

THE UNIVERSITY OF CHICAGO

DEVELOPMENTS OF MICROWAVE KINETIC INDUCTANCE DETECTORS

A DISSERTATION SUBMITTED TO
THE FACULTY OF THE DIVISION OF THE PHYSICAL SCIENCES
IN CANDIDACY FOR THE DEGREE OF
DOCTOR OF PHILOSOPHY

DEPARTMENT OF ASTRONOMY AND ASTROPHYSICS

BY
ELYSSA BROOKS

CHICAGO, ILLINOIS

AUGUST 2024

Copyright © 2024 by Elyssa Brooks

All Rights Reserved

This thesis is dedicated to my late advisor Erik Shirokoff, my late kitten Volo, my wife Celeste, and our two cats Orin and Aylin. Thank you for everything.

It's never too late to change your mind.

TABLE OF CONTENTS

LIST OF FIGURES	vii
LIST OF TABLES	xii
ACKNOWLEDGMENTS	xiii
ABSTRACT	xiv
1 INTRODUCTION	1
1.1 Far-Infrared Astronomy	2
1.2 Line Intensity Mapping	4
1.3 MKID Experiments	4
2 THE PHYSICS BEHIND KINETIC INDUCTANCE DETECTORS	7
2.1 The Two-Fluid Model and BCS Theory	8
2.2 Mattis-Barden Theory	9
2.2.1 Superconducting Thin Film Surface Impedance	10
2.2.2 Local limit	11
2.2.3 Extreme anomalous limit	11
2.2.4 Thin film limit	12
2.3 Quasiparticle Dynamics	13
2.4 Microwave Properties	15
2.4.1 Scattering Parameters	16
2.4.2 I and Q	16
2.4.3 RLC Circuits	17
2.4.4 Asymmetry and Bifurcation	19
2.5 Responsivity	20
2.6 Noise Properties	22
2.6.1 Generation-Recombination Noise	22
2.6.2 Photon Noise	22
2.6.3 Two-Level System Noise	23
2.7 Lumped-Element KIDs	24
3 DESIGN, FABRICATION, AND TESTING OF KIDS FOR THZ SPECTROSCOPY	26
3.1 The RAxDE Idea	27
3.2 Focal Plane Design	27
3.3 Absorber and KID Design	29
3.4 Fabrication	31
3.5 Test Setup	36
3.6 Results	38

4	FABRICATION AND TESTING OF KIDS FOR LINE INTENSITY MAPPING	41
4.1	The South Pole Telescope Summer Line Intensity Mapping Project	42
4.2	Detector Design	42
4.3	Fabrication	46
4.4	Testing Setup	47
4.5	Detector Performance and Improvements	50
4.5.1	Fabrication and Design Improvements	50
4.5.2	Anomalies in the Feedline	53
4.5.3	Quality Factors	56
4.5.4	Frequency Placement	58
4.5.5	Polarization Measurements	59
4.5.6	Detector Noise	65
4.5.7	Spectral Response	65
5	FORECASTING OF SPT-SLIM CONSTRAINTS ON THE LUMINOSITY FUNCTION	72
5.1	Line Intensity Mapping Measurements	73
5.2	Formalism	73
5.2.1	The Cluster-Power Component	74
5.2.2	The Shot-Power Component	75
5.2.3	Direct Detections	75
5.3	Likelihood Method	76
5.3.1	Power Spectrum	76
5.3.2	Luminosity Function	77
5.4	Data Generation	77
5.5	Preliminary Results	79
6	CONCLUSION	82

LIST OF FIGURES

<p>1.1 <i>Left:</i> A diagram showing the galactic fountain model. The stellar disk ejects matter via stellar winds and supernovae to the outskirts around a galaxy. In the outskirts, the gas cools and falls back into the galaxy. <i>Right:</i> A multiband image of M82 showing matter ejected from the disk. Optical light is in yellow, green, and orange, infrared is in red, and x-ray is in blue. Credit: X-ray: NASA/CXC/JHU/D.Strickland; Optical: NASA/ESA/STScI/AURA/The Hubble Heritage Team; IR: NASA/JPL-Caltech/Univ. of AZ/C. Engelbracht</p> <p>1.2 A three-dimensional map of the local universe in the range $z < 0.15$ created by the Sloan Digital Sky Survey. Redshifts are calculated using photometric redshifts. Credit: Sloan Digital Sky Survey</p> <p>1.3 A one square degree simulated galaxy field at $z \sim 5$. From left to right are all galaxies, galaxies visible to conventional telescopes (an arbitrary cutoff of $M_{gal} \geq 10^{9.5} M_{\odot}$), the CO emission, and the CII emission. The CO and CII emissions have instrument characteristic angular resolutions applied. Credit: [7]</p> <p>2.1 A diagram of a parallel RLC circuit with a coupling capacitor. The signal enters from port 1 on the left and exits through port 2 on the right. A coupling capacitor separates the RLC circuit from the feedline in order to control the coupling quality factor. [60]</p> <p>2.2 A plot showing the three solutions of a bifurcated resonator. The following parameters were used to generate the solutions: $Q = 2 * 10^5$, $Q_c = 1.5 * 10^6$, $a = 2$, and resonance frequencies of 1.00003, 1.00005, 1.00007 GHz for solutions 0, 1, and 2 respectively.</p> <p>3.1 <i>Top:</i> A diagram of a rectangular waveguide with a microcavity resonator. The terahertz signal enters through port 1 and leaves through port 2. Specific frequencies are selected by the cavity resonator and exit through port 3 to the detector. <i>Middle:</i> An HFSS simulation of the electric field distribution for a on-resonance signal. <i>Bottom:</i> Scanning electron microscope images of a fabricated spectrometer. The images represent from left to right the top view, the cross-section, and the corner detail. The gold coating is 596nm on the top surface and 239nm on the side walls. [50]</p> <p>3.2 Waveguide geometry and box design. (a) A schematic drawing of the two wafer design. The filterbank wafer has gold coated trenches and the detector wafer has gold except where the MKIDs and readout lines are. When pressed together, they form a closed waveguide. (b) A top-down microscope image of the main waveguide and one filter before gold coating. (c) An edge on view of the two-chip stack with a zoom in of the $80 \times 160 \mu\text{m}$ waveguide. Also in view are the spring plungers that press the two chips together. (d) The prototype device box. Shown are the alignment pins, launcher boards for wire bonding, SMA connectors to send and receive the microwave signal, and the spring plunger layout.</p>	<p>3</p> <p>5</p> <p>6</p> <p>18</p> <p>21</p> <p>28</p> <p>30</p>
---	--

3.3	Different views of the simulations of the detector absorber in relation to the waveguide. <i>Top Left</i> : Isometric view. S31, the signal after passing through the cavity resonator, enters through the far side of the drawing. <i>Top Right</i> : Front view. The waveguide forms the bottom part of the simulation and the absorber and silicon wafer sit on top of the waveguide. <i>Bottom Left</i> : Top view. The absorber is an annulus that is on a thin piece of silicon on the detector wafer. <i>Bottom Right</i> : Right view. The etched area behind the silicon membrane acts as a backstop to reflect the signal that isn't absorbed back into the absorber. . . .	32
3.4	Simulations and overall MKID device layout. (a) A plot of an HFSS simulation of the absorber on top of the waveguide. The absorber absorbs greater than 60% of the power between 1.4 and 2.0 THz that passes through the waveguide filter. (b) Layout of a full MKID. The Au waveguide top is in blue at the bottom. The Al inductor is in black and sits just on top of the waveguide. The Nb IDC, co-planar waveguide, and ground are in red. (c) A close up microscope image of the Al inductor and absorber. The absorber is $26\mu\text{m}$ in inner diameter and $2\mu\text{m}$ in width. The large pads are to ensure adequate contact with the Nb IDCs. (d) An overview microscope image of the entire 14mm mounted device chip. The waveguide is in the center of the chip and the 18 MKIDs branch off of it. . . .	33
3.5	A diagram of the fabrication steps for both the detector wafer and the waveguide wafer. The detector wafer steps shown are the initial gold layer, the aluminum deposition, the aluminum etch, the niobium deposition, the niobium etch, and the alignment pin etch. For the waveguide wafer, the steps are the waveguide etch, a photoresist deposition, the gold deposition, the gold lift-off, and the protective and alignment etches.	37
3.6	A diagram of the microwave components used in a single-tone homodyne measurement.	38
3.7	Test results from one resonance on a prototype device. <i>Upper Left</i> : S_{21} VNA sweeps of one resonance with temperature varying from 30mK to 300mK. Temperatures 60mK to 150mK are omitted since the resonance only starts to move at approximately 180mK. <i>Upper Right</i> : S_{21} VNA sweeps of one resonance with the attenuation varied over 7dB. As the attenuation decreases, the resonance bifurcates and becomes non-linear. To obtain ideal noise performance, we need to drive the resonances with as much power as we can as long as they remain in the linear regime. <i>Bottom</i> : The fractional frequency noise of a single tone on and off the resonance frequency. We take two separate timestreams at different sample rates to simplify data processing and obtain more accuracy over a wide range of frequencies.	40
4.1	a: A diagram of the SPT-SLIM cryostat. b: A model of the detector box and horn array. c: An early SPT-SLIM focal plane design with three separate silicon submodules. d: A cross-section diagram of the detector including an absorber and the backshort. [5]	43

4.2	a: A layout diagram showing key components of the detector architecture including the OMT probes with a 180° hybrid to send the combined signal to the filterbank. The inset shows the mm-wave feedline, the capacitively coupled $\lambda/2$ filter, and the KID inductor. b: <i>Left:</i> The layout of microwave microstrip resonators in order to measure dielectric properties. <i>Middle:</i> Measurements of SiN dielectric and <i>Right:</i> amorphous silicon.	44
4.3	Two python model simulations of an SPT-SLIM filter bank between 120–180 GHz showing both the single and total power transmission. Each channel is oversampled by a factor of 1.6. The colored lines show the approximate actual device characteristics when fabrication errors and dielectric loss is included. The gray lines are the theoretical transmissions with no errors or losses. [54]	44
4.4	A diagram of the full SPT-SLIM submodule design on a six inch silicon wafer with various test devices. Spring-loaded pogo pins located between some of the resonator banks secure the wafer inside the detector box to prevent vibrations. Two dowel hole pins are made to ensure the wafer stays aligned with the horn inside the detector box. The test devices allow for quick checks of the viability of a submodule as well as other diagnostic structures. [5]	45
4.5	A diagram of the fabrication steps for a SPT-SLIM submodule device. The steps shown are the initial six inch wafer with SiO and low stress SiN, the aluminum deposition, the aluminum etch, the niobium deposition, the niobium etch, the SiN deposition, a second Nb deposition, a second Nb etch, a SiN etch, a Si etch, and a SiO etch. The upper Nb layer is the ground plane while the lower Nb layer is the device layer. The OMT sits only on the low stress SiN membrane so that light can be reflected via a backshort.	48
4.6	Measurements of S21 transmission over a few hundred MHz for the spt_slim_mux_2 device. The three measurements shown are with the detector box lid on, the box lid off, and the box lid coated in a black, light-absorbing material. Removing the lid did little to change the overall amplitude of the standing wave, but blackening the lid did reduce the standing wave. This implied the standing wave could be partially due to the capacitors coupling to the lid of the detector box.	51
4.7	A simulated S21 transmission comparing the initial ground-plane bridge width and an optimal bridge width. <i>Credit: Gethin Robson</i>	52
4.8	A diagram of the parallel plate capacitor test structure. In this test structure, the orientation of the capacitors is flipped relative to the detector design in order to expose the separated niobium pads. In test structure A, the top layer niobium does not extend over the dielectric whereas the opposite is true for test structure B.	54

4.9	<i>Top</i> : A measurement of S21 vs frequency for the initial optical testing of the submodule. The baseline should be approximately horizontal with no variations in this frequency regime. The spikes can easily be seen including both some regularity and irregularity in their frequency position. <i>Middle</i> : A timestream of the in-phase component at a specific frequency in the region where the spikes appear. A Fourier transform of this component reveals that there is not a specific frequency that the spike appear at. <i>Bottom</i> : The in-phase and quadrature components during a sweep in frequency. The spikes are seen here as curved deviations away from expected circle from the cable delay.	55
4.10	An example PPC resonance from spt_slim_submodule_2. This resonance had quality factors of $Q \sim 1.6 * 10^4$, $Q_i \sim 2.2 * 10^4$, and $Q_c \sim 1.5 * 10^4$. The resonances were generally more shallow than the IDCs with averages of $Q \sim 2 * 10^4$, $Q_i \sim 3 * 10^4$, and $Q_c \sim 1 * 10^5$. The higher than design Q_c is likely due to not fully characterizing the SiN at the University of Chicago fabrication facility.	56
4.11	The distributions of Q (<i>Top</i>), Q_i (<i>Middle</i>), and Q_c (<i>Bottom</i>) on the multiplexing test device slim_mux_2. The Q_i have a localized distribution centered around $1.5 * 10^5$ while the Q_c are much more spread out between 10^4 and 10^6 . Since Q depends on Q_i and Q_c , the distribution is a more spread out version of the Q_i distribution with an average of $7.5 * 10^4$. There were 142 resonances that were measured on this device.	57
4.12	A full device VNA sweep from 2.2GHz to 2.8GHz for ripple test device slim_ripple_v1. The large baseline variation of 3-5dB can be seen throughout the sweep. There were 155 out of 160 resonances found on this device.	58
4.13	<i>Top</i> : An example ideal resonance from spt_slim_submodule_2 trio IDC bank. This resonance had quality factors of $Q \sim 1.6 * 10^4$, $Q_i \sim 2.3 * 10^4$, and $Q_c \sim 5.5 * 10^4$. <i>Middle</i> : The frequencies of each KID on spt_slim_submodule_2 trio IDC bank. Each bank of resonators begins and ends with a small bump in resonance frequency. The resonance frequencies tend to bunch up at the end of a bank. <i>Bottom</i> : A histogram of the resonance frequency spacing scaled by the resonance quality factor. A clash for SPT-SLIM is defined as having a spacing $\frac{Q\delta f}{f_0} < 3$	60
4.14	<i>Top</i> : The frequencies of each KID on spt_slim_submodule_2 duo IDC bank. Each bank of resonators begins and ends with a small bump in resonance frequency. The resonance frequencies tend to bunch up at the end of a bank. <i>Bottom</i> : A histogram of the resonance frequency spacing scaled by the resonance quality factor. A clash for SPT-SLIM is defined as having a spacing $\frac{Q\delta f}{f_0} < 3$	61
4.15	Plots showing the separation between the chopped and unchopped signals in terms of df/f for FT47. The first 13 KIDs are narrowband detectors and the remaining KIDs are broadband detectors. Each KID was fitted for polarization angle and cross-polarization. The first set of plots uses specific polarization angles whereas the second set uses a rotating polarizing grid.	64

4.16	Plots showing the separation between the chopped and unchopped signals in terms of df/f for FT84. The first 13 KIDs are narrowband detectors and the remaining KIDs are broadband detectors. Each KID was fitted for polarization angle and cross-polarization. 2 KIDs were also manually fitted because least-squares fitting produced too high of cross-polarization.	66
4.17	Plots showing the separation between the chopped and unchopped signals in terms of df/f for FT89. The first 13 KIDs are narrowband detectors and the remaining KIDs are broadband detectors. Each KID was fitted for polarization angle and cross-polarization.	67
4.18	Noise power spectrums taken on and off resonance from KID 66 and KID 87 from spt_slim_submodule_2 IDC duo bank taken at 30mK. KID 66 had a quality factor approximately twice as large as KID 87 which explains the difference in absolute noise levels. Both resonances feature $1/f$ noise to a frequency of 50Hz.	68
4.19	The spectral response for 2 broadband KIDs (<i>Top</i>) and 5 narrowband KIDs (<i>Bottom</i>) on device ft84. The broadband responses show no broad peaks but instead show a number of smaller peaks, indicating that the detector is not functioning correctly. The narrowband responses show two peaks from FB011 and FB012 with FB011 significantly stronger. This indicates some issue either in fabrication or with the testing setup that is able to produce the appropriate response occasionally.	70
4.20	The spectral response for 64 spectral channels and 35 broadband channels on submodule_24 fabricated and measured by other members of the SPT-SLIM collaboration.	71
5.1	An example CO(3-2) power spectrum at a redshift of 1.3. The parameters used to generate the power spectrum are the same as is mentioned in section 5.4. Also shown are the two components of the power spectrum, the clustering and shot power. The blue shaded region are the target wavenumbers that SPT-SLIM will constrain.	74
5.2	The parameter contour and marginalized χ^2 for the power spectrum only analysis. The curves represent Gaussians because the equation is linear with respect to the two parameters. 1 and 4σ contours are plotted in black on the lower left image.	80
5.3	Marginalized log likelihoods of the three parameters of the luminosity function. The top two images of the right column show the data points, the true power spectrum and luminosity function curves, and the curves corresponding to the maximal likelihood.	81

LIST OF TABLES

4.1	A summary of the SPT-SLIM devices fabricated at the University of Chicago.	49
5.1	Cosmological parameters used to generate the matter power spectrum.	77
5.2	Telescope and observational parameters used in data and error generation.	78

ACKNOWLEDGMENTS

I would like to acknowledge many different people and things that have all helped me through my journey. First, I would like to thank my wife Celeste Keith for always being there throughout some of the hardest moments of my life. I love you so much and can't wait to go on so many different trips and adventures with you in the next phase of our lives. I would also like to thank the research advisors that have provided me support throughout my life, Ellen Zweibel, Frank Lind, Bradford Benson, Adam Anderson, Damiano Caprioli, Erik Shirokoff, Kirit Karkare, Peter Barry, and Clarence Chang. Many thanks to my committee Clarence Chang, Kirit Karkare, Bradford Benson, Jeffrey McMahon, and Dan Hooper for providing guidance and feedback throughout my graduate studies. My two cats Orin and Aylin have been a much needed source of comfort in recent months. The mental health support provided by my two therapists and my psychiatrist has been vital to my life for the last two years. Thank you to the many friends who have provided so much joy to my life Julia Fish, Ben Reeve, Kevin Gayley, Qing Yang Tang, Karia Dibert, Andrew Neil, Diane Gayley, Megan Barnett, Cuncheng Chen, Emily Simon, Adina Feinstein, and many others. Thank you to Karen Wesener and Lee Keith for the support and guidance you have offered me.

ABSTRACT

In this thesis, I will cover the fabrication, testing, and analysis of microwave kinetic inductance detectors (MKIDs) for both THz and mm-wave spectroscopy. MKIDs are a detector technology that enables large numbers of highly-sensistive mm/submm detectors to be read out using a small number of readout lines, which enables large-format spectroscopy. They can be produced such that a small piece of silicon contains both the spectrometer and detector. The RAxDEx project produced prototype THz spectrometers with a novel, in-chip rectangular waveguide. THz spectroscopy with MKIDs will enable the coupling of large fields-of-view to multi-kilopixel detectors. These devices would drastically improve our ability to map the cooling gas around galactic fountains by using hyperfine cooling lines among other uses for far-infrared spectroscopy. I present prototype dark MKIDs for RaxDEx that match design and noise specifications. In addition, SPT-SLIM is a project to create a mm-wave spectrometer for line intensity mapping with the South Pole Telescope. Line intensity mapping is expected to dramatically increase our knowledge of large scale cosmological structure, particularly in regards to galaxies that are too dim to be detected directly. I will present both dark and optical measurements from SPT-SLIM devices from initial prototypes to the final design submodules. Finally, I will cover an initial analysis of how SPT-SLIM will use unresolved, high-redshift galaxies to constrain the CO power spectrum and the luminosity function.

CHAPTER 1

INTRODUCTION

1.1 Far-Infrared Astronomy

Far-infrared (FIR) wavelength light (30-300 μ m) is a prime target for astrophysical observations because it provides unique opportunities for understanding astrophysical processes and emission [24]. FIR provides opportunities to study processes that are not visible at other wavelengths, such as young stellar objects and assembly of supermassive black holes. Many atomic emission lines such as [OI], [NII], [CI], and [CII] as well as various molecular emission lines like CO, H₂O, and HCN are emitted in the FIR. Specifically, the galactic fountain model posits that material in disk galaxies is ejected due to star formation and supernovae (see figure 1.1). After the gas is ejected, it eventually cools and falls back into the galaxy. This cooling gas has been difficult to observe for a number of reasons [63]. However, the [NII] and [CII] cooling lines are likely able to be observable by a FIR spectroscopic experiment. [NII] and [CII] are remarkably robust tracers of cooling across a wide range of temperatures[65]. Dust in the temperature range of 15K to 100K emits thermal radiation in the FIR. Furthermore, FIR can identify polarized dusty foregrounds for cosmic microwave background (CMB) observations that cannot be removed in any other way.

Unfortunately, FIR radiation is heavily absorbed by the Earth's atmosphere except in a few narrow windows. Thus there is a great need to develop space-based instruments that can target the wavelengths we cannot see on the ground. There have been a number of space-based astrophysical spectrometer instruments that have probed this region of light [24]. One example of a space-based FIR spectrometer is the SWS/LWS Fabry-Perot etalons on ISO[15]. The most recent examples are the PACS grating spectrometer on *Herschel*[51] and the SPIRE-FTS Fourier transform spectrometer on *Herschel*[30]. However, Herschel was limited by emission from the telescope because it was at 85K. Another limiting factor is the dynamic range of telescopes. FIR sources can vary greatly in brightness, so detectors either have to have a high saturation limit or have separate arrays for differing intensity sources. Furthermore, the next generation of spectrometers will need to be able to couple large fields-of-view to multi-kilopixel focal planes. Each spectrometer architecture has downsides in this

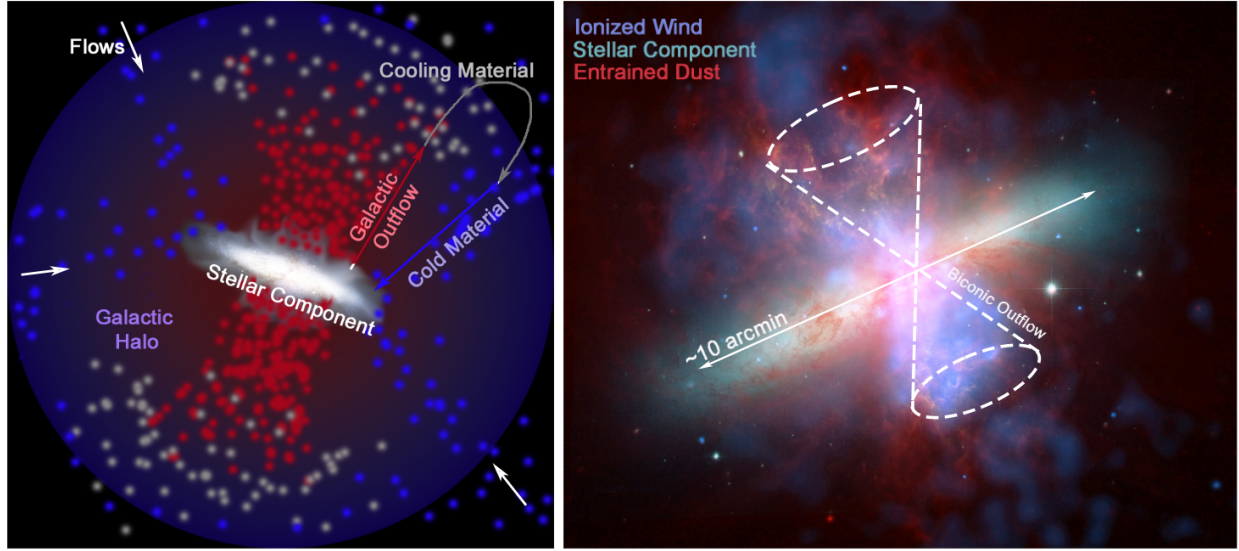


Figure 1.1: *Left:* A diagram showing the galactic fountain model. The stellar disk ejects matter via stellar winds and supernovae to the outskirts around a galaxy. In the outskirts, the gas cools and falls back into the galaxy. *Right:* A multiband image of M82 showing matter ejected from the disk. Optical light is in yellow, green, and orange, infrared is in red, and x-ray is in blue. Credit: X-ray: NASA/CXC/JHU/D.Strickland; Optical: NASA/ESA/STScI/AURA/The Hubble Heritage Team; IR: NASA/JPL-Caltech/Univ. of AZ/C. Engelbracht

regard. Grating spectrometers are difficult to couple to wide fields-of-view, Fourier transform spectrometers have increased integration time due to the need for spectral modulation in the time domain, and Fabry-Perot instruments are mechanically demanding and have narrow free spectral range.

1.2 Line Intensity Mapping

Large-scale structure (LSS) is one of the key components to constrain cosmological models and star formation history. LSS is typically measured with large-scale optical galaxy surveys that detect individual galaxies (see figure 1.2). However, the majority of galaxies will not be visible at higher redshifts because they are too faint. To combat this difficulty, line intensity mapping (LIM) is a relatively recent technique that seeks to use large-scale maps of gas line emission in order to trace matter in the universe (see figure 1.3). Using spectroscopy with LIM allows for the creation of 3 dimensional maps and a low angular resolution allows for large volumes of the universe to be mapped. The best suited line emissions for far-IR LSS LIM are CO rotational lines and [CII] fine-structure lines. Current LIM instruments are limited by sensitivity and are not able to place strong constraints on cosmological parameters or high-redshift astronomy.

1.3 MKID Experiments

MKIDs were first proposed as an astrophysical detector by Peter Day and Benjamin Mazin in the early 2000s [17][45]. The mechanism of detection and properties of MKIDs will be described in chapter 2. Here we discuss the various experiments that MKIDs have been utilized for.

The Multiwavelength Sub-millimeter Inductance Camera (MUSIC) was one of the first MKID experiments. MUSIC is a photometric imaging camera measuring at the four wavelengths of 0.87, 1.04, 1.33, and 1.98 mm [28]. MUSIC has a 14 degree field-of-view with 2304

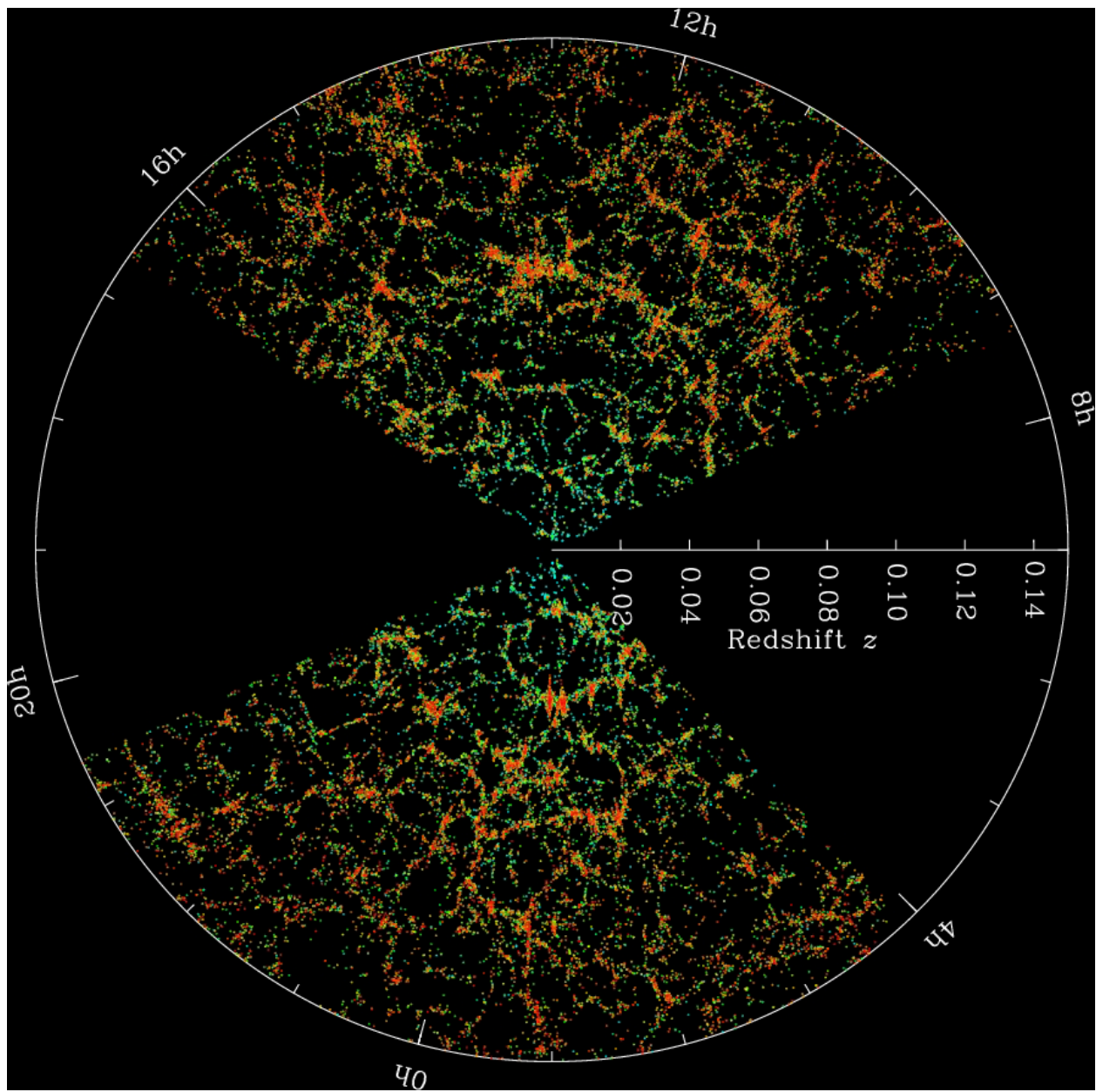


Figure 1.2: A three-dimensional map of the local universe in the range $z < 0.15$ created by the Sloan Digital Sky Survey. Redshifts are calculated using photometric redshifts. Credit: Sloan Digital Sky Survey

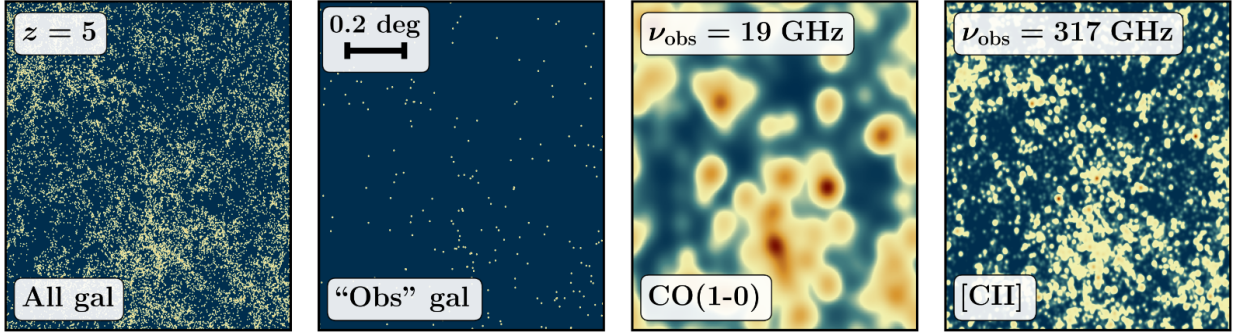


Figure 1.3: A one square degree simulated galaxy field at $z \sim 5$. From left to right are all galaxies, galaxies visible to conventional telescopes (an arbitrary cutoff of $M_{gal} \geq 10^{9.5} M_{\odot}$, the CO emission, and the CII emission. The CO and CII emissions have instrument characteristic angular resolutions applied. Credit: [7]

detectors in 576 spatial pixels.

Another example of an imaging camera is the Mexico UK Sub-mm Camera for AsTronomy (MUSCAT) [8][62]. MUSCAT targeted the 1.1mm band 1458 horn-coupled lumped-element KIDs. The camera was commissioned in 2022 on the 50m Large Millimeter Telescope.

MKIDs have also been used to create on-chip spectrometers by using a feedline to send photons to filters that only couple certain frequencies of light onto each KID. One example of this is the DESHIMA project that has a single pixel covering the wavelengths of 322 to 377GHz [22][23]. The second generation of DESHIMA is currently in development and upgrades both the frequency range to 220 to 440GHz and increases the number of MKIDs from 49 to 347 [61]. Another example is the SuperSpec project which aims for 200 to 450GHz frequency band and is also a single pixel device [57][46].

CHAPTER 2

THE PHYSICS BEHIND KINETIC INDUCTANCE

DETECTORS

This chapter will cover the physical principles that allow the creation of a KID and their properties. Kinetic inductance detectors utilize specific properties of superconductivity in order to measure small changes in energy caused by the absorption of photons. Roughly speaking, pairs of electrons that have no resistance form the charge carriers in a superconductor. Since electrons have mass, an alternating current will create an inductance due to the inertia of the electrons. An incoming photon that deposits energy into the superconductor and break apart these electron pairs. Which in turn causes a measurable change in the inductance of the metal. This change in inductance forms the basis for the operation of KIDs.

2.1 The Two-Fluid Model and BCS Theory

One of the first phenomenological models created to describe the effects of superconductivity was the two-fluid model created by Gorter and Casimir [29]. This theory postulates that the electrons in a superconducting metal are made up of two different charge carriers. The first being the normal electrons that follow the standard laws of physics and the second is a separate fluid that is responsible for the properties of superconductivity. Below some critical temperature T_c , the electrons would transfer from the first fluid to the second fluid. The second fluid would then be able to transfer current with no resistance.

Cooper, in 1956, showed that a pair of electrons in a metal can become bound if there is an arbitrarily small attraction between them [16]. This creates an available energy state for the electrons that is less than the Fermi energy. This discovery formed a major component of the BCS theory of superconductivity [2]. It was discovered that an electron-phonon interaction created by the movement of electrons through a lattice of positive charges (atomic nuclei) could create a small attractive force. As an electron moves through a lattice, it slightly deforms the lattice. Another electron will then be attracted to the slightly higher positive charge created by the deformation. The two electrons become correlated and form a Cooper pair. The binding energy of this pair near T_c is $\Delta = 3.2k_B T_c(1 - T/T_c)^{1/2}$. As more pairs

are created, they overlap and form a collective condensate that resists scattering off the lattice because scattering would require the pairs to break. Normal electrons are scattered impurities and vibrations creating resistance, but since Cooper pairs behave collectively, they have virtually no resistance.

2.2 Mattis-Barden Theory

A detailed electrodynamic theory of superconductivity was developed by Mattis and Bardeen in 1958 [42]. The theory is complex and a more detailed explanation on how the theory is applied to KIDs can be found in [44] [25] [66]. However, the conductivity $\sigma = \sigma_1 - i\sigma_2$ can be calculated in various limits.

The theory provides equations for σ_1 and σ_2 given by

$$\frac{\sigma_1}{\sigma_n} = \frac{2}{\hbar\omega} \int_{\Delta}^{\infty} dE \frac{(E(E + \hbar\omega) + \Delta^2)(f(E) - f(E + \hbar\omega))}{\sqrt{E^2 - \Delta^2} \sqrt{(E + \hbar\omega)^2 - \Delta^2}} \quad (2.1)$$

$$\frac{\sigma_2}{\sigma_n} = \frac{1}{\hbar\omega} \int_{\Delta}^{\Delta + \hbar\omega} dE \frac{(E(E - \hbar\omega) + \Delta^2)(1 - 2f(E))}{\sqrt{E^2 - \Delta^2} \sqrt{\Delta^2 - (E - \hbar\omega)^2}} \quad (2.2)$$

where σ_n is the non-superconducting (normal state) conductivity and $f(E)$ is the distribution function for unpaired quasiparticles. In thermal equilibrium, $f(E)$ is the Fermi-Dirac distribution $f(E) = 1/(e^{E/k_B T} + 1)$.

Next, we consider the limit at low temperature $k_B T, \hbar\omega \ll \Delta(T)$. In this limit, equations 2.1 and 2.2 become analytical and have the form [25] [3]

$$\frac{\sigma_1}{\sigma_n} \approx \frac{4\Delta}{\hbar\omega} e^{\frac{-\Delta}{k_B T}} \sinh(\xi) K_0(\xi) \quad (2.3)$$

$$\frac{\sigma_2}{\sigma_n} \approx \frac{\pi\Delta}{\hbar\omega} (1 - 2e^{\frac{-\Delta}{k_B T}} e^{-\xi} I_0(\xi)) \quad (2.4)$$

where $\xi = \hbar\omega/2k_B T$, and I_0 and K_0 are the Bessel functions of the first and second kind

respectively.

We can also define the density of quasiparticles as

$$n_{qp} = 4N_0 \int_0^\infty dE \frac{f(E)E}{\sqrt{E^2 - \Delta^2}} \approx 2N_0 e^{\frac{-\Delta}{k_B T}} \sqrt{2\pi k_B T \Delta} \quad (2.5)$$

where N_0 is the density of single-spin electron states at the Fermi energy. This is simply the quasiparticle distribution function multiplied with the superconducting density of states.

2.2.1 Superconducting Thin Film Surface Impedance

We generally cannot measure the complex conductivities defined in 2.3 and 2.4. However, we can measure the complex surface impedance $Z_s = R_s + iX_s$. R_s is the surface resistance and X_s is the surface reactance. So we need to create a link between the surface impedance and the conductivity.

Linking these is not straightforward, unless certain limits are considered. These limits have to do with physical length and film thickness. The three limits are the local limit, the anomalous limit, and the thin film limit.

First we need to define two characteristic length scales, the coherence length ξ_0 and the penetration depth λ (see [66] [19] for more detailed explanations). ξ_0 can be understood as the distance of the bond of the two electrons in a cooper pair. This is defined as $\xi_0 = \hbar v_f / \pi \Delta_0$, where v_f is the Fermi velocity of electrons. λ is the depth that a magnetic field is able to penetrate a superconductor. The calculation of λ varies depending on the limits being applied.

Non-idealities in a superconductor, however, will degrade the coherence length. This leads to a mean free path of Cooper pairs defined as $l = \tau v_f$. τ , in this instance, is the time it takes for Cooper pairs to collide with the impurities in the superconductor. This leads to an effective coherence length ξ defined as

$$\frac{1}{\xi} = \frac{1}{\xi_0} + \frac{1}{l} \quad (2.6)$$

We can then define two more limits, the clean and dirty limits, where $l \gg \xi_0$ and $l \ll \xi_0$ respectively.

2.2.2 Local limit

The local limit is defined as the limit where $\lambda \gg \xi$. Since the coherence length is small compared to the magnetic field effects, the response of the charge carriers is local. This condition arises only when the film thickness is much greater than the penetration depth.

In this limit, the penetration depth is defined as $\lambda_{\text{local}} = \sqrt{\hbar/\pi\Delta\mu_0\sigma_n}$. The relations between the surface impedance and the conductivity is calculated as

$$Z_s = \sqrt{i\mu_0\omega/\sigma} \quad (2.7)$$

Both Z_s and σ vary with temperature, so we can see the how the surface impedance changes in response to a small change in temperature.

$$\delta Z_s = -\frac{1}{2} \sqrt{\frac{i\mu_0\omega}{\sigma^3}} \delta\sigma \quad (2.8)$$

$$\frac{\delta Z_s}{Z_s} = -\frac{1}{2} \frac{\delta\sigma}{\sigma} \quad (2.9)$$

2.2.3 Extreme anomalous limit

The extreme anomalous limit is the opposite of the local limit. In this instance, the coherence length is large compared to the penetration depth, $\lambda \gg \xi$. This limit also only occurs when the film thickness is much greater than the penetration depth. With the response no longer local, the penetration depth can be defined as $\lambda_{\text{anom}} = \lambda_{\text{local}}^{2/3} (\sqrt{3}l/2\pi)^{1/3}$. Similar to before,

the surface impedance is

$$Z_s = i\mu_0\omega\lambda_{\text{anom}}(1 + \frac{i\delta\sigma}{\sigma_{2,0}})^{-1/3} \quad (2.10)$$

where $\sigma_{2,0} = \sigma_2(T = 0)$ is the complex part of the conductivity at a temperature of 0.

Taking a small change in temperature yields

$$\delta Z_s = \frac{-1}{3}i\mu_0\omega\lambda_{\text{anom}}(1 + \frac{i\delta\sigma}{\sigma_{2,0}})^{-4/3}\delta(1 + \frac{i\delta\sigma}{\sigma_{2,0}}) \quad (2.11)$$

$$\frac{\delta Z_s}{Z_s} = \frac{-1}{3}\delta\ln(1 + \frac{i\delta\sigma}{\sigma_{2,0}}) \quad (2.12)$$

$$\frac{\delta Z_s}{Z_s} = \frac{-1}{3}\delta\ln(\frac{i\sigma}{\sigma_{2,0}}) \quad (2.13)$$

$$\frac{\delta Z_s}{Z_s} = \frac{-1}{3}\frac{\delta\sigma}{\sigma} \quad (2.14)$$

2.2.4 Thin film limit

Finally, when the superconducting film is no longer much thicker than the penetration depth, we have the thin film limit. In this instance, the surface density of the superconducting film is nearly constant. This leads to a penetration depth of $\lambda_{\text{thin}} = \lambda_{\text{local}}^2/t$, where t is the film thickness. This limit is the regime that the work in this thesis belongs to. Again, we have the surface impedance

$$Z_s = i\mu_0\omega\lambda_{\text{thin}}(1 + \frac{i\delta\sigma}{\sigma_{2,0}})^{-1} \quad (2.15)$$

and the response to small changes in temperature

$$\delta Z_s = -i\mu_0\omega\lambda_{\text{anom}}(1 + \frac{i\delta\sigma}{\sigma_{2,0}})^{-2}\delta(1 + \frac{i\delta\sigma}{\sigma_{2,0}}) \quad (2.16)$$

$$\frac{\delta Z_s}{Z_s} = -\delta\ln(1 + \frac{i\delta\sigma}{\sigma_{2,0}}) \quad (2.17)$$

$$\frac{\delta Z_s}{Z_s} = -\delta\ln(\frac{i\sigma}{\sigma_{2,0}}) \quad (2.18)$$

$$\frac{\delta Z_s}{Z_s} = -\frac{\delta\sigma}{\sigma} \quad (2.19)$$

Now we can see that

$$\frac{\delta Z_s}{Z_s} = -\gamma\frac{\delta\sigma}{\sigma} \quad (2.20)$$

where $\gamma = 1, 1/2$, and $1/3$ for the thin film, local, and extreme anomalous limits respectively. This equation allows us to relate how changes in temperature of the superconducting film affect the measurable impedance. This is the foundation of KID operation, where the small temperature change is generally provided by an absorbed photon.

2.3 Quasiparticle Dynamics

The number density of quasiparticles stated in the previous section is an average. The true number of quasiparticles fluctuates due to Cooper pairs randomly hitting the metal lattice and breaking apart. The quasiparticles do quickly condense back into a Cooper pair after some quasiparticle lifetime τ_{qp} . The fluctuations from the generation and recombination of quasiparticles sets the intrinsic limit for noise in KIDs.

Diving into this dynamic further, we can write an equation for the change in the number of quasiparticles in terms of a generation rate Γ_g and a recombination rate Γ_r ,

$$\frac{dN_{qp}}{dt} = 2(\Gamma_g - \Gamma_r) \quad (2.21)$$

The recombination rate is by definition the product of the number of quasiparticles and the inverse of the quasiparticle lifetime $\Gamma_r = \frac{1}{2}N_{qp}/\tau_{qp}$. The factor of $\frac{1}{2}$ comes from the fact that two quasiparticles are needed to recombine. The value of τ_{qp} was calculated by Kaplan in 1976 [35]

$$\tau_{qp} = \frac{\tau_0}{\sqrt{\pi}} \left(\frac{k_B T_c}{2\Delta} \right)^{5/2} \sqrt{\frac{T_c}{T}} \exp\left(\frac{\Delta}{k_B T}\right) \quad (2.22)$$

Substituting in our value of n_{qp} from equation 2.5 gives

$$\tau_{qp} = \frac{\tau_0}{n_{qp}} \frac{N_0 (k_B T_c)^3}{2\Delta^2} = R^{-1} n_{qp}^{-1} \quad (2.23)$$

where R is the rate proportionality constant. Substituting this into the equation for Γ_r from above gives

$$\Gamma_r = RV n_{qp}^2 / 2 \quad (2.24)$$

In thermal equilibrium, the number of quasiparticles does not change with time. Thus, equation 2.21 becomes

$$\Gamma_r = \Gamma_g = \Gamma_{th} + \Gamma_{ex} \quad (2.25)$$

Here we have separated the generation rate into two components, thermal and excitations. The excitations can be from optical signal or from readout power. In thermal equilibrium, the thermal generation and recombination rates are required to be equal, $\Gamma_{th} = \Gamma_r(n_{th})$. The value of n_{th} is calculated using equation 2.5. Using equation 2.24 and the assumption that the optical signal is the dominant source of excitations gives

$$n_{qp}^2 = n_{th}^2 + \frac{2\Gamma_{opt}}{RV} = n_{th}^2 + n_{opt}^2 \quad (2.26)$$

Now we define the optical power as $P_{opt} = \Delta\Gamma_{opt}/\eta_{pb}$. η_{pb} is the pair breaking efficiency and it is less than one because some of the photon energy isn't captured by Cooper pairs [10] [17] [20]. Using the equation for the optical power, equation 2.25, and equation 2.23 for R , we can derive an equation for n_{opt} in terms of P_{opt}

$$n_{opt}^2 = \frac{\eta_{pb} N_0 \tau_0 (k_B T_c)^3}{\Delta^3 V} P_{opt} \quad (2.27)$$

Taking the derivative of equation 2.26 with respect to P_{opt} gives an equation for how the quasiparticle density changes with respect to an optical signal.

$$\frac{\delta n_{qp}}{\delta P_{opt}} = \sqrt{\frac{\eta_{qp} N_0 \tau_0 (k_B T_c)^3}{4\Delta^3 V}} P_{opt}^{-1/2} = \frac{\eta_{pb} \tau_{qp}}{\Delta V} \quad (2.28)$$

Here we can see the dependence of changes in the quasiparticle density due to incident light goes like $P_{opt}^{-1/2}$. Experiments have verified the validity of this relationship [33] [43]. However, at low temperatures, the quasiparticle lifetime should increase exponentially, but it was found that there is a maximum to the value [66]. This phenomenon is not well understood, but some recent work has shown that this phenomenon may be due to the trapping of quasiparticles in areas of the metal where Δ is lower than expected [18]

2.4 Microwave Properties

The KIDs throughout this entire thesis all utilize microwave circuitry in order to measure the change in inductance. Microwave KIDs (MKIDs) is generally synonymous with KIDs. The general frequency range that MKIDs are designed for is between about 100MHz and about 5GHz.

2.4.1 Scattering Parameters

A primary measurement made in microwave circuits is the scattering of the microwave signal through the entire system. The scattering parameters are defined by a matrix with the voltage signals on either end of the two port system.

$$\begin{pmatrix} V_{1,\text{out}} \\ V_{2,\text{out}} \end{pmatrix} = \begin{bmatrix} S_{11} & S_{12} \\ S_{21} & S_{22} \end{bmatrix} \begin{pmatrix} V_{1,\text{in}} \\ V_{2,\text{in}} \end{pmatrix} \quad (2.29)$$

For MKIDs, $V_{2,\text{in}}$ is generally 0 corresponding to no voltage input on the second port. This then leads to the definitions $S_{11} = V_{1,\text{out}}/V_{1,\text{in}}$ and $S_{21} = V_{2,\text{out}}/V_{1,\text{in}}$. S_{21} , the ratio of output signal to input signal, is the scattering parameter of the most interest for measuring MKID signals. S_{11} , the reflections from port 1 back to port 1, is a value we want to be minimized so that the S_{21} signal can be stronger. It is usually more convenient to work in logarithmic units than linear units for S_{21} and S_{11} . We can define a logarithmic unit, decibels, as

$$s = 20\log_{10} | S_{21} | \text{ dB} \quad (2.30)$$

2.4.2 *I* and *Q*

The alternating current used in MKID circuitry takes the form of a sinusoid. A general form for any sinusoidal signal is

$$b(t) = A(t)\cos(\phi(t))\sin(2\pi ft) + A(t)\sin(\phi(t))\cos(2\pi ft) = A(t)e^{i(2\pi ft + \phi(t))} \quad (2.31)$$

where A is the time-dependent amplitude, ϕ is the phase, f is the frequency, and t is the time. The real component of this equation is the in-phase component, I and the imaginary

part is the quadrature component, Q .

We can easily write an equation for the magnitude and phase of S_{21} based off the I and Q components. The magnitude is $A(t) = |S_{21}| = \sqrt{I^2 + Q^2}$ and the phase is $\phi = \arctan(Q/I)$.

2.4.3 RLC Circuits

RLC resonant circuits create an easy method of measuring changes in the impedance of a system. Figure 2.1 shows a diagram of an RLC circuit and the S_{21} signal created by it. As seen in the figure, an RLC circuit creates a resonance at a frequency given by $\omega_0 = 1/\sqrt{LC}$. The peak energy stored in the circuit, E , divided by the average energy dissipated, P_{dis} is known as the quality factor, Q and is related to the depth of the resonance.

$$Q = \omega_0 \frac{E}{P_{dis}} \quad (2.32)$$

The purpose of the coupling capacitor in figure 2.1 is to introduce a loss mechanism to be able to control the quality factor. With this capacitor, we can further break Q into two components. Q_i is the intrinsic quality factor that comes from the RLC circuit and Q_c the coupling quality factor that comes from the coupling capacitor. These are related to Q by

$$\frac{1}{Q} = \frac{1}{Q_i} + \frac{1}{Q_c} \quad (2.33)$$

The formula for Q_i is easily derived to be $Q_i = \omega_0 RC$. A derivation for the formula for Q_c can be found in [4] and the equation is

$$Q_c = \frac{C}{\omega_0 RC_c^2} \quad (2.34)$$

Going back to the beginning of this section, the transfer function, S_{21} , for the RLC circuit can be calculated in terms of the resonant frequency and the quality factors. From [52], we have for our two-port system

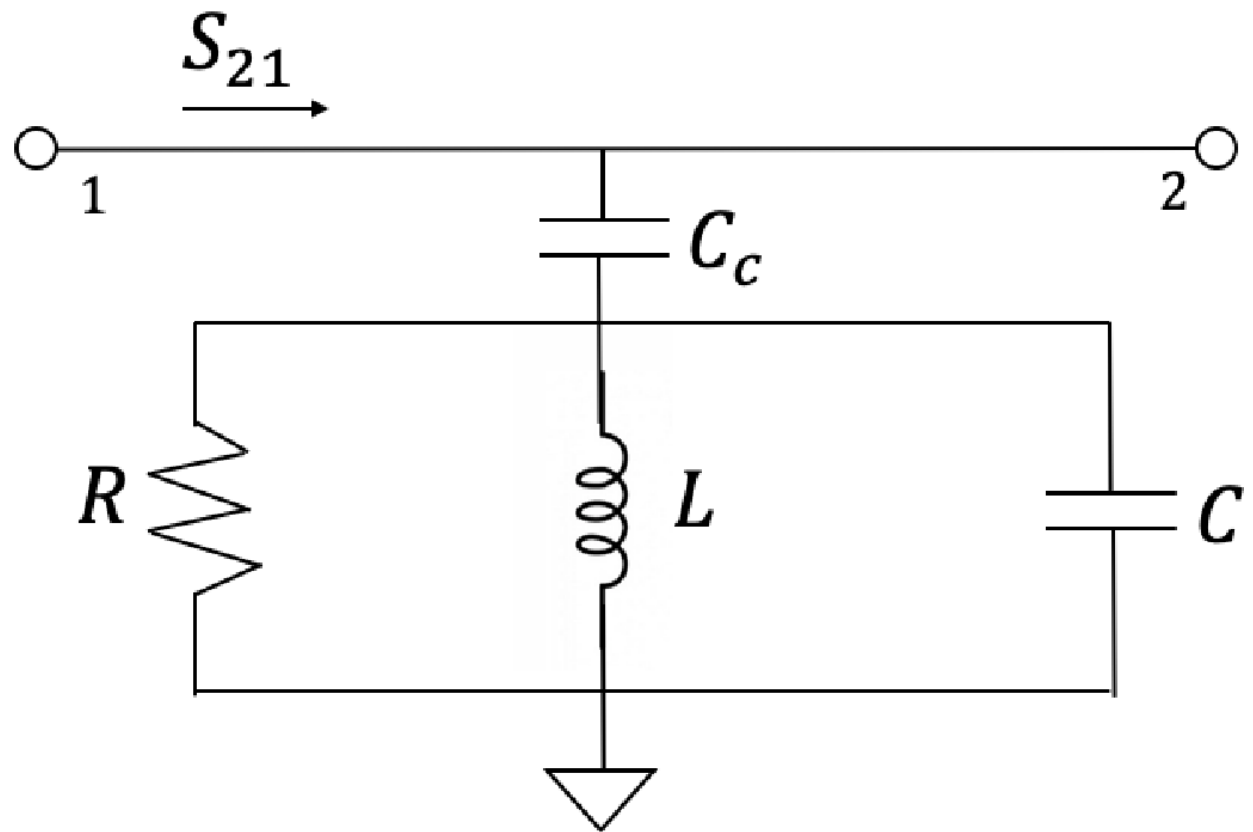


Figure 2.1: A diagram of a parallel RLC circuit with a coupling capacitor. The signal enters from port 1 on the left and exits through port 2 on the right. A coupling capacitor separates the RLC circuit from the feedline in order to control the coupling quality factor. [60]

$$S_{21} = \frac{2}{2 + Z/(2R)} \quad (2.35)$$

The impedance Z is the sum of the impedances of the coupling capacitor and the resonant circuit

$$Z = Z_{cc} + Z_{res} = -\frac{i}{\omega C_c} + \frac{R}{1 + 2iQ_i \frac{\omega - \omega_0}{\omega_0}} \quad (2.36)$$

The assumption that $\omega - \omega_0$ is small is assumed. Now, using the approximations $Q_i \gg 1$ and $Q_i(\omega - \omega_0)^2 \ll 1$, we can rewrite equation 2.35 as

$$S_{21} = 1 - \frac{Q/Q_c}{1 + 2iQ \frac{\omega - \omega_0}{\omega_0}} \quad (2.37)$$

2.4.4 Asymmetry and Bifurcation

Impedance mismatches between the circuit and the other microwave components can lead to asymmetries in the shape of the resonance curve. The impedance mismatch can be easily accounted for by allowing Q_c to be complex, i.e. \tilde{Q}_c . A full derivation of why this is the case can be found in [26]. This implies that the total quality factor Q is also complex. The "real" quality factors can still be found using $1/Q_c = \Re(1/\tilde{Q}_c)$.

Equation 2.37 breaks down if the resonator is driven at high powers. At high powers, the resonator response is no longer linear due to the nonlinear kinetic inductance of the superconducting film. A detailed derivation of the below equations can be found in [58]. The first step to incorporate the nonlinear behavior is to define the fractional frequency shift $x = (\omega - \omega_0)/\omega_0$, which replaces the corresponding term in equation 2.37. Then, we can incorporate the nonlinearity into the fractional frequency shift by redefining it such that x becomes

$$x = \frac{\omega - \omega_0}{\omega_0} + \frac{2Q^2}{Q_c} \frac{1}{1 + 4Q^2x^2} \frac{P_g}{\omega_1 E_*} \quad (2.38)$$

Here, P_g , E_* , and ω_1 are the generator power, an energy scale factor, and the nonlinear resonance frequency respectively. This can be simplified by making the substitutions of $y = Qx$ and $y_0 = Q\frac{\omega - \omega_0}{\omega}$ and introducing the nonlinearity parameter

$$a = \frac{2Q^3}{Q_c} \frac{P_g}{\omega_1 E_*} \quad (2.39)$$

to become

$$y = y_0 + \frac{a}{1 + 4y^2} \quad (2.40)$$

When $a \gtrsim 0.8$, y bifurcates and there are three solutions to the S_{21} equation. Two of the solutions result from sweeping up in frequency and sweeping down in frequency as seen in figure 2.2. The third solution is unstable and generally not observed. Driving the resonator at higher input powers leads to a stronger signal. However, operating slightly below bifurcation but still in the nonlinear regime leads to better response than operating solely in the linear regime [48].

2.5 Responsivity

We can now build off equation 2.28 to relate changes in resonance parameters to changes in optical power. The inductance $L = L_g + L_k$ of the resonator is the sum of the geometric and kinetic inductances. During photon absorption, only the kinetic inductance is changed and the fractional frequency shift is

$$\delta x \frac{\omega - \omega_0}{\omega_0} = \frac{\delta \omega}{\omega} = -\frac{1}{2} \frac{\delta L}{L} = -\frac{\alpha}{2} \frac{\delta L_k}{L_k} \quad (2.41)$$

where $\alpha = L_k/L$ is the kinetic inductance fraction. Similarly, we can compute how the internal quality factor changes

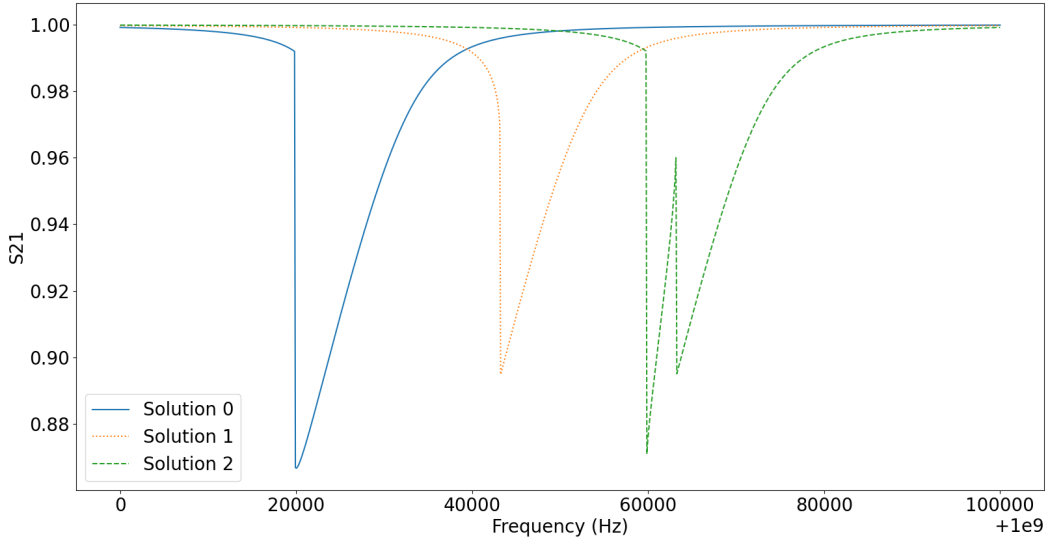


Figure 2.2: A plot showing the three solutions of a bifurcated resonator. The following parameters were used to generate the solutions: $Q = 2 * 10^5$, $Q_c = 1.5 * 10^6$, $a = 2$, and resonance frequencies of 1.00003, 1.00005, 1.00007 GHz for solutions 0, 1, and 2 respectively.

$$\frac{1}{Q_i} = \frac{R}{\omega_0 L} \rightarrow \delta \frac{1}{Q_i} = \frac{\alpha \delta R}{\omega L} \quad (2.42)$$

Using the detector quasiparticle response to optical power, equation 2.28, one can derive the detector response in both fractional frequency shift and internal quality factor [66] [4]

$$\frac{\delta x}{\delta P_{opt}} = \frac{\alpha \gamma \eta_{pb} \tau_{qp}}{4 N_0 \Delta_0^2 V} \left(1 + \sqrt{\frac{2 \Delta_0}{\pi k_B T}} \exp\left(-\frac{\hbar \omega}{2 k_B T}\right) I_0\left(\frac{\hbar \omega}{2 k_B T}\right) \right) \quad (2.43)$$

$$\frac{\delta Q_i^{-1}}{\delta P_{opt}} = \frac{\alpha \gamma \eta_{pb} \tau_{qp}}{\pi N_0 \Delta_0^2 V} \sqrt{\frac{2 \Delta_0}{\pi k_B T}} \sinh\left(\frac{\hbar \omega}{2 k_B T}\right) K_0\left(\frac{\hbar \omega}{2 k_B T}\right) \quad (2.44)$$

2.6 Noise Properties

2.6.1 Generation-Recombination Noise

As discussed in section 2.3, there are fluctuations in the number of quasiparticles in a superconducting film due to generation and recombination from the imperfections of the material. Just as the resonator parameters δx and Q_i change with respect to optical power, they also vary with changes in quasiparticle density. Afterall, the optical power breaking Cooper pairs is the source of the resonator response. This continuous generation and recombination gives rise to the fundamental noise element of KIDs (GR noise).

Noise terms in MKIDs are generally expressed as noise-equivalent powers (NEPs). NEP is defined as the signal power that would give rise to a signal-to-noise (SNR) ratio of one in a one hertz output bandwidth. Typical NEPs for MKIDs are between 10^{-17} to 10^{-20} . The NEP for GR noise is given by [56] [64]

$$\text{NEP}_{gr} = \frac{2\Delta}{\eta_{pb}} \sqrt{\frac{N_{qp}}{\tau_{qp}}} \quad (2.45)$$

The GR noise spectrum S_{gr} is flat in frequency until the quasiparticle lifetime where the time scales are short enough that the quasiparticles can't react.

$$S_{gr} = \frac{4N_{qp}\tau_{qp}}{1 + (\omega\tau_{qp})^2} \quad (2.46)$$

GR noise in a detector can be reduced in a number of ways. One can choose a metal with a smaller band gap $\text{NEP}_{gr} \sim \Delta^{5/2} \exp(-\Delta/k_B T)$, create inductors with a smaller volume $\text{NEP}_{gr} \sim V^{1/2}$, or reduce the temperature of the detector $\text{NEP}_{gr} \sim T^{1/2} \exp(-\Delta/k_B T)$.

2.6.2 Photon Noise

In the mm and submm regime, MKIDs are generally detecting a constant stream of photons and not single photon counting due to the Fano limit. Thus, another source of noise in the

detector is due to the random arrival rate of photons. The NEP associated with this is [6]

$$\text{NEP}_{ph} = \sqrt{2Ph\nu(1 + mB)} \quad (2.47)$$

where P is the power absorbed, ν is the photon frequency, and $(1 + mB)$ is a correction to Poisson statistics due to wave bunching.

Furthermore, the photon integration will also increase the average number of quasiparticles such that

$$N_{qp} = \frac{P\tau_{qp}}{\eta_{pb}\Delta} \quad (2.48)$$

This will then lead to an increase in NEP_{gr} and can become the dominant source of quasiparticles in the high loading limit.

2.6.3 Two-Level System Noise

Two-level system (TLS) noise is another contributing factor to detector sensitivity and the least well understood [25]. TLSs form in amorphous dielectrics which can include oxide layers on the surface of a substrate. The amorphous dielectrics have tunneling states that have electric dipole moments that can couple to electric fields. This coupling changes the effective dielectric properties of the material which in turn affects the resonant frequency of KIDs.

TLS noise does not have a complete microscopic model, but there are a number of empirical relations that have been discovered. Creating an effective dielectric constant from observations, [25] formed these two equations for how the KID properties change.

$$Q_{i,\text{TLS}}^{-1} = F\delta_{\text{TLS}}^0 \tanh\left(\frac{\hbar\omega}{2k_B T}\right) \quad (2.49)$$

$$\delta x = \frac{F\delta_{\text{TLS}}^0}{\pi} \left[\Re\Psi\left(\frac{1}{2} - \frac{\hbar\omega}{2i\pi k_B T}\right) - \log\frac{\hbar\omega}{2\pi k_B T} \right] \quad (2.50)$$

F is a filling factor that depends on how much the TLS host material volume fills the resonator volume, δ_{TLS}^0 is the intrinsic loss tangent, and $\Re\Psi$ is the real part of the complex digamma function Ψ .

Going further, the spectral density density of TLS noise is material and geometry dependent, but has the following scaling relation

$$S_{\text{TLS}} \propto T^{-2} f^{-1/2} P_r^{-1/2} \quad (2.51)$$

There are a number of methods one can use to try to reduce TLS noise. Operating at higher temperatures is the most straightforward, but does elevate GR noise. Another technique is reducing F by trying to have as little electric field energy stored in the amorphous material as possible. One way this can be achieved is by increasing the gap spacing of an interdigitated capacitor. One more method is to utilize more than one material when designing a KID. For example, aluminum has higher levels of TLS noise but has a lower band-gap energy that is important for mm and submm sensitivity. Thus one could make only the inductor out of aluminum and the capacitor out of niobium which has lower levels of TLS noise [25]

2.7 Lumped-Element KIDs

Lumped-Element KIDs (LEKIDs) are the subset of KIDs used in this thesis. This refers to KIDs where the components of the resonant circuit are each in their own defined lumped. Other types of KIDs can have the inductor and capacitor consist of the same component in the design such as the original co-planar waveguide design by [17]. LEKIDs were developed by [21] in 2007. The benefit of separating out the components is that the inductor can have a more uniform current distribution and sensitivity because the capacitor has non-

uniform current throughout. Furthermore, The design parameters are more easily controlled through modifications to specific elements that are independent of the other components. For example, the resonant frequency can be controlled by the size of the capacitor and Q_c can be controlled by the size of the coupling capacitor. The main drawback of LEKIDs is they take up a much larger footprint on a device and so the ability to multiplex can be less than other KID designs.

CHAPTER 3

DESIGN, FABRICATION, AND TESTING OF KIDS FOR THZ SPECTROSCOPY

3.1 The RAxDEx Idea

In order to avoid the challenges of improving existing FIR detector design mentioned in section 1.1, we are developing an on-chip filter bank to act as the spectrometer of our detectors. Experiments, such as SuperSpec[31, 37], have demonstrated large-format on-chip spectrometers, albeit at millimeter wavelengths. In the FIR regime, the same filter bank architecture would lead to unacceptable dielectric loss in the feedline. Instead, we propose to use a rectangular waveguide to mitigate these losses (see fig 3.1), similar to the design of the WSPEC instrument [11]. We utilize microcavity resonators connected to the waveguide feedline in order to select individual frequencies of radiation. A single, low-quality microcavity resonator at terahertz (THz) frequencies has previously been created and tested[27]. Similar work of etching silicon to create terahertz waveguide components such as an orthomode transducer has been done before [34]. After radiation passes through the microcavity resonator, the radiation is absorbed by detectors and in this work, we use MKIDs to accomplish this. The MKIDs used in this work will overcome many of the issues past experiments have faced. Our MKIDs are required to be cooled to less than 300mK so the telescope will have to be at much colder temperatures. In addition, MKIDs provide a straightforward method for multiplexing large format arrays on a single device. This work will detail the design and coupling of MKIDs to a rectangular waveguide filter bank for FIR wavelengths. We discuss the focal plane design, MKID design, fabrication steps, and testing of a prototype device.

3.2 Focal Plane Design

This experiment utilizes a unique two silicon wafer design to create a waveguide for an on-chip spectrometer between 1.4 and 2 THz. First a trench with disk resonators branching from it is etched into the silicon with one end of the waveguide at the end of the chip (see Fig. 3.2). The trench is gold coated and forms three sides of the waveguide. The high-conductivity gold

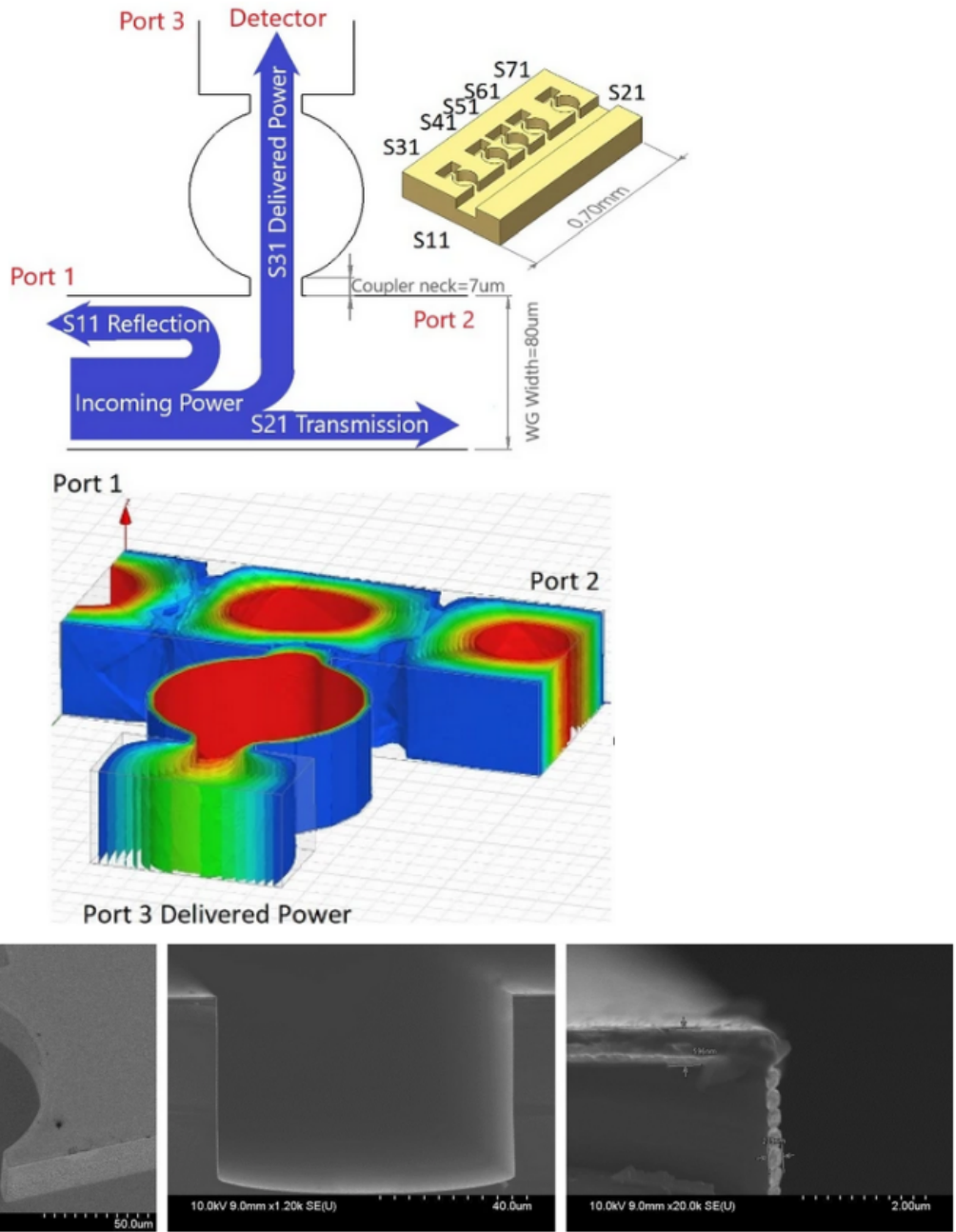


Figure 3.1: *Top*: A diagram of a rectangular waveguide with a microcavity resonator. The terahertz signal enters through port 1 and leaves through port 2. Specific frequencies are selected by the cavity resonator and exit through port 3 to the detector. *Middle*: An HFSS simulation of the electric field distribution for a on-resonance signal. *Bottom*: Scanning electron microscope images of a fabricated spectrometer. The images represent from left to right the top view, the cross-section, and the corner detail. The gold coating is 596nm on the top surface and 239nm on the side walls. [50]

film is necessary to ensure low loss in the waveguide. A second wafer, on which the detectors have been fabricated, also has a gold coating so that it acts as the top of the waveguide. Light incident on the edge of the silicon chips travels down the center waveguide before being picked off by a resonance cavity and absorbed by a detector. Alignment of the two chips is achieved with two dowel pins mounted in the device box and a hole and slot pattern etched into the devices. This technique has been shown to align the two chips to within a few microns [59]. In order to press the two chips together and avoid any gaps in the waveguide, we use three spring-loaded plungers with an acetal plastic nose (McMaster-Carr part no. 2467A15) mounted in the box that apply pressure to the chips as they are screwed in. The tip provides between 1.3 and 2.7 lbs of force per plunger depending on how far compressed it is. The waveguide design has been tested and verified using a room temperature VNA to measure the transmission and filter properties of a 4-port 10x10mm chip, the details of which are found in [49]. The peak frequencies were within 0.4% of the design targets and the Q-values were around 100 which is consistent with achieving a $R \sim 100$ spectrometer.

The ultimate goal of this collaboration is to produce an $n \times n$ pixel device targeting $R = 100$ and a noise equivalent power of $10^{-18} \text{W Hz}^{-1/2}$. Including the entire spectrometer and detector array, the resulting focal plane cube for this goal will only be a few tens of millimeters on a side.

3.3 Absorber and KID Design

The MKIDs are designed to couple directly to the waveguide using an annular absorber for the inductor (see fig. 3.3). The absorber design is based off the work done by [12] using the Model-I design. The main modification to the design is the annulus has a small break where the two inductor lines connect. This feature is not shown in the simulation but was tested and had negligible effects. The absorber sits on the top surface of the waveguide and is fabricated from 25nm thick aluminum. This thin layer is necessary to keep the inductor volume low (approximately $16\mu\text{m}^3$) in order to achieve low detector noise of $\text{NEP} \sim 5 * 10^{-20} \text{W Hz}^{-1/2}$

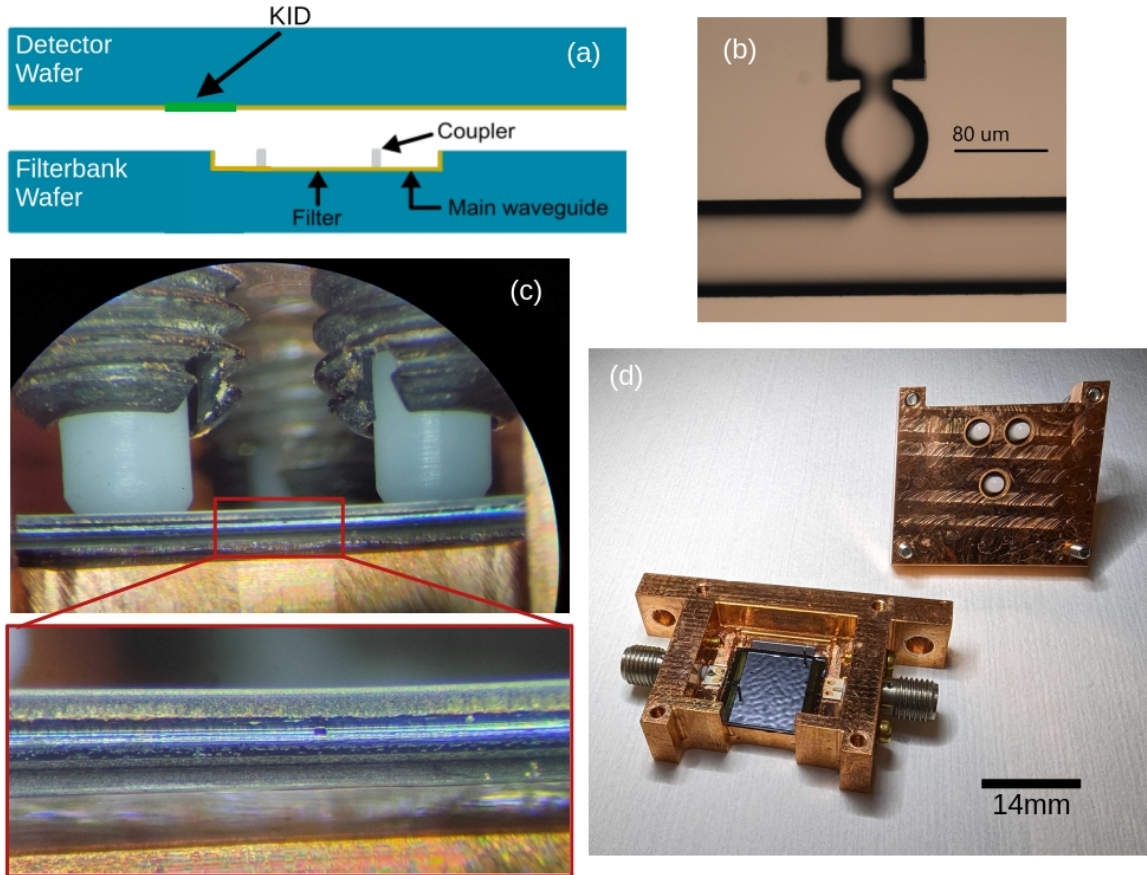


Figure 3.2: Waveguide geometry and box design. (a) A schematic drawing of the two wafer design. The filterbank wafer has gold coated trenches and the detector wafer has gold except where the MKIDs and readout lines are. When pressed together, they form a closed waveguide. (b) A top-down microscope image of the main waveguide and one filter before gold coating. (c) An edge on view of the two-chip stack with a zoom in of the $80 \times 160 \mu\text{m}$ waveguide. Also in view are the spring plungers that press the two chips together. (d) The prototype device box. Shown are the alignment pins, launcher boards for wire bonding, SMA connectors to send and receive the microwave signal, and the spring plunger layout.

[32]. Simulations of the antenna design and placement using Ansys HFSS show that the antenna has the ability to absorb at least 60 percent of the power in our band that passes through the waveguide filter. Furthermore, unlike the Model-I design, the dark devices that are mentioned in this thesis do not have a metallized ground plane on the opposite surface of the dielectric. Lastly, the simulations were performed assuming the silicon behind the absorber is etched away to form a backstop. This step has not been performed in the dark devices but a similar technique to create the thin membranes has been demonstrated in Chapter 4 and also in the creation of parallel plate capacitors using a crystal silicon dielectric.

Two thin aluminum lines come out of the annulus to connect to either side of an interdigitated capacitor (IDC) to form the resonant circuit of the MKIDs (see Fig. 3.4). The IDCs are fabricated out of niobium and the fingers have a width of $3\mu\text{m}$ and a spacing of $6\mu\text{m}$. The MKIDs are capacitively coupled to a niobium co-planar waveguide for read-out. The IDCs have a long rectangular shape which optimizes the number of KIDs that can be placed along the THz waveguide before the waveguide loss becomes too large. The capacitor fingers near the read-out line are oriented perpendicular to the feedline to minimize coupling and the rest are rotated 90 degrees to make the capacitors more robust to fabrication defects and reduce inductance in the capacitor. The resonant frequency placement is controlled by the length of the capacitors and the coupling quality factors by the length of the coupling capacitor. The design coupling quality factor is $5 * 10^4$ and the expected internal quality factor is $1 * 10^5$. The KID design was refined using Sonnet to simulate the resonant circuit and determine the appropriate variations in the IDCs and coupling capacitors.

3.4 Fabrication

The devices are fabricated on $500\mu\text{m}$ double-side polished, high resistivity silicon wafers. Fabrication of the detector wafer begins with a Maskless Laser Aligner (MLA) lithography and gold deposition. The gold is sputtered onto the wafer to reach a thickness of 600nm. Then a liftoff step where acetone is used to dissolve the photoresist is performed to remove

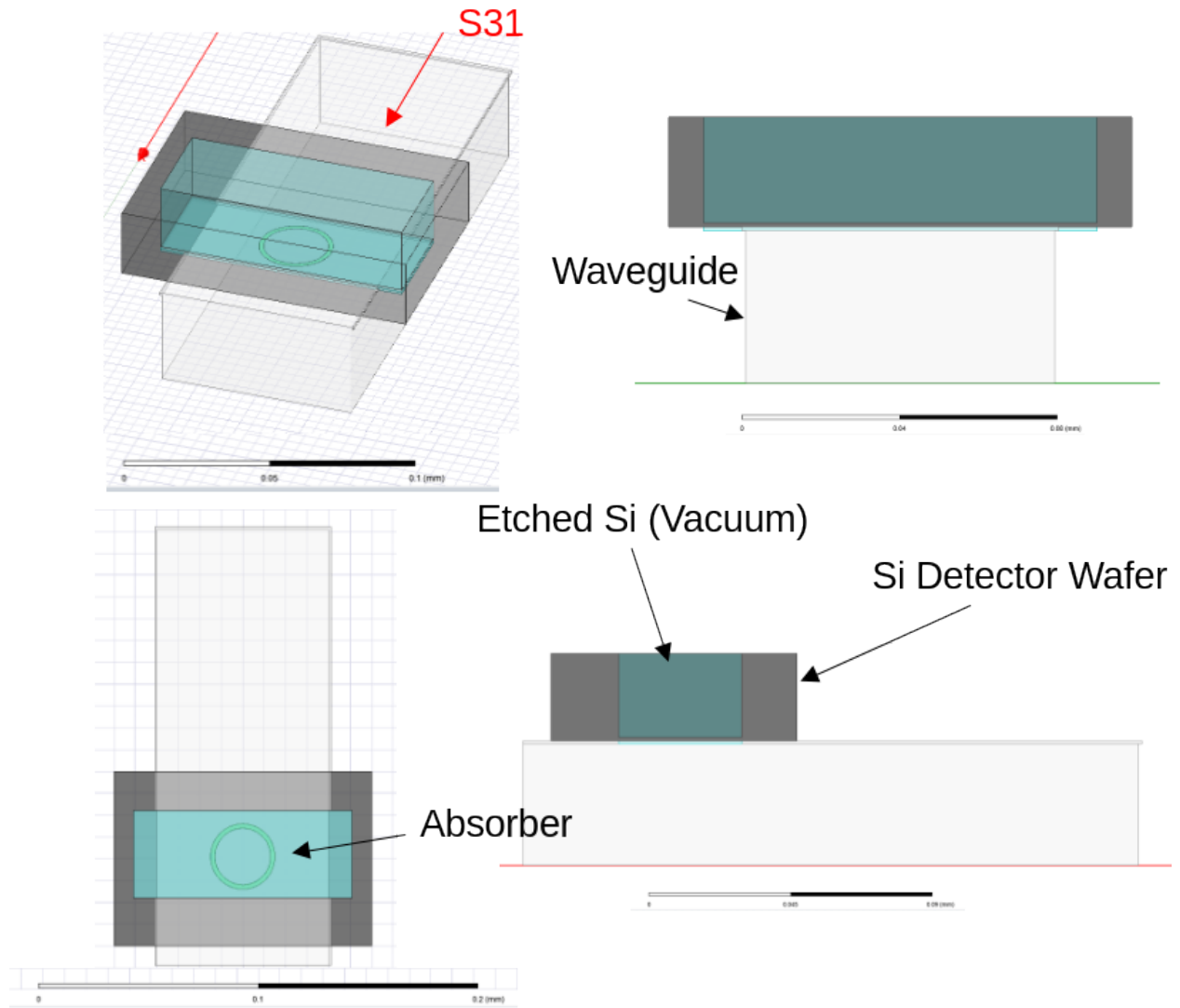


Figure 3.3: Different views of the simulations of the detector absorber in relation to the waveguide. *Top Left*: Isometric view. S31, the signal after passing through the cavity resonator, enters through the far side of the drawing. *Top Right*: Front view. The waveguide forms the bottom part of the simulation and the absorber and silicon wafer sit on top of the waveguide. *Bottom Left*: Top view. The absorber is an annulus that is on a thin piece of silicon on the detector wafer. *Bottom Right*: Right view. The etched area behind the silicon membrane acts as a backstop to reflect the signal that isn't absorbed back into the absorber.

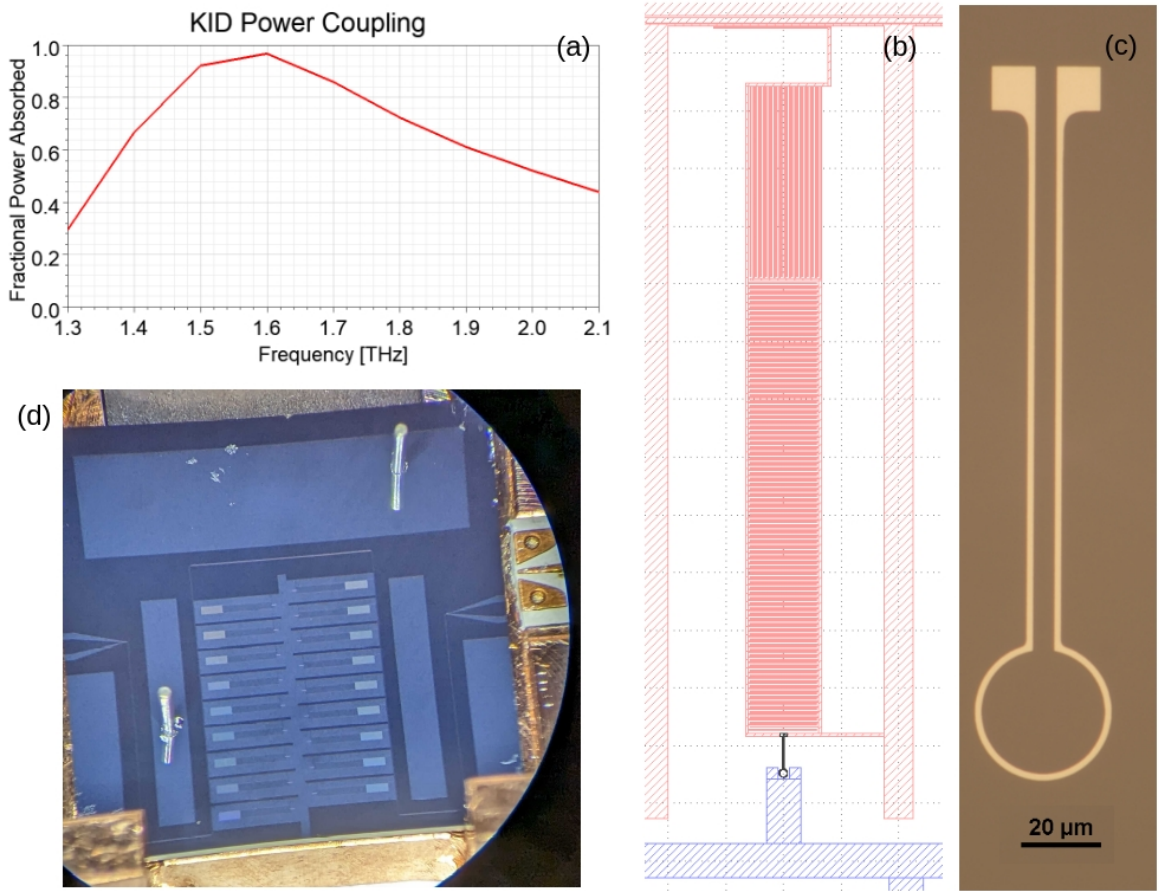


Figure 3.4: Simulations and overall MKID device layout. **(a)** A plot of an HFSS simulation of the absorber on top of the waveguide. The absorber absorbs greater than 60% of the power between 1.4 and 2.0 THz that passes through the waveguide filter. **(b)** Layout of a full MKID. The Au waveguide top is in blue at the bottom. The Al inductor is in black and sits just on top of the waveguide. The Nb IDC, co-planar waveguide, and ground are in red. **(c)** A close up microscope image of the Al inductor and absorber. The absorber is $26\mu\text{m}$ in inner diameter and $2\mu\text{m}$ in width. The large pads are to ensure adequate contact with the Nb IDCs. **(d)** An overview microscope image of the entire 14mm mounted device chip. The waveguide is in the center of the chip and the 18 MKIDs branch off of it.

areas where the gold is unwanted. This gold layer protects the niobium and aluminum layers, which are thinner, when the two wafers are pressed together. The gold layer fabrication was performed by a collaboration member and the details of which are covered in another proceeding [49]. Then, 30nm of Al is deposited using an AJA Ultra High Vacuum (UHV) physical vapor deposition sputtering tool. The chamber pressure was typically \sim 1e-9 Torr at the time of deposition. The Al was deposited with 5mTorr Ar gas pressure and a deposition rate of \sim 6nm/min. The Al is then patterned using MLA lithography with AZ1512 photoresist, given a post-exposure bake at 115C for 60s and developed in AZ 1 : 1 developer. For all AZ1512 processes, the dosage is 120mJ/cm² and the developing time is approximately 1 to 2 minutes. Finally, the Al is etched using an Al acid etch containing phosphoric, acetic, and nitric acids for about 60s. During the etch, the glass is continuously agitated to improve uniformity in the etch. The stopping criteria for the etch is to remove the wafer after approximately 10s after the wafer looks visibly free of Al. It is very important when performing a wet etch to minimize the time spent in the acid to prevent undercutting. The photoresist is removed using a sonicated acetone bath for 15 minutes followed by an IPA and DI water rinse. The wafer is then dehydrated in a vacuum oven at 110C for 180s. The Nb layer follows the same procedure with a few changes. First, an ion mill is performed before the Nb is deposited to remove the oxide layer from the surface of the Al. The ion mill is performed in the same chamber as the Nb is deposited. The ion mill uses 30sccm of Ar for approximately 2 minutes at an etch rate of a few nm per minute. Then the Nb is deposited using the same sputter tool but with an Ar pressure of 10mTorr and a deposition rate of \sim 5nm/min. The thickness of the Nb layer is approximately 225nm, however the exact thickness is unimportant since it is not part of the inductor. The Nb lithography is identical to the Al except the developer is AZ 300 MIF. AZ 300 MIF has better performance but etches Al, so it can only be used when the Al is protected by the Nb. Lastly, the Nb etch is performed in a Plasma-Therm ICP Flouride Etch tool with a combination of CHF₃ and CF₄ as the etchants. The etch time is approximately 5 minutes and a similar stopping

criteria to the wet etch is used except that the overetching is done for 30 seconds. The photoresist is more difficult to remove after a F1 etch because the F1 reacts with the photoresist. To remove the photoresist, the wafer is put into an O₂ plasma ash at 70C and 300W for 240 seconds. With the crust removed, the wafer is soaked in NMP at 80C overnight and followed with an ultrasonic bath, IPA rinse, and DI water rinse. To remove the finished chips from the silicon wafer and create the dowel pin alignment holes, we use a Plasma-Therm Deep Si Reactive Ion Etch (DRIE) that runs the Bosch Si process. The photoresist used for the lithography before the DRIE is a 20 μ m thick layer of double spun AZ4620. The resist is spun at 1500rpm with a softbake at 110C of 10 minutes in between and 15 minutes afterwards. The wafer is then given 30 minutes to rehydrate to prevent resist bubbling or cracking during exposure. The thick layer of photoresist is needed to withstand the etchants until the entire 500 μ m wafer thickness is etched. Great care must be taken when heating and cooling the photoresist after exposure as it is prone to thermal cracking if the temperature changes too rapidly. The photoresist needs to be hard baked at 110C for approximately 45 minutes after developing in AZ1:4. The preferred method is a vacuum oven that starts at room temperature and gradually reaches 110C. Cooling is done by slowing opening the door to the vacuum oven several minutes. The Si etch takes around 1300 cycles and is deliberately slow to minimize scalloping at the edges. The remaining photoresist is removed the same way as for the Nb layer.

The waveguide wafers start fabrication in a similar manner with the same type of silicon wafer. They are first DRIE etched to create the channel for the waveguide. Then, before removing the photoresist, 600nm Au is deposited to fully coat the waveguide walls. Then, the photoresist is removed and all that remains is the Au coated channels. Those steps are performed by a collaboration member. Next, the protective etch to remove Si near the MKIDs and readout line on the detector wafer needs to be performed. This step is particularly difficult because the waveguide channels create an uneven surface for spinning the photoresist. To overcome this, a double layer of AZ4620 spun at 1500rpm is used as

above even though the etch is much shorter and does not need a thick layer. The first layer effectively fills in the channels but leaves some exposed Si near the top of the channel's edges due to surface tension. The second layer fully covers the now much smoother surface with little difficulty. The wafer can now be etched about $300\mu\text{m}$ using the same DRIE process as above. Lastly, the chips need to be removed from the device and the alignment pin holes need to be etched. This process is the same as for the KID wafer except that we only need to etch through about $200\mu\text{m}$ since we can etch the first $300\mu\text{m}$ in the previous step. This last etch is done on the backside of the wafer to make the photoresist spinning process feasible and the frontside is coated with a protective layer of photoresist to prevent scratching.

3.5 Test Setup

In order to test the devices, they are cooled to between 30mK and 300mK using a BlueFors He-3 dilution refrigerator. This type of fridge utilizes a mixture of He-3 and He-4 isotopes. The He-3 is cycled through the system using vacuum pumps and the mixture separates into a concentrated (He-3 rich) phase and a dilute (He-3 poor) phase below 800mK . Inside the mixing chamber, the He-3 is moved from the concentrated to the dilute phase taking heat with it in the process. The evaporated He-3 is moved into the still where it gets recycled to the beginning of the cycle.

The setup has a variety of microwave components both outside and inside the cryostat. There are two measurement setups. One utilizes a vector network analyzer (VNA) to perform S_{21} frequency sweeps and the other is a single-tone homodyne readout to study detector noise. Figure 3.6 provides an overview of the components involved in the homodyne system. However, everything between the variable attenuator and the first low pass filter are identical. In words, the signal is generated via either the VNA or synthesizer depending on the measurement. Then the signal goes through a variable attenuator at room temperature before entering the cryostat. There is a 20dB attenuator on the 4K cryostat stage and another 30dB of attenuation on the mixing chamber stage. After the signal passes through the

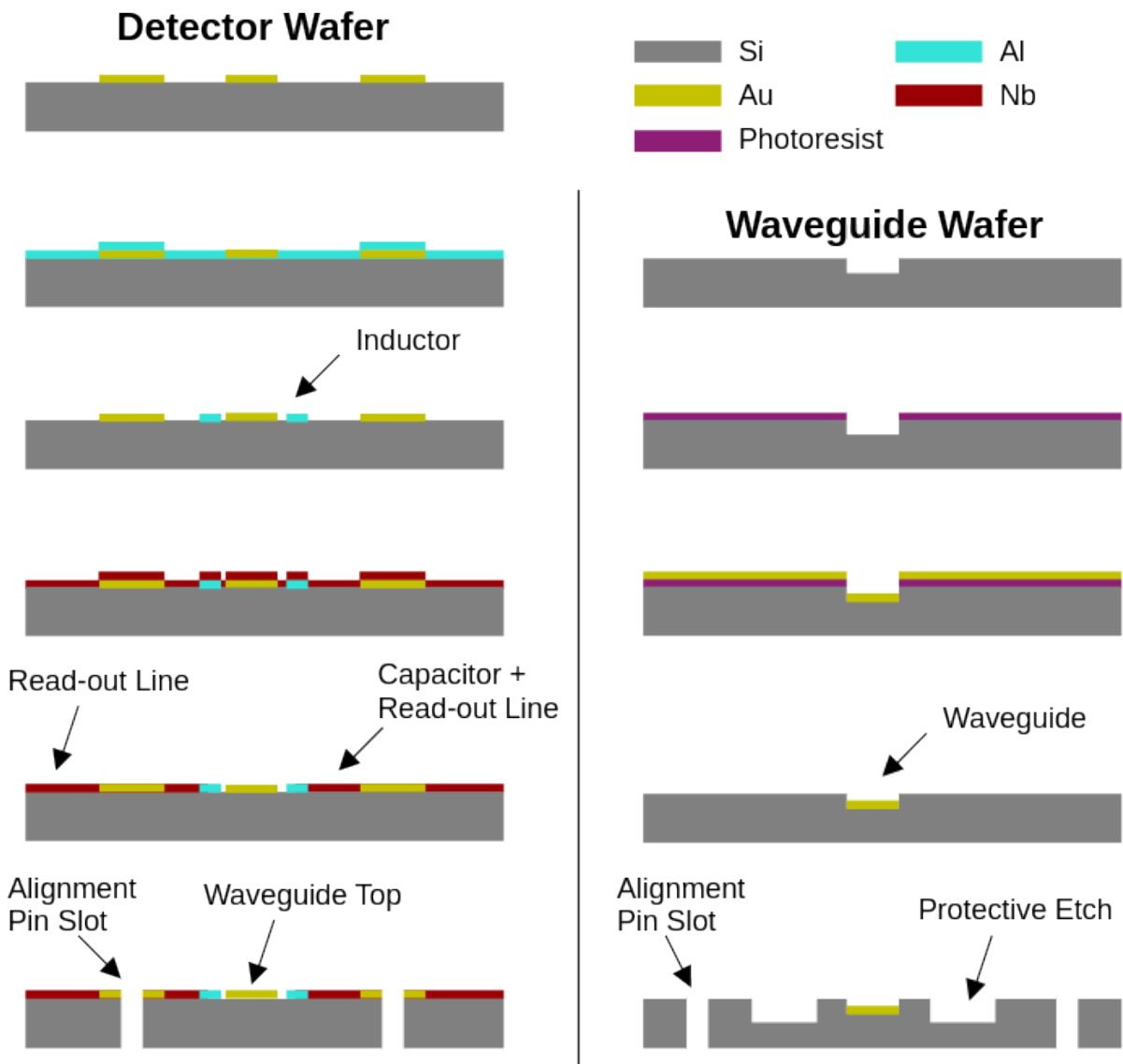


Figure 3.5: A diagram of the fabrication steps for both the detector wafer and the waveguide wafer. The detector wafer steps shown are the initial gold layer, the aluminum deposition, the aluminum etch, the niobium deposition, the niobium etch, and the alignment pin etch. For the waveguide wafer, the steps are the waveguide etch, a photoresist deposition, the gold deposition, the gold lift-off, and the protective and alignment etches.

device, it enters a cold amplifier on the 4K stage that provides about 20dB of gain. The signal is then fed through a 1400MHz low-pass filter and is sent through a room temperature amplifier with a gain of about 35dB. Finally the signal either enters port 2 of the VNA or it is mixed with the original signal and sent to an analog-to-digital converter.

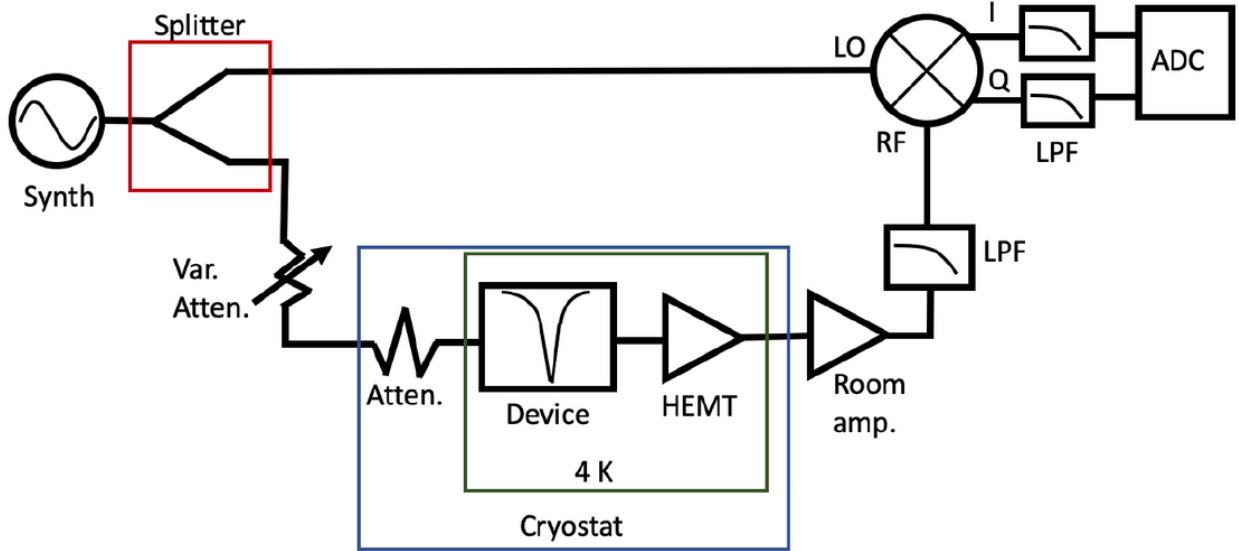


Figure 3.6: A diagram of the microwave components used in a single-tone homodyne measurement.

3.6 Results

The chips are held in a box made from high conductivity copper with two SMA connectors to send the signal through (see Fig 3.2). Two prototype devices have been fabricated and tested so far and the results presented here reflect the performance of the second generation device. Data from the 18-channel prototype device are shown in Fig. 3.7. The device yielded all 18 resonances however, there was a dichotomy in the Q_c of the resonances. 6 of the resonances had a Q_c of about $1 * 10^4$ and the others were clustered around $1 * 10^5$. It is unclear what caused this split around the desired Q_c of $5 * 10^4$, but it may be related to which side of the waveguide the resonances are on since all of the low Q_c resonances are on the same side. Q_i of the resonances from this device were lower than expected and averaged about

$1 * 10^4$. We suspect this may be due to contamination of our Al in the sputtering chamber as the Q_i of recent similar devices fabricated in the same tool have also shown lower than expected Q_i . The sputter tool also contains tantalum and rhenium that may be the source of the contamination. Temperature sweeps demonstrate how the KID reacts to changes in the number of quasiparticles. The attenuation sweeps allow us to find the optimal power to drive the resonators near the onset of bifurcation where the resonance becomes nonlinear and the detector is most sensitive. The noise spectra shows the fractional frequency noise of one resonance relative to the off-resonance noise. Fits were performed to the off-resonance data to obtain the anti-aliasing filter roll-off and amplifier parameters. Then we fit the on-resonance profile keeping the filter roll-off parameters constant and obtain a resonator time constant of $\tau = 3.5\mu\text{s}$. This time constant is close to the resonator roll-off of $1.5\mu\text{s}$ and noise measurements at a second temperature support this roll-off being the resonator roll-off. The noise will likely improve to show the quasiparticle generation-recombination noise once the suspected Al contamination is removed.

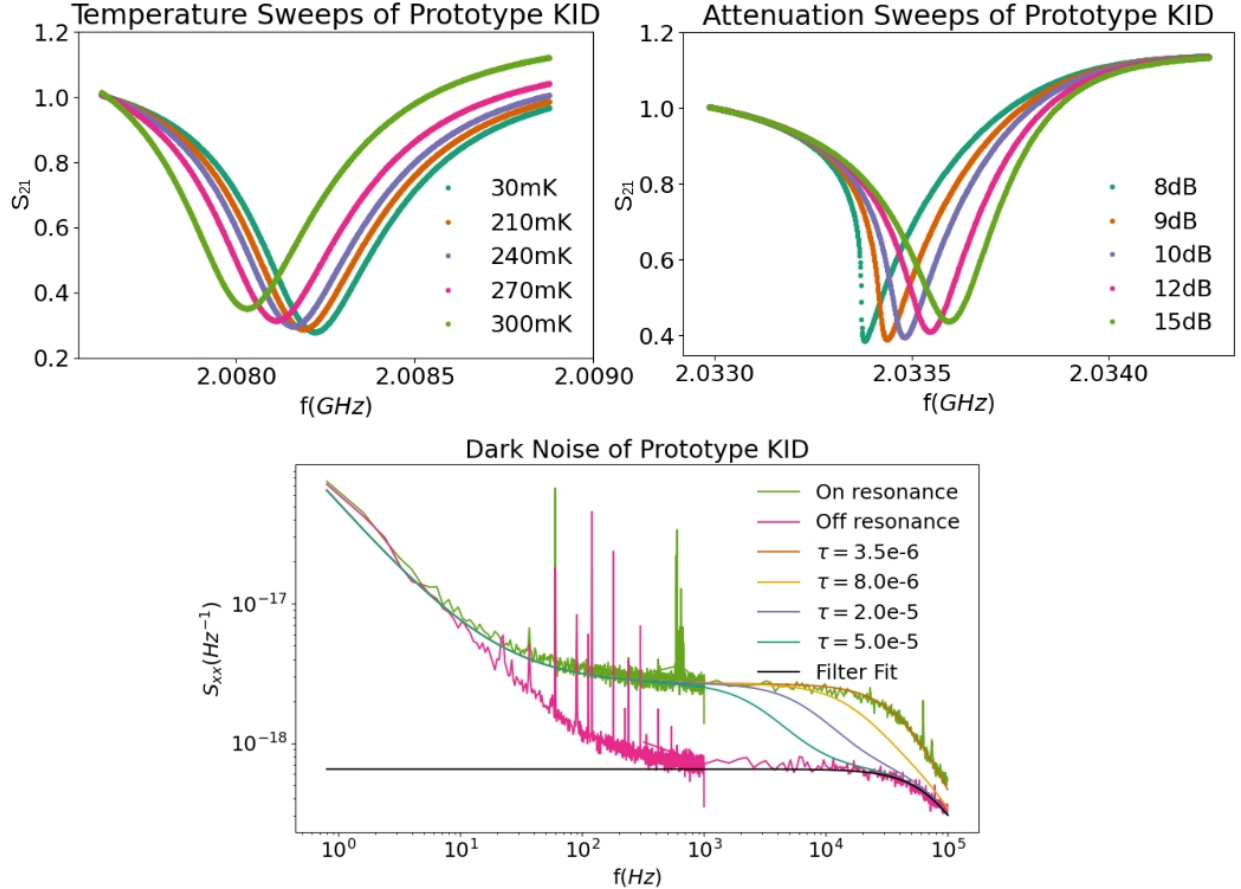


Figure 3.7: Test results from one resonance on a prototype device. *Upper Left:* S_{21} VNA sweeps of one resonance with temperature varying from 30mK to 300mK. Temperatures 60mK to 150mK are omitted since the resonance only starts to move at approximately 180mK. *Upper Right:* S_{21} VNA sweeps of one resonance with the attenuation varied over 7dB. As the attenuation decreases, the resonance bifurcates and becomes non-linear. To obtain ideal noise performance, we need to drive the resonances with as much power as we can as long as they remain in the linear regime. *Bottom:* The fractional frequency noise of a single tone on and off the resonance frequency. We take two separate timestreams at different sample rates to simplify data processing and obtain more accuracy over a wide range of frequencies.

CHAPTER 4

FABRICATION AND TESTING OF KIDS FOR LINE

INTENSITY MAPPING

4.1 The South Pole Telescope Summer Line Intensity Mapping Project

The South Pole Telescope Summertime Line Intensity Mapper (SPT-SLIM) is a pathfinder experiment to demonstrate the capability of on-chip, large-format mm-wave spectrometers for LIM [36]. On-chip spectrometers have been demonstrated before (SuperSpec [57], DESHIMA [61], μ spec [9]). We will be pushing the density of detectors further than these experiments, which are already an order of magnitude denser than previous spectrometers. The experiment utilizes aluminum-niobium KIDs to accomplish this goal.

The targeted frequency range of SPT-SLIM is 120-180GHz with $R = \nu/\delta\nu = 300$ spectroscopy. This frequency range covers CO(2-1), CO(3-2), and CO(4-3) in the redshift ranges $0.3 < z < 0.9$, $0.9 < z < 1.8$, and $1.6 < z < 2.8$ respectively. This large redshift range allows SPT-SLIM to probe how cosmic parameters changed throughout the history of the universe. SPT-SLIM plans to deploy at the south pole in the 2024-2025 austral summer.

4.2 Detector Design

MKID/detector design, capacitor types, omt/membrane, number of detectors, inverted ground plane

The design of the SPT-SLIM detector has some similarities to the RAxDEx design described in the previous chapter. See figures 4.1 and 4.2 for diagrams of the detector layout. The main similarities are in the KID design including nearly identical capacitors and a combination of aluminum for the inductors and niobium for the capacitors. The biggest difference is how the light is guided to the inductor. The SPT-SLIM design uses a waveguide-coupled planar orthomode transducer (OMT) that is capable of sending each polarization to its own filterbank [47]. The light is separated into bands using a $\lambda/2$ microstrip filter that is capacitively coupled to the inductor and the mm-wave feedline [54].

The detector utilizes an inverted architecture to help minimize dielectric noise and provide

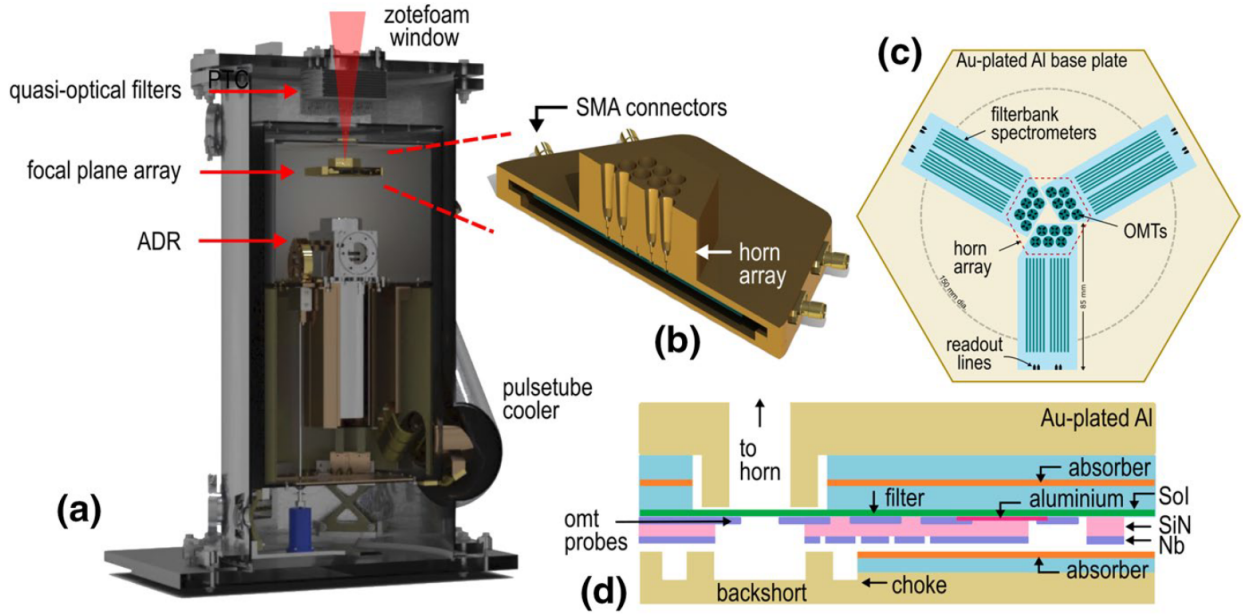


Figure 4.1: **a:** A diagram of the SPT-SLIM cryostat. **b:** A model of the detector box and horn array. **c:** An early SPT-SLIM focal plane design with three separate silicon submodules. **d:** A cross-section diagram of the detector including an absorber and the backshort. [5]

shielding for the photosensitive regions of the detector. The dielectric noise is minimized because the metal resonator layers are deposited on crystal silicon rather than a deposited dielectric. The shielding is provided by the ground plane niobium layer which covers most of the top surface of the detector.

The design parameters of $R = 300$ between 120-180GHz, an $\text{NEP} < 10^{-15} \text{ W/Hz}^{-1/2}$, and the physical layout on a 6in wafer are the primary constraints on the detector design. One of the largest challenges needed to achieve these goals is multiplexing the 200 KIDs per filterbank within a 500MHz bandwidth that conventional microwave electronics are limited to (see figure 4.3 for a simulation of the filterbank). The resonant frequency of the detectors can vary with fabrication errors that lead to small changes in the inductor linewidth. Because the inductor volume is small, these changes can lead to large enough resonant frequency shifts that nearby resonance can sometimes overlap which makes analyzing the resonances extremely difficult. See figure 4.4 for the latest iteration of the detector featuring how it fits on the 6in wafer with other test devices.

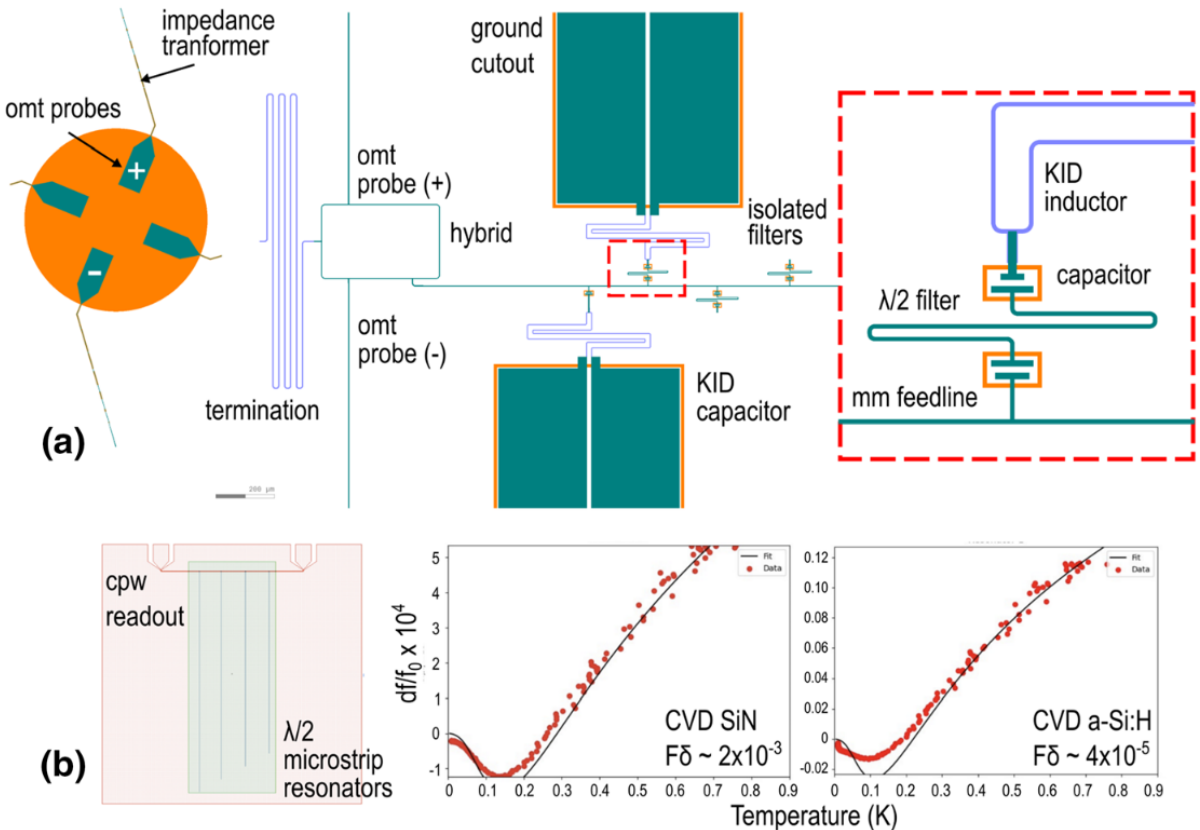


Figure 4.2: **a:** A layout diagram showing key components of the detector architecture including the OMT probes with a 180° hybrid to send the combined signal to the filterbank. The inset shows the mm-wave feedline, the capacitively coupled $\lambda/2$ filter, and the KID inductor. **b:** *Left:* The layout of microwave microstrip resonators in order to measure dielectric properties. *Middle:* Measurements of SiN dielectric and *Right:* amorphous silicon.

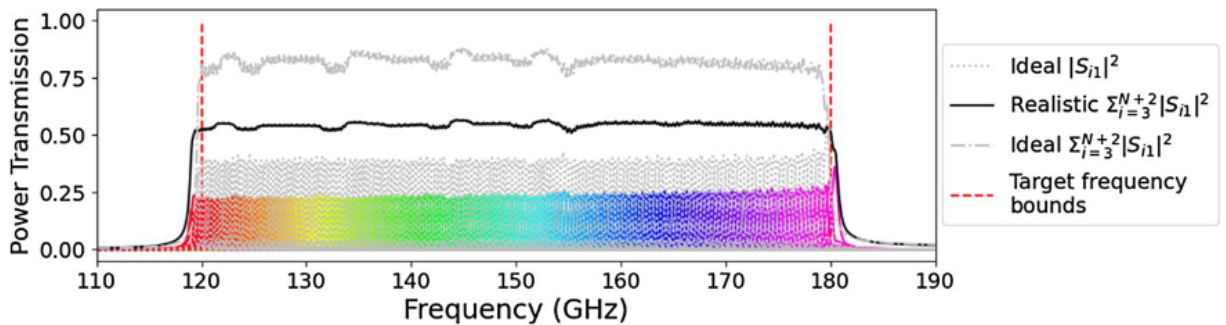


Figure 4.3: Two python model simulations of an SPT-SLIM filter bank between 120–180 GHz showing both the single and total power transmission. Each channel is oversampled by a factor of 1.6. The colored lines show the approximate actual device characteristics when fabrication errors and dielectric loss is included. The gray lines are the theoretical transmissions with no errors or losses. [54]

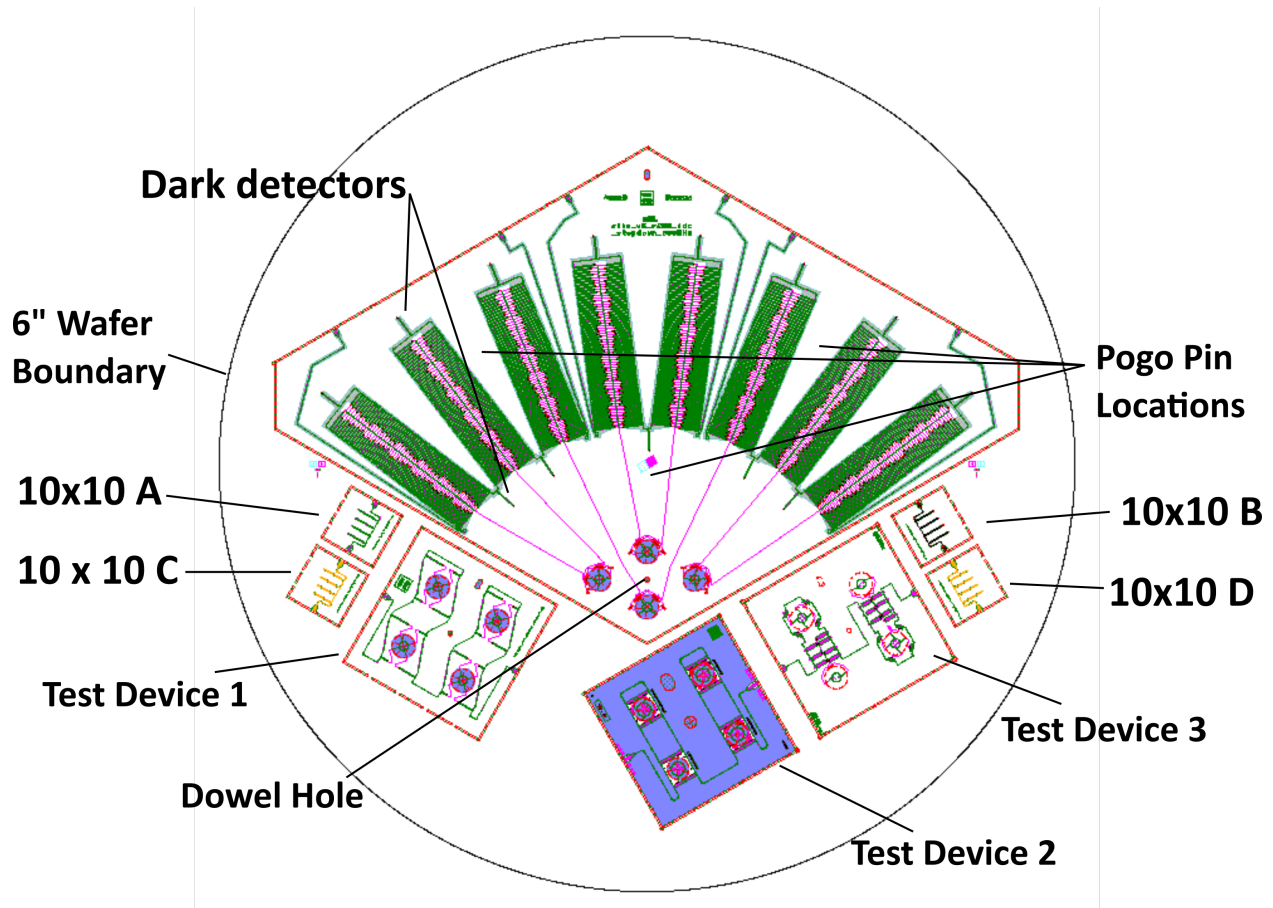


Figure 4.4: A diagram of the full SPT-SLIM submodule design on a six inch silicon wafer with various test devices. Spring-loaded pogo pins located between some of the resonator banks secure the wafer inside the detector box to prevent vibrations. Two dowel hole pins are made to ensure the wafer stays aligned with the horn inside the detector box. The test devices allow for quick checks of the viability of a submodule as well as other diagnostic structures. [5]

4.3 Fabrication

Fabrication of the on-chip spectrometer utilizes a 6-layer design. The substrate is a high-resistivity silicon wafer that has a silicon oxide and low-stress silicon nitride coatings (step 1 in 4.5). Four layers are added on top of the wafer which consist of aluminum, niobium, silicon nitride, and another niobium layer.

Fabrication begins with an aluminum deposition in an ultra-high vacuum (UHV) sputtering chamber at a rate of 6nm/min (step 2). The aluminum layer is 30nm thick and the thickness is verified with a profilometer after the next etch. The aluminum is then spin coated with AZ1512 photoresist at 4500rpm and exposed using Maskless Laser Aligning (MLA) lithography. The photoresist is developed in AZ1:1 and then undergoes a brief oxygen plasma descum. Next, the aluminum is etched using Al Etch A, a mixture of phosphoric, acetic, and nitric acids, until all exposed aluminum is removed (step 3). The photoresist is then removed using an NMP sonicated bath at 80C for 20 minutes. Now the niobium device layer is deposited using the same UHV sputter tool to a thickness of 200nm at 5nm/min (step 4). The aluminum layer undergoes an ion mill to remove the top few nanometer thick oxide layer just before the niobium is deposited. This process ensures that galvanic contact is made between the two metals. The niobium then undergoes the same lithography process as the aluminum except AZ 300 MIF is used as the developer to improve developing resolution. The niobium is then etched using a flouride plasma machine that uses CHF_3 and CF_4 as the etchants (step 5). The photoresist is then removed using a combination of a 240 second long oxygen plasma ashing at 70C and an overnight bath in NMP at 80C. 300nm of silicon nitride is deposited next using a high-density plasma chemical vapor deposition tool (step 6). Immediately following the silicon nitride deposition, the wafer is placed in the UHV sputtering chamber and another 250nm of niobium ground plane is deposited on top of the silicon nitride (step 7). The niobium ground plane is then etched in the exact same process as for the device layer (step 8). Then the silicon nitride layer is patterned using AZ1512 photoresist and exposed with the MLA. The developer using is also AZ 300 MIF.

Afterwards, the silicon nitride is etched using the fluoride plasma tool with CHF_3 and O_2 as the etchants (step 9). The photoresist is then removed using the same process as for the niobium layers. Now with the top layers finished, the device needs to have the backside of the antennas etched out and for the entire device to be diced from the wafer. This is accomplished using a Deep Reactive Ion Etch (DRIE) into the silicon using the silicon oxide layer as an etch stop (step 10). The silicon oxide etch stop is removed using a hydrofluoric acid etch to leave behind a membrane of low-stress silicon nitride that the antenna sits on top of (step 11). These last two steps also are used to dice the wafer by leaving a thin silicon nitride layer that can easily be broken to remove the device.

There are three variations in capacitor design that were tested during fabrication. These are parallel plate capacitors (PPC), interdigitated capacitors (IDC) on silicon nitride and interdigitated capacitors on crystal silicon. The PPCs and IDCs on silicon nitride require no extra processing steps but the IDCs on crystal silicon require two steps to be added at the beginning of fabrication. The two steps are a silicon nitride etch and a silicon oxide step. These two steps are accomplished as before with a fluorine etch for the silicon nitride and a hydrofluoric acid etch for the silicon oxide.

4.4 Testing Setup

The VNA and noise measurements for SPT-SLIM were taken using the same equipment as RAxDEX (see section 3.6). However, SPT-SLIM also includes optical measurements. For optical measurements, we use a combination of a Fourier transform spectrometer (FTS) and a ROACH FPGA board along with a DAC/ADC board developed for the MUSIC instrument. The ROACH is a multitone system capable of generating many simultaneous tones over a 500MHz bandwidth at the same time. For more information on this system, please refer to [46].

SPT-SLIM’s final readout platform will be the ICE signal processing platform [1] that is built upon a general-purpose Xilinx Kintex-7 FPGA motherboard (the ”IceBoard”). This

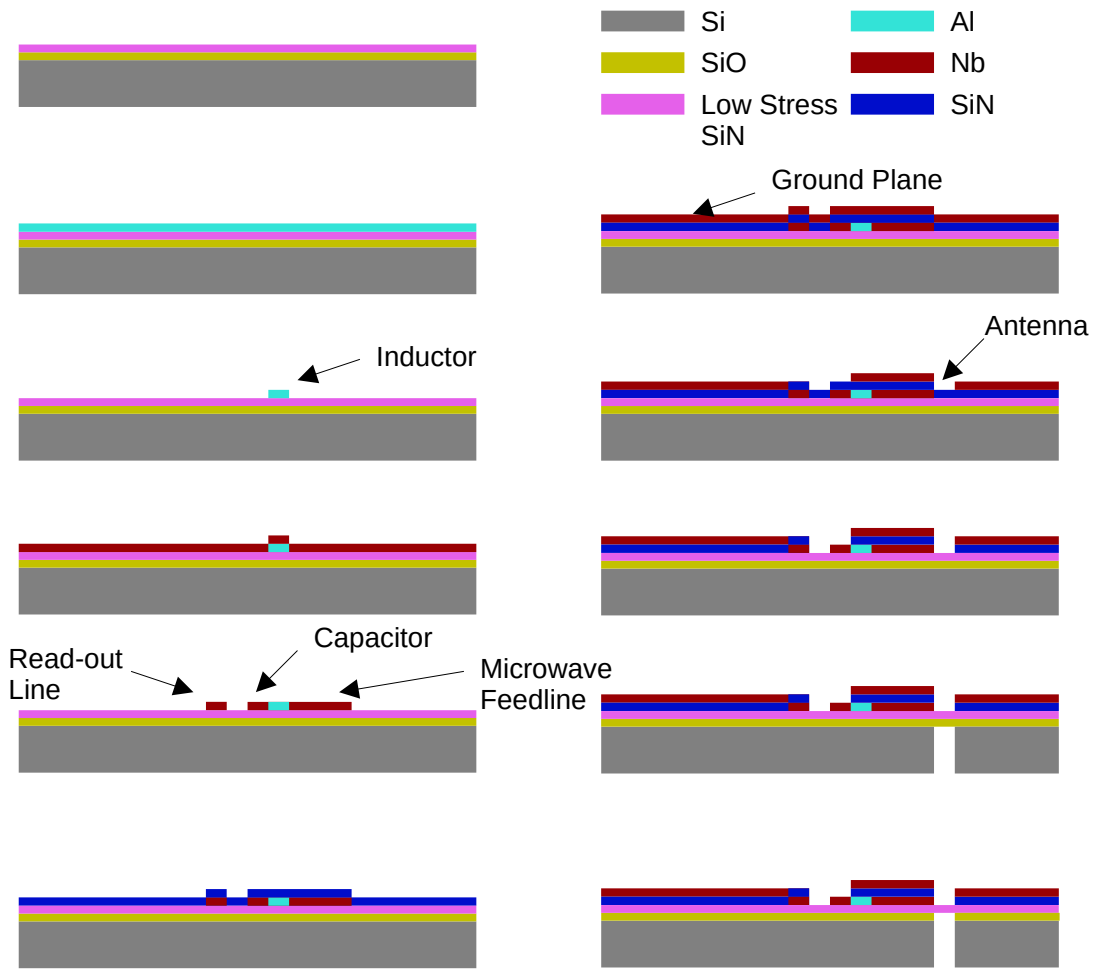


Figure 4.5: A diagram of the fabrication steps for a SPT-SLIM submodule device. The steps shown are the initial six inch wafer with SiO and low stress SiN, the aluminum deposition, the aluminum etch, the niobium deposition, the niobium etch, the SiN deposition, a second Nb deposition, a second Nb etch, a SiN etch, a Si etch, and a SiO etch. The upper Nb layer is the ground plane while the lower Nb layer is the device layer. The OMT sits only on the low stress SiN membrane so that light can be reflected via a backshort.

Device List		
Device Name	Description	Fabrication Notes
spt_slim_multi_1	4in dark fabrication test device	Uneven aluminum deposition
spt_slim_multi_2	4in dark fabrication test device	Difficulties removing resist
spt_slim_mux_2	4in dark test device testing multiplexing	Nb layer deposited before Al
spt_slim_mux_2_2	4in dark test device testing multiplexing	No issues
spt_slim_ripple1_v1	4in dark test without Al	No issues
spt_slim_optfabtest	6in dark fabrication test device	Tried depositing Nb before Al etch
spt_slim_optfabtest_2	6in dark fabrication test device	Reverted to Al etch before Nb deposition
spt_slim_submodule_1	6in dark prototype device	Added PPC test structures
spt_slim_submodule_2	6in dark prototype device	No issues

Table 4.1: A summary of the SPT-SLIM devices fabricated at the University of Chicago.

board connects to smaller modular boards that are designed specifically for each experiment. These modular boards house the analog-to-digital and digital-to-analog converters. The Iceboard is capable of reading out 1024 resonances over a 500MHz bandwidth at a given instance in time.

4.5 Detector Performance and Improvements

4.5.1 Fabrication and Design Improvements

The first complication in detector performance came from a large, approximately sinusoidal ripple along the feedline of the device. The amplitude of the ripple was around 10-20dB in magnitude. Initially, it was thought the issue may come from coupling of the electromagnetic fields on the device to the lid of the detector box. To test this, the amplitude was measured with the lid on, the lid off, and the lid coated in a black absorber (see figure 4.6). The lid itself was having an effect on the detector because the ripple did change throughout each test. Further investigations of this issue in simulations (see figure 4.7) also found that there was likely a parasitic inductance coming from the feedline bridges that caused an impedance mismatch. The bridge width was adjusted from $6\mu\text{m}$ to $18.5\mu\text{m}$. This was able to bring the amplitude of the ripple down by approximately a factor of 2. The remainder of the ripple was caused by a sub-optimal cold amplifier that was replaced with a more suitable amplifier. This brought the ripple amplitude down to a few dB at most.

In the initial 6in wafer design, the parallel plate capacitors were not visible and were likely shorted while the interdigitated capacitors were seen approximately as expected. First, a search for pinhole shorts [41] was done using a scanning electron microscope and the results were likely that there was no pinhole shorts. Pinhole shorts are created when a dielectric deposition avoids specific points on a wafer which creates a hole that a metal deposition would fill to create the short. Next, a new test structure design was created so that a resistance probe measurement could be done at room temperature to determine where the short is occurring. Figure 4.8 shows the test structure design. The primary suspect being tested is shorting at the edge of the capacitor. Test structure B has the top layer extend over the dielectric and test structure A has the top layer smaller than the dielectric. They allow for testing both for pinhole shorts (if A and B are shorted) and for shorts at the edge of the structure (if B is shorted but not A). These test structures were made in both aluminum and

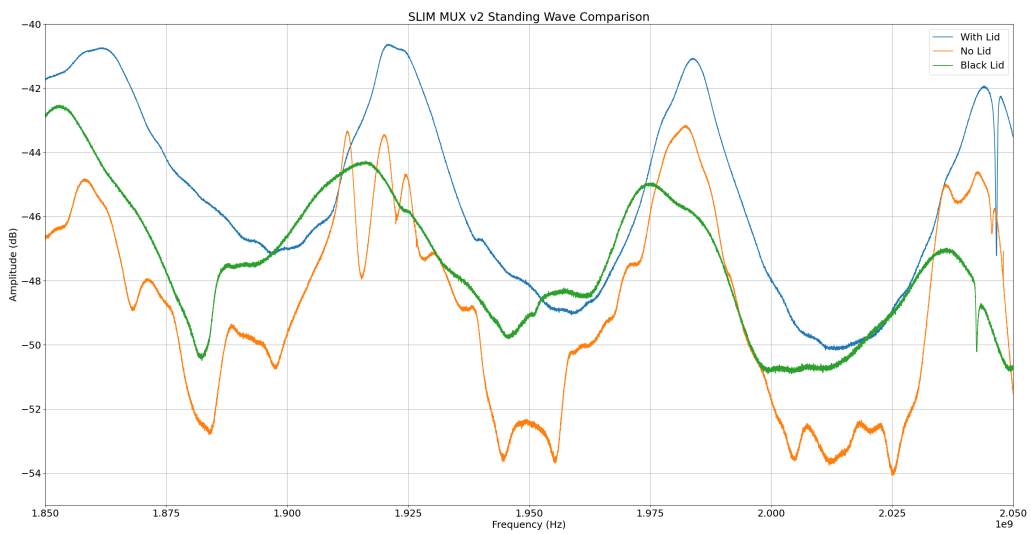


Figure 4.6: Measurements of S21 transmission over a few hundred MHz for the spt_slim_mux_2 device. The three measurements shown are with the detector box lid on, the box lid off, and the box lid coated in a black, light-absorbing material. Removing the lid did little to change the overall amplitude of the standing wave, but blackening the lid did reduce the standing wave. This implied the standing wave could be partially due to the capacitors coupling to the lid of the detector box.

Simulated feedline throughput for Ripple1 large device parasitics with original and optimal bridge parasitic capacitances

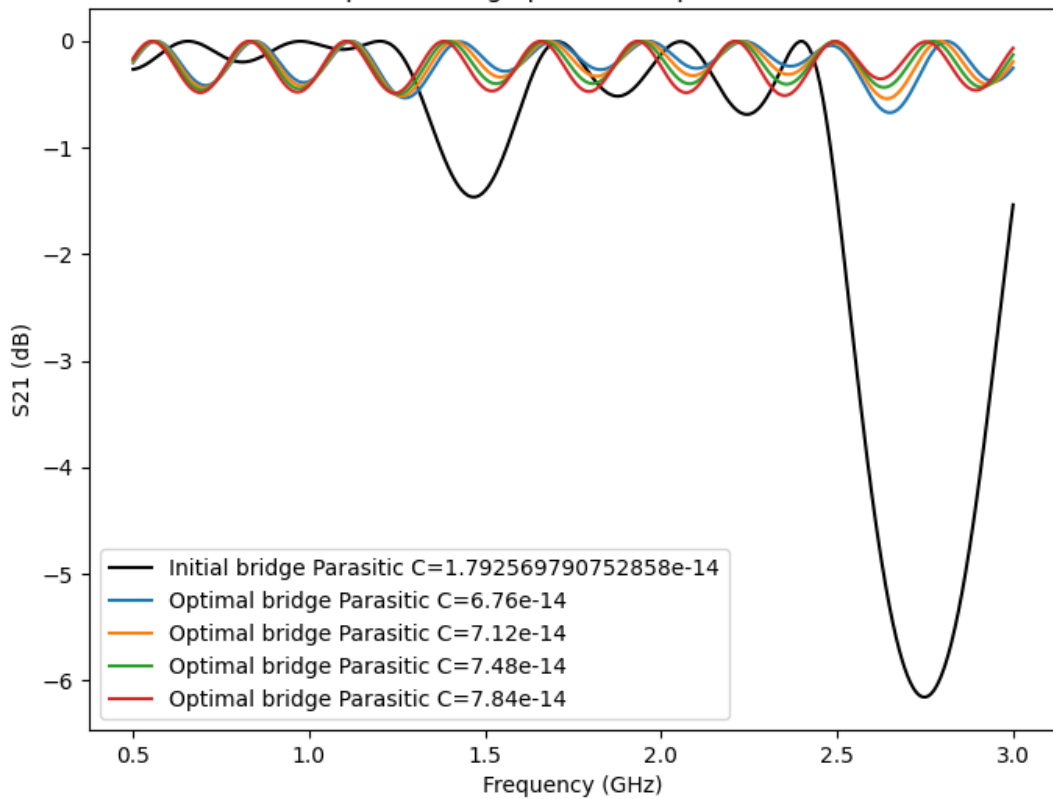


Figure 4.7: A simulated S21 transmission comparing the initial ground-plane bridge width and an optimal bridge width. *Credit: Gethin Robson*

niobium. Upon testing with a DC probe, a short was detected in test structure B but not test structure A providing evidence that the dielectric layer was not fully covering the first niobium layer (see figure 4.8). The solution to this problem was to increase the dielectric thickness from 300nm to 500nm. This was enough of a change to fully coat the sidewalls of the first niobium layer and the PPCs no longer came back shorted.

4.5.2 Anomalies in the Feedline

During initial optical testing of the submodule design using the 6in wafer fabrication process, spikes appeared in the S21 and timestamp measurements as shown in figure 4.9. The spikes were isolated in frequency of the S21 measurements between 2.2GHz and 2.3GHz. The spike only increase the S21 baseline and do not decrease the baseline. The spikes varied in time such that they appeared at different frequencies in sequential S21 sweeps. Changing the warm amplifiers, input power, and microwave cables all had no effect on the spikes. Initially, it was thought the anomaly could be due to an outside wireless source but the entire cryostat and electronics were shielded with aluminum foil and the spikes were unaffected. However, it was discovered that turning the pulse tube cooler (PTC) on the cryostat off greatly reduced or removed the spikes. The PTC produces noticeable vibrations that can be seen in noise measurements. This implies the spikes are due to a component that handles the signal vibrating excessively. Since the wafer is adequately clamped and this issue only appeared using the optical box and not other devices, the spikes were likely due to a box component vibrating. The primary candidate was the SMA connectors that are soldered to launcher boards. The solder or connector may have been damaged in transport of the box and so the connectors were replaced and resoldered. This fully removed the spikes and resolved the issue.



Test Structure A

- Top Layer Niobium
- Silicon Nitride Dielectric
- Bottom Layer Niobium



Test Structure B

Figure 4.8: A diagram of the parallel plate capacitor test structure. In this test structure, the orientation of the capacitors is flipped relative to the detector design in order to expose the separated niobium pads. In test structure A, the top layer niobium does not extend over the dielectric whereas the opposite is true for test structure B.⁵⁴

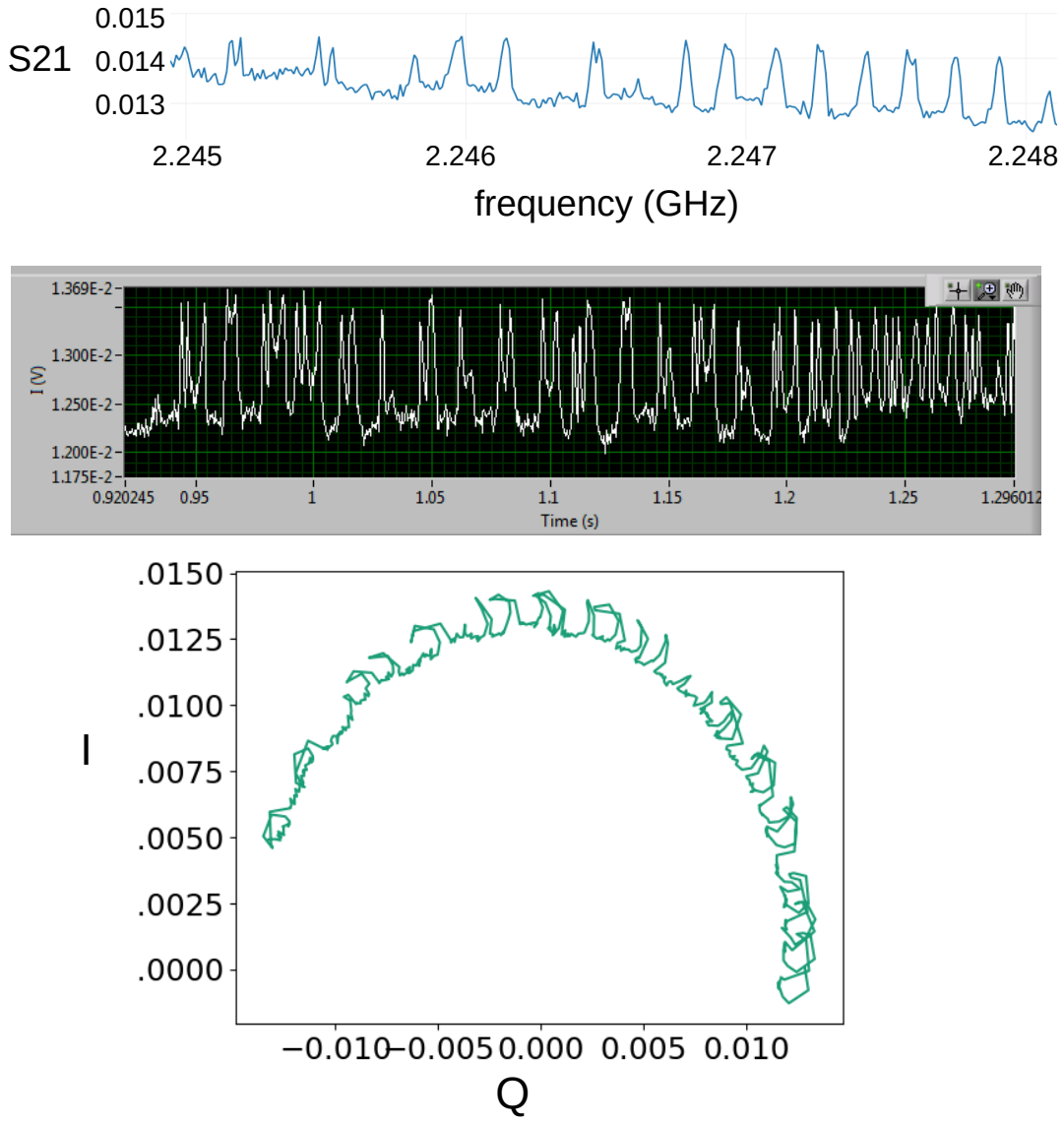


Figure 4.9: *Top*: A measurement of S21 vs frequency for the initial optical testing of the submodule. The baseline should be approximately horizontal with no variations in this frequency regime. The spikes can easily be seen including both some regularity and irregularity in their frequency position. *Middle*: A timestream of the in-phase component at a specific frequency in the region where the spikes appear. A Fourier transform of this component reveals that there is not a specific frequency that the spike appear at. *Bottom*: The in-phase and quadrature components during a sweep in frequency. The spikes are seen here as curved deviations away from expected circle from the cable delay.

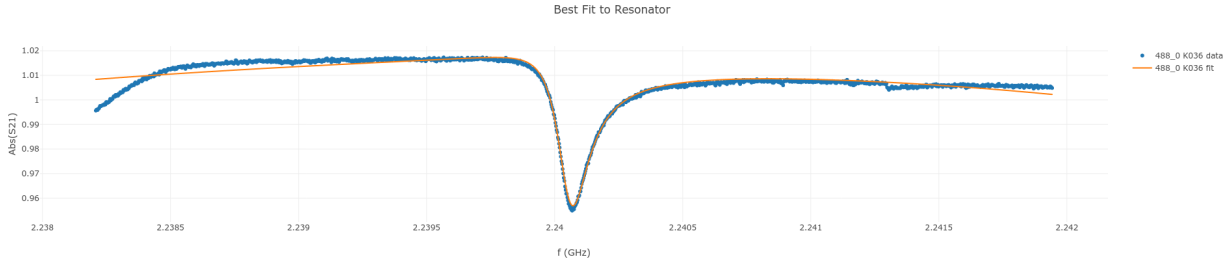


Figure 4.10: An example PPC resonance from `spt_slim_submodule_2`. This resonance had quality factors of $Q \sim 1.6 * 10^4$, $Q_i \sim 2.2 * 10^4$, and $Q_c \sim 1.5 * 10^4$. The resonances were generally more shallow than the IDCs with averages of $Q \sim 2 * 10^4$, $Q_i \sim 3 * 10^4$, and $Q_c \sim 1 * 10^5$. The higher than design Q_c is likely due to not fully characterizing the SiN at the University of Chicago fabrication facility.

4.5.3 Quality Factors

As previously described, a key property of MKID resonances is the quality factor. The quality factor is related to the sensitivity of the detector and the ability to multiplex. For SPT-SLIM, the design Q_c is $5 * 10^4$ with an expectation of the Q_i to be approximately $1 * 10^5$. Figure 4.10 shows an example resonance from `spt_slim_submodule_2` with $Q_c \sim 1.5 * 10^4$ and $Q_i \sim 2.2 * 10^4$. This particular resonance utilized a parallel plate capacitor. The SiN dielectric of the PPCs were not yet fully characterized which caused the large discrepancy between the design and actual quality factors. The Q_c for the IDCs was, in contrast, approximately $1 * 10^5$ while the Q_i was approximately $3 * 10^4$ (see figure 4.13). The Q_i values are believed to be low due to the same contamination of the sputtering chamber used to deposit the Nb and Al layers as the RAxDE project.

However, earlier in the fabrication timeline, the sputtering chamber had significantly less contamination. For example, the `slim_mux_2` device had a very consistent $Q_i \sim 1.5 * 10^5$ as seen in figure 4.11. This device had 142 measured resonances. However, a wide scatter can be seen in the Q_c of this device, ranging from 10^4 to 10^6 . This is due to small fabrication defects typically in the inductor. Because the inductor volume is extremely small, any small change in the thickness or widths of the meander will cause a relatively large change in the inductance. Thus both the Q_c and the f_0 values will also have a large scatter.

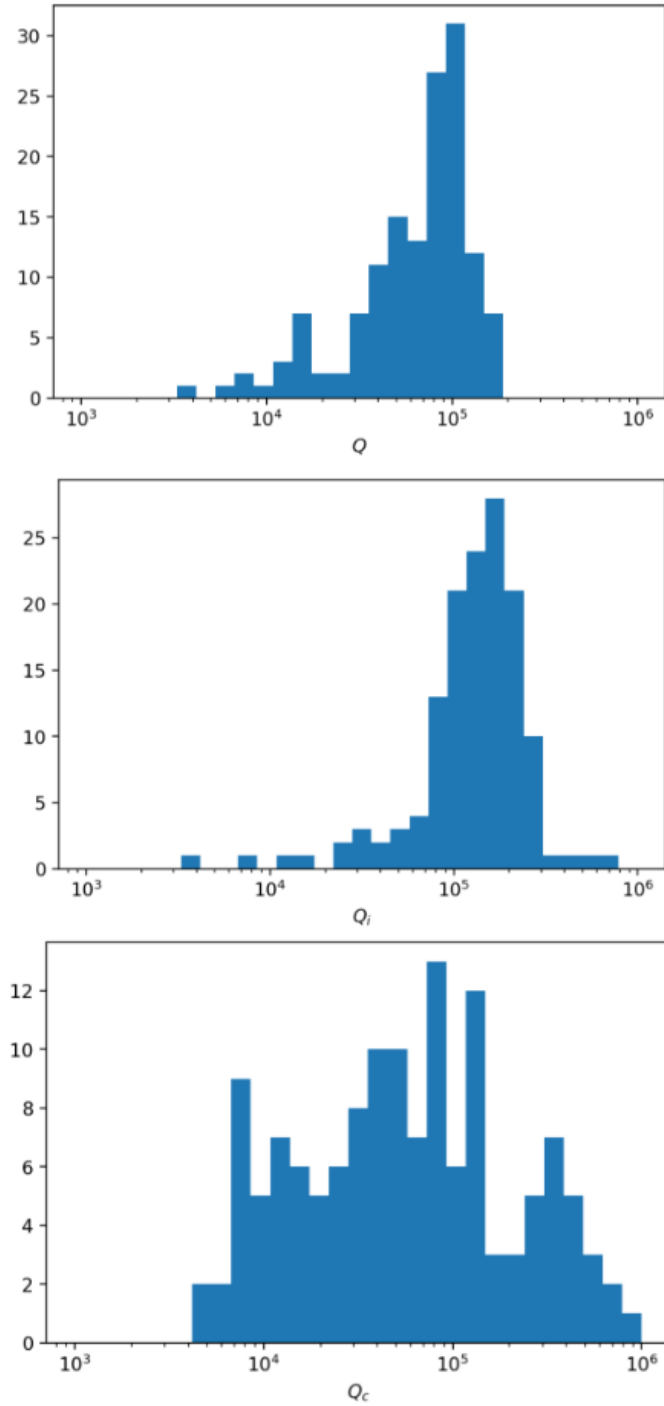


Figure 4.11: The distributions of Q (Top), Q_i (Middle), and Q_c (Bottom) on the multiplexing test device `slim_mux_2`. The Q_i have a localized distribution centered around 1.5×10^5 while the Q_c are much more spread out between 10^4 and 10^6 . Since Q depends on Q_i and Q_c , the distribution is a more spread out version of the Q_i distribution with an average of 7.5×10^4 . There were 142 resonances that were measured on this device.

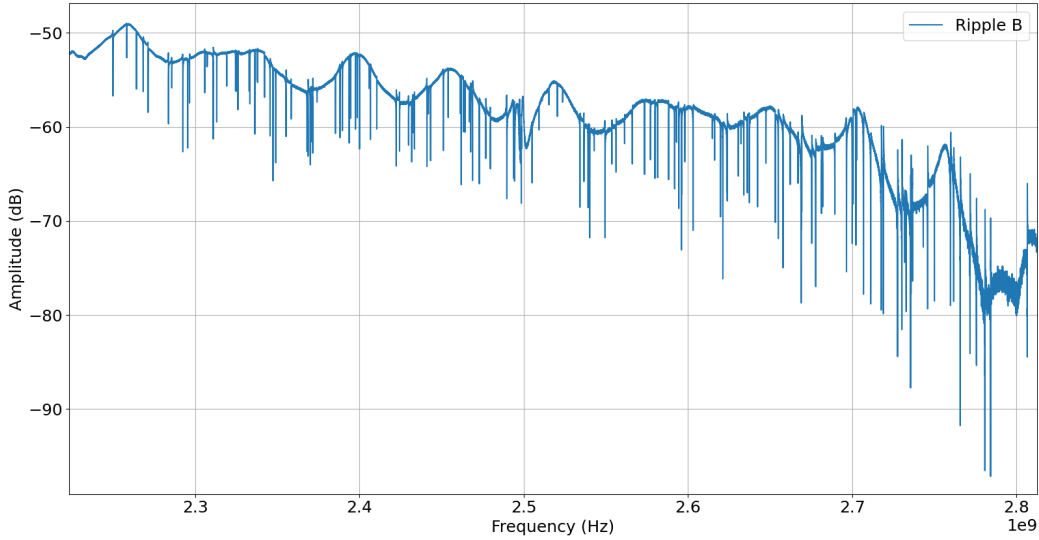


Figure 4.12: A full device VNA sweep from 2.2GHz to 2.8GHz for ripple test device `slim_ripple_v1`. The large baseline variation of 3-5dB can be seen throughout the sweep. There were 155 out of 160 resonances found on this device.

4.5.4 Frequency Placement

In order to have the desired spectral resolution, we need to pack as many KIDs as possible onto the detector wafer. Many of the prototype devices had approximately 150 resonances which is similar to the number of KIDs on one bank on the full submodule devices. Figure 4.12 shows an example of a full device VNA sweep on the `slim_ripple_v1` device. The first main limiting factor to the number of KIDs is the physical size of the silicon wafers. For this reason, the SPT-SLIM submodules utilize 6in silicon wafers instead of the standard 4in silicon wafers. Silicon wafers also are regularly produced in 8in diameter, but the fabrication facilities at both Argonne National Laboratory and the University of Chicago do not support the processing of 8in wafers. Most machines used in these facilities can only operate with 6in wafers and are optimized for 4in wafers. Furthermore, the uniformity of many processes is hard to maintain as the wafer size increases.

Secondly, the multiplexing capability is limited by the resonant frequency placement and, consequently, the quality factor uniformity. Figure 4.13 shows the resonant frequency

of every KID measured on the spt_slim_submodule_2 trio IDC. The resonances are grouped such that there is a small jump in resonant frequency between groups. If two resonances overlap with each other, it becomes much more difficult to extract information from that resonance. We can define that two resonances clash (overlap with each other) if they're within three linewidths of each other. Linewidth is defined as the separation between two resonant frequencies multiplied by the lowest quality factor and divided by the resonant frequency. This is essentially the distance between two resonances scaled for the widths of the resonances. Figure 4.13 shows a histogram of the spt_slim_submodule_2 linewidths. Any linewidth greater than 20 was included in the last bin. Of the 333 resonances, there are approximately 100 clashed resonances. This means that a third of the resonances on this device are unusable.

Figure 4.14 shows the resonant frequencies and linewidths of the duo IDC device that had 218 resonances. As before, any linewidth greater than 20 was included in the last bin. As expected, fewer resonances spaced further apart leads to less clashing. There were approximately 35 clashed resonances on this device which account for 16% of the resonances.

The resonance frequency scatter is a challenging value to bring down. It would require more precise fabrication techniques, particularly in the lithography and etching of the Al inductors. Electron beam lithography was attempted at Argonne National Laboratory, but the scatter was identical implying that the etch consistency may play a greater factor. In addition, modifying the design and sacrificing some of the detectors properties could reduce the scatter. The number of KIDs could be reduced which would sacrifice spectral resolution (such as in the duo IDC) or the inductor volume could be made larger which would sacrifice sensitivity.

4.5.5 *Polarization Measurements*

As stated in section 4.2, the detectors are sensitive to both horizontal and vertical polarizations. Some of the early measurements were to determine how well the detector separated

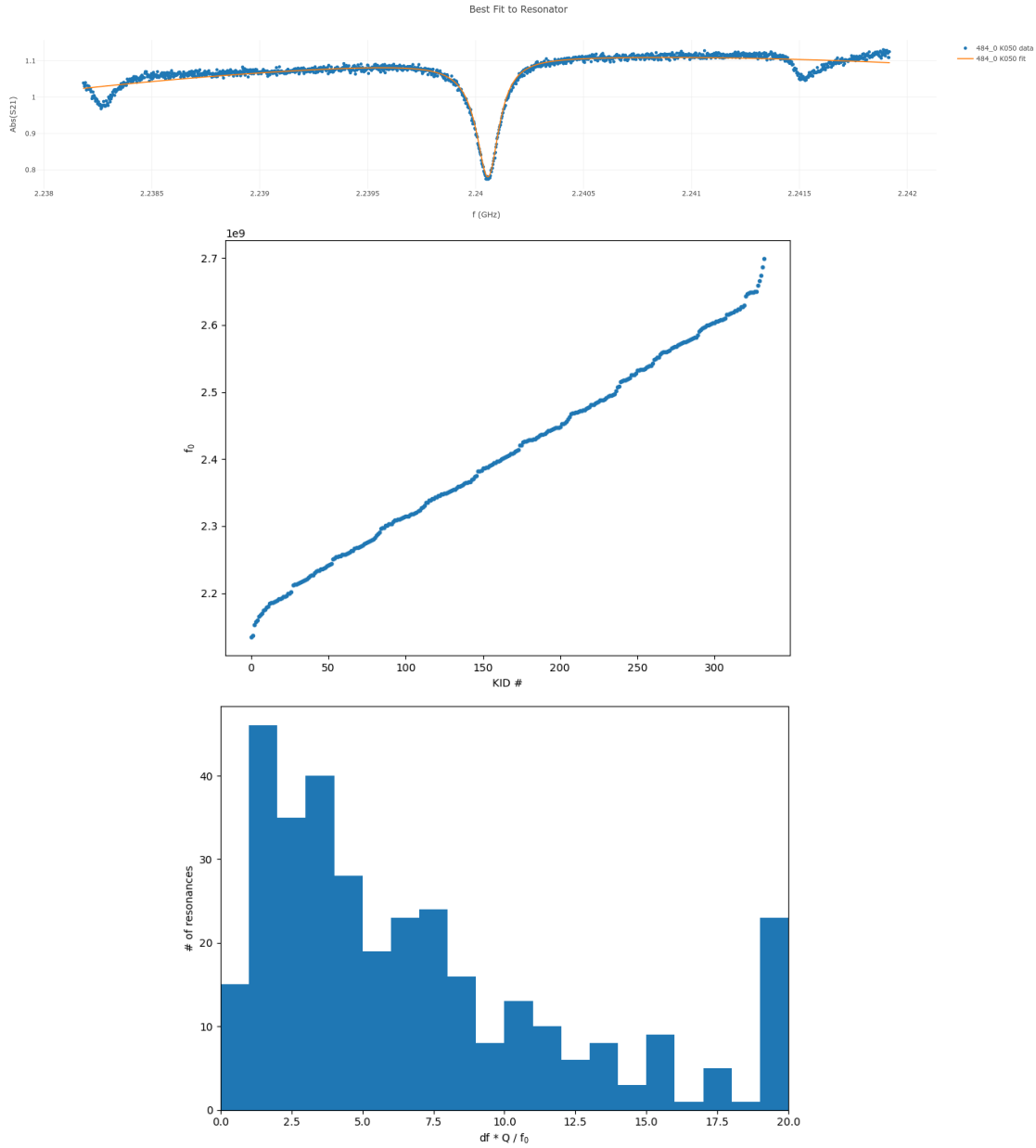


Figure 4.13: *Top*: An example ideal resonance from spt_slim_submodule_2 trio IDC bank. This resonance had quality factors of $Q \sim 1.6 * 10^4$, $Q_i \sim 2.3 * 10^4$, and $Q_c \sim 5.5 * 10^4$. *Middle*: The frequencies of each KID on spt_slim_submodule_2 trio IDC bank. Each bank of resonators begins and ends with a small bump in resonance frequency. The resonance frequencies tend to bunch up at the end of a bank. *Bottom*: A histogram of the resonance frequency spacing scaled by the resonance quality factor. A clash for SPT-SLIM is defined as having a spacing $\frac{Q\delta f}{f_0} < 3$.

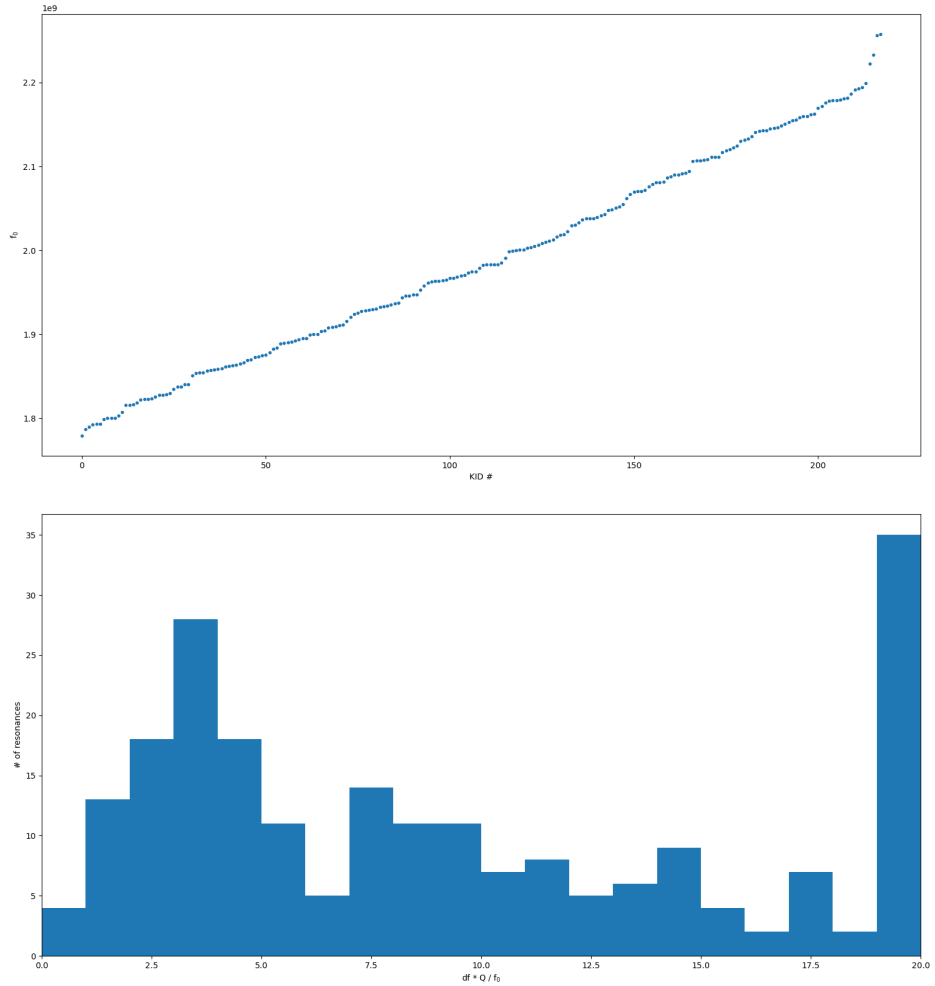


Figure 4.14: *Top*: The frequencies of each KID on spt_slim_submodule_2 duo IDC bank. Each bank of resonators begins and ends with a small bump in resonance frequency. The resonance frequencies tend to bunch up at the end of a bank. *Bottom*: A histogram of the resonance frequency spacing scaled by the resonance quality factor. A clash for SPT-SLIM is defined as having a spacing $\frac{Q\delta f}{f_0} < 3$.

polarizations which, in turn, also measures the amount of unpolarized stray light being picked up by the detectors. The testing setup used a blackbody with a chopper in front of it that periodically stops the signal. The light then passes through a collimating lens, a polarizing wire-mesh grid, and a focusing lens before entering the cryostat window. Eccosorb was used to cover the setup in order to shield the setup from stray light. The optical setup was placed on a moveable cart that was aligned to the detectors by measuring where the detector response to the chopped signal was greatest. Initially, measurements were made with the blackbody at 1000C. Later, measurements were also made at 600C and 300C to ensure the detectors were not oversaturated. Three different devices had their polarizations measured in this way, FT47, FT84, and FT89. These were all fabricated at Argonne National Laboratory. They have approximately 22 resonators (depending on yield) where the first 11 are narrowband and the remaining 11 are broadband. For FT47 and FT84, the wire mesh grid was manually rotated in 30° increments. However, for FT84 and FT89, a motorized wire mesh grid was used to both measure the polarization in the same increments and in a continuously rotating fashion.

The two values that need to be extracted to characterize the polarization are the polarization orientation angle ψ and the cross-polarization response ϵ . To measure these, first the difference between the detector response, $\Delta\frac{\delta f}{f}$, between the chopped signal and the blackbody signal is calculated for each polarization angle θ . The difference in the detector response is directly related to the polarization angle through the following equation:

$$\Delta\frac{\delta f}{f} = A \left(\cos[2(\theta \frac{\pi}{180} + \psi)] + \frac{1 + \epsilon}{1 - \epsilon} \right) \quad (4.1)$$

A least squares fit was performed to produce values for each of A , ψ , and ϵ . There are a few extra steps involved when using the continuous rotation data. First the data has to be truncated to remove the regions before and after the grid started rotating. This is performed by eye and is within a few degrees of the true value. Since the signal rapidly switches between blackbody and chopped, the values of the signal are split and

binned. The signal average is calculated for bins containing 200 data points and then a spline is fit to the average. The points are then divided into the blackbody points if they are above the average and chopped points if they are below the average. Then, the average of each bin of blackbody points and chopped points are calculated. Two splines are then used to interpolate each set of points. The difference between these two splines is then the final $\Delta \frac{\delta f}{f}$ and is fit to extract the polarization parameters.

There are two minor drawbacks that introduce small systematic errors using the continuous rotation method described above. First, there are a small number of data points when the blackbody is partially covered by the chopper that are included in the averages. This will make the averages ever so slightly closer to the center of the blackbody and chopped points (about 0.04% was the average percent difference in a post-analysis calculation). Second, by splitting the blackbody and chopped points using the average, we are assuming there is always a non-zero gap between the signals. In other words, there cannot be zero separation between the two points as would occur if the detectors were perfectly polarized. This situation only applies to a small number of detectors we measured and only minorly raises the cross-polarization response.

FT47 gave a large amount of questionable results for the narrowband detectors as can be seen in figure 4.15. Many appeared to be asymmetric when rotating through the full 360 degrees of polarization. There are two issues we attribute this to. First, the blackbody temperature was at 1050°C which may have oversaturated the detectors as mentioned earlier. Second, there was no correction for the cable delay of the system as described in section 4.5.6. Both of these issues were addressed in the other two device's measurements where a temperature of 600°C was used and the correction was applied. Measurements were taken with and without an internal absorber in the device box. The absorbers decreased the cross-polarization of the broadband detectors but had little effect on the low quality, narrowband detectors.

With the corrections applied and a new device, FT84 showed improved results. Figure

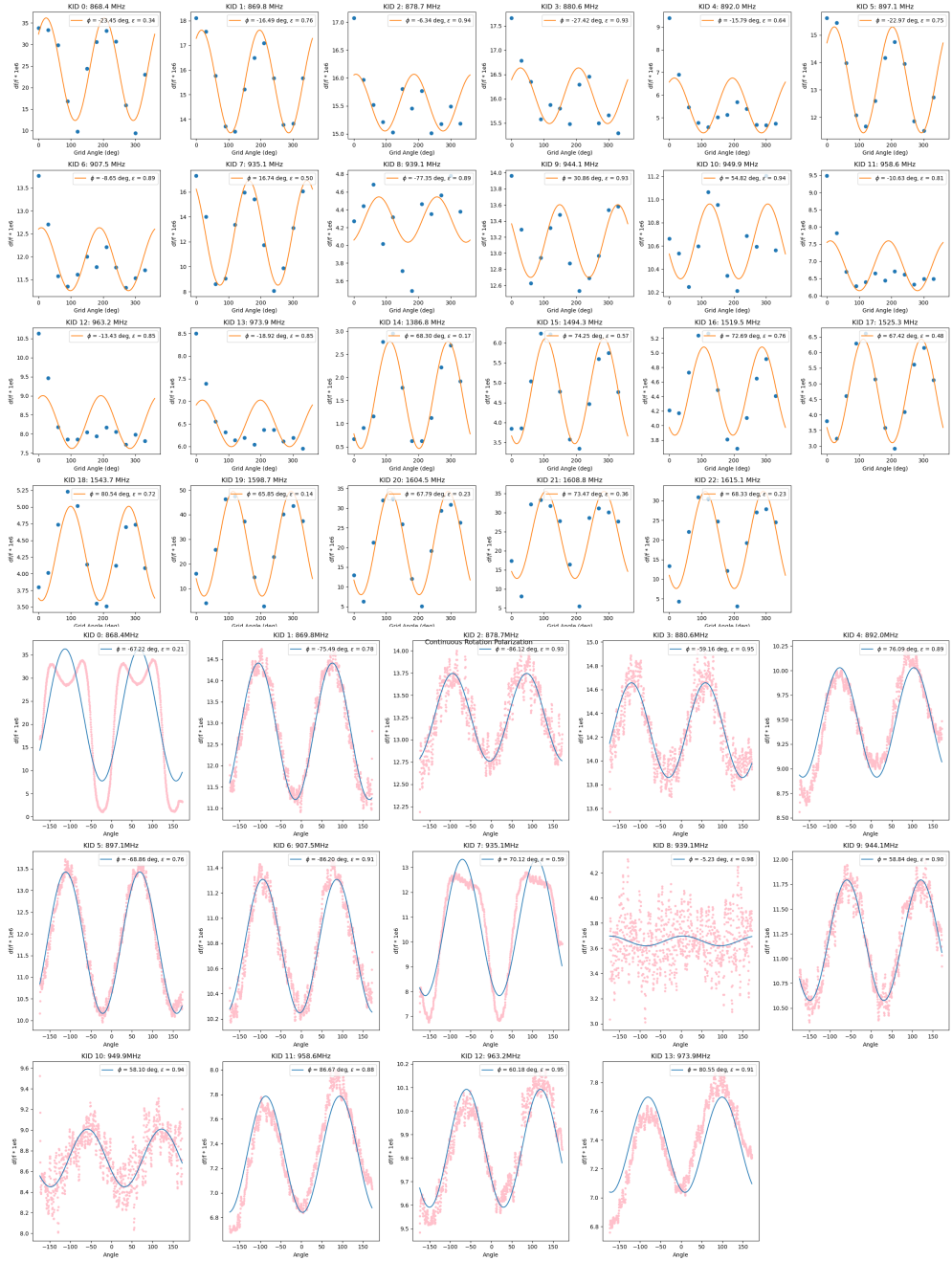


Figure 4.15: Plots showing the separation between the chopped and unchopped signals in terms of df/f for FT47. The first 13 KIDs are narrowband detectors and the remaining KIDs are broadband detectors. Each KID was fitted for polarization angle and cross-polarization. The first set of plots uses specific polarization angles whereas the second set uses a rotating polarizing grid.

4.16 shows the polarization measurements of FT84. The least-squares fit on two of the KIDs did not match the curves well, so manual fits were performed as well by manually adjusting the parameters. The narrowband detectors performed much better with 5 of the 13 having cross-polarizations less than 0.5. KID 6 had a cross-polarization of 0.06. The broadband detectors also performed better with the four KIDs with good results having cross-polarizations less than 0.14.

FT89 showed even greater improvements with all broadband KIDs having a cross-polarization below 0.13 (see figure 4.17). In addition, 9 of the 14 narrowband KIDs had cross-polarizations below 0.5. There were also less KIDs with bad or noisy data implying that the fabrication of the devices has improved. Overall, it appears dark pickup is unlikely to be a problem for either narrowband or broadband detectors, but some attention should be paid to the narrowband detectors to ensure their cross-polarizations continue to drop and are consistent.

4.5.6 *Detector Noise*

The noise spectrum were acquired for a subset of the devices fabricated. One such device was spt_slim_submodule_2. The noise data was taken using the same method as the one described in section 3.6. Figure 4.18 shows the noise spectrums of two KIDs taken at 30mK. Both on and off resonance spectrums are plotted. KID 66 was had quality factors of $Q \sim 2.6 * 10^4$, $Q_i \sim 3.5 * 10^4$, and $Q_c \sim 1.0 * 10^5$ while KID 87 had $Q \sim 1.5 * 10^4$, $Q_i \sim 2.6 * 10^4$, and $Q_c \sim 3.4 * 10^4$. Since KID 66 has a higher quality factor, the noise levels are around a factor of 10 lower. The $1/f$ noise falls off above 50Hz.

4.5.7 *Spectral Response*

An important aspect of characterizing the detectors is to determine what wavelengths of light each individual detector is sensitive to. The simulated detector response for the entire band between 120GHz and 180GHz is shown in figure 4.3. This simulation includes all 200 detectors for a single polarization.

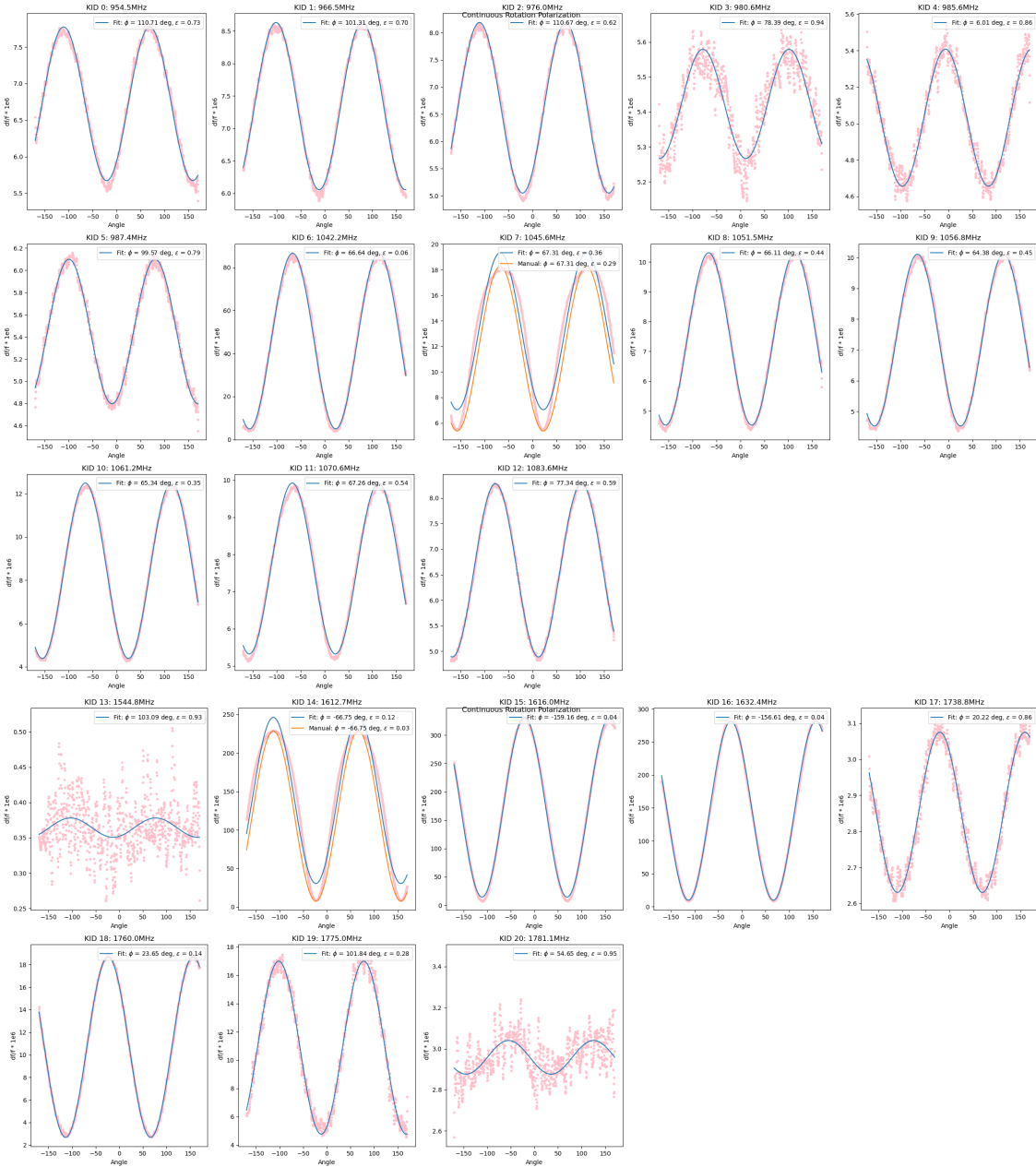


Figure 4.16: Plots showing the separation between the chopped and unchopped signals in terms of df/f for FT84. The first 13 KIDs are narrowband detectors and the remaining KIDs are broadband detectors. Each KID was fitted for polarization angle and cross-polarization. 2 KIDs were also manually fitted because least-squares fitting produced too high of cross-polarization.

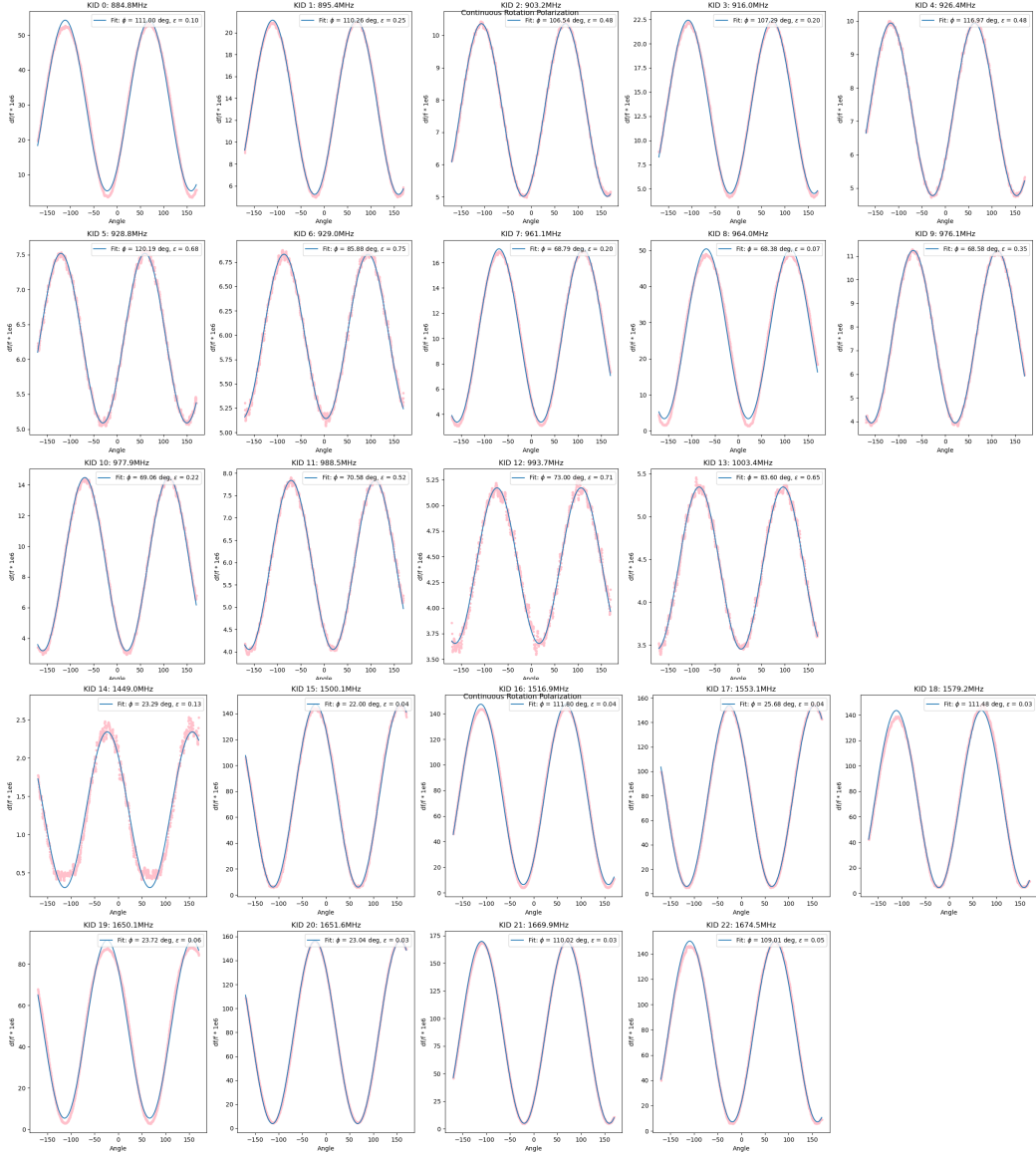


Figure 4.17: Plots showing the separation between the chopped and unchopped signals in terms of df/f for FT89. The first 13 KIDs are narrowband detectors and the remaining KIDs are broadband detectors. Each KID was fitted for polarization angle and cross-polarization.

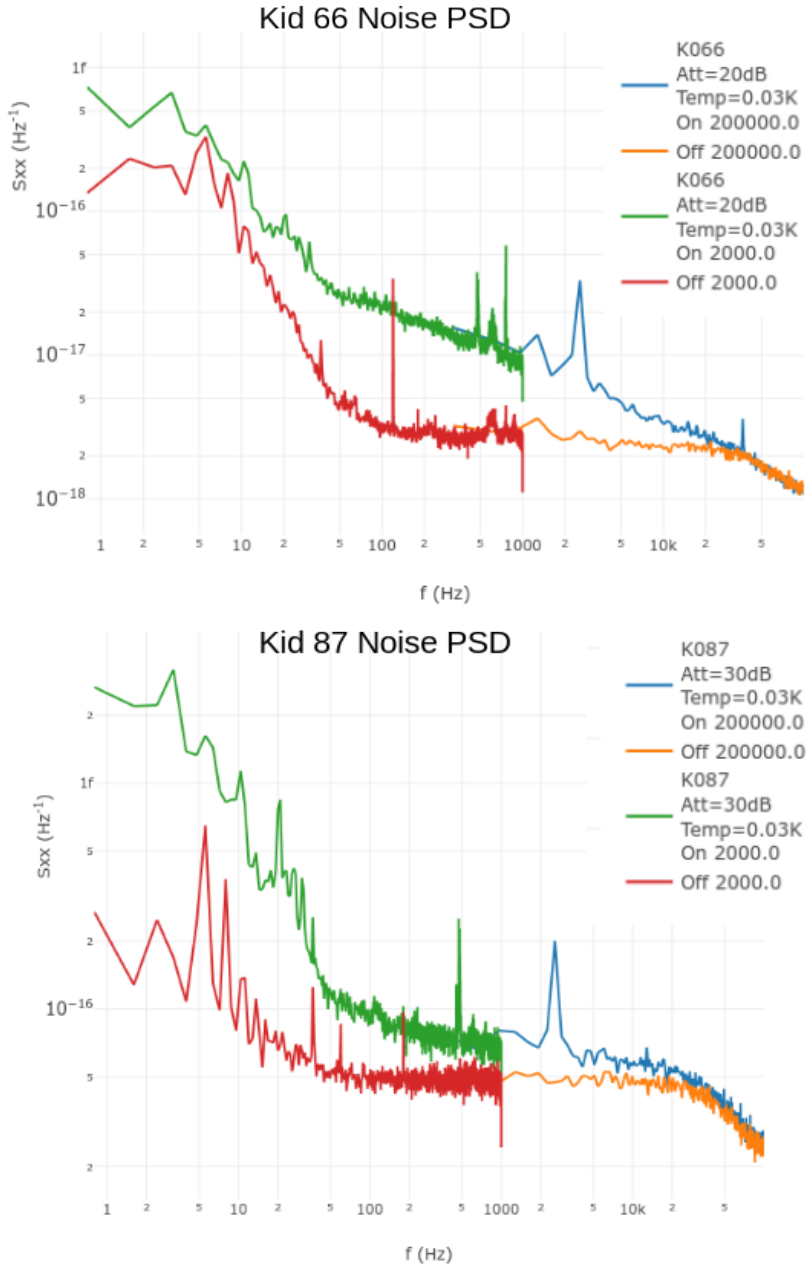


Figure 4.18: Noise power spectrums taken on and off resonance from KID 66 and KID 87 from spt_slim_submodule_2 IDC duo bank taken at 30mK. KID 66 had a quality factor approximately twice as large as KID 87 which explains the difference in absolute noise levels. Both resonances feature $1/f$ noise to a frequency of 50Hz.

The spectral response is measured using the FTS and Roach board described in 4.4. First, the optimal power to each KID is determined by starting at a low input power and raising the power until just before bifurcation of the resonance. Then, the exact tone to measure each KID is determined by where the change in distance in the IQ plane is greatest. Finally, the FTS mirror is swept three times back and forth and the deviation of the resonance is measured. Near the white light fringe of the FTS, the KID response oscillates and then decays. The decay rate is related to the bandwidth and responsivity of the detector. After appropriate corrections are made to the data as for noise calculations, then the Fourier transform is taken to convert the data to frequency space.

Early SPT-SLIM devices performed relatively poorly. FT84 had only three spectral KIDs that showed somewhat desirable performance (see figure 4.19 for a subset of the spectral responses). The broadband KIDs also performed poorly with many peaks and a low overall response.

It was later found that the dielectric properties of the Argonne National Laboratory silicon nitride were not accurate. This caused the millimeter waveguide cutoff to block the first harmonic of the signal. However, for some of the spectral channels, other harmonics were able to travel down the waveguide providing a small response. This was recognized and corrected after my contributions to the collaboration had ended. Figure 4.20 shows some of the KIDs from these newer devices that have desirable spectral response. These measurements were taken using the Iceboard readout systems.

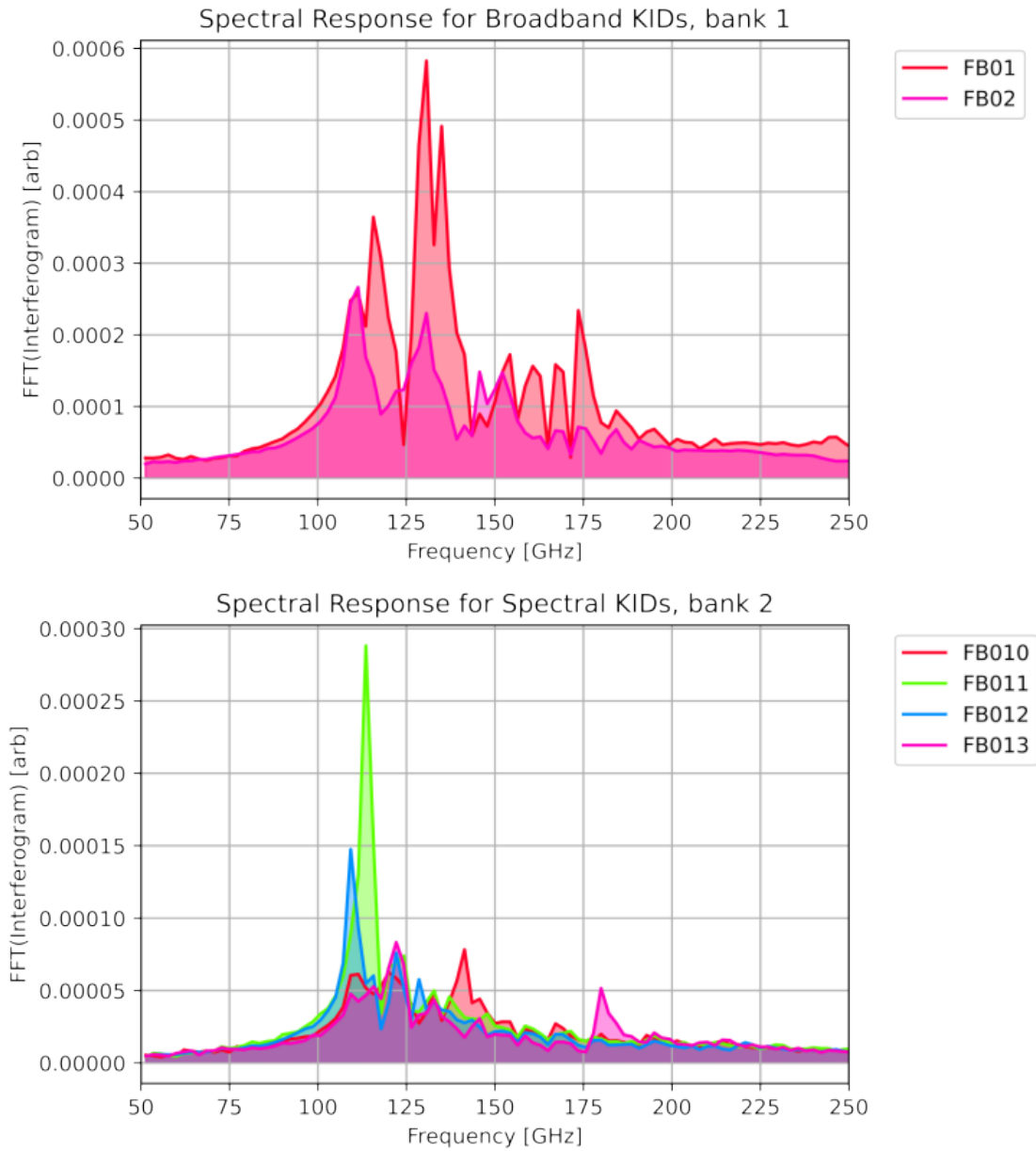


Figure 4.19: The spectral response for 2 broadband KIDs (*Top*) and 5 narrowband KIDs (*Bottom*) on device ft84. The broadband responses show no broad peaks but instead show a number of smaller peaks, indicating that the detector is not functioning correctly. The narrowband responses show two peaks from FB011 and FB012 with FB011 significantly stronger. This indicates some issue either in fabrication or with the testing setup that is able to produce the appropriate response occasionally.

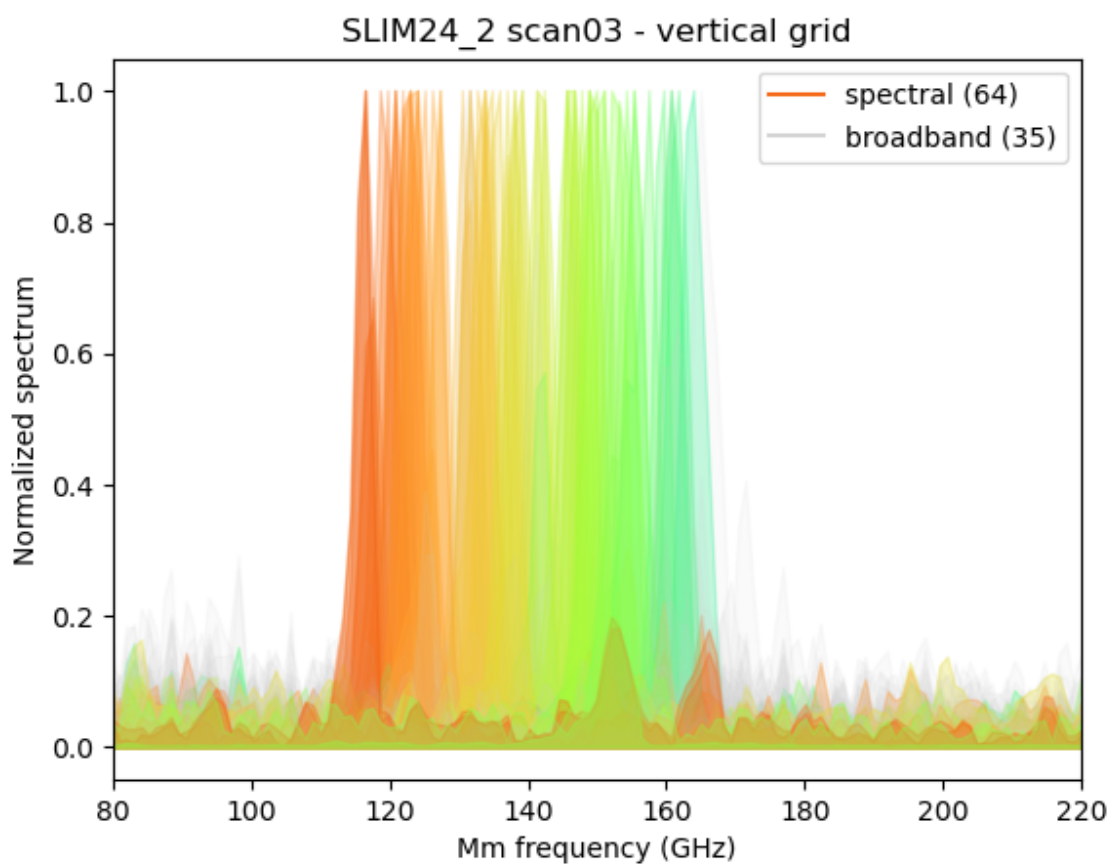


Figure 4.20: The spectral response for 64 spectral channels and 35 broadband channels on submodule_24 fabricated and measured by other members of the SPT-SLIM collaboration.

CHAPTER 5

FORESCASTING OF SPT-SLIM CONSTRAINTS ON THE

LUMINOSITY FUNCTION

5.1 Line Intensity Mapping Measurements

As mentioned previously, line intensity mapping (LIM) is a recently implemented method to measure large-scale structure without needing to resolve individual galaxies. Previous LIM experiments such as COMAP[14], COPPS[38], and CONCERTO[38] have just begun to scratch the surface of what is possible with LIM. For more information on LIM experiments, see [39]. COMAP, for example, in their early science release put a constraint on the CO power spectrum of $P_{CO}(k) = -2.7 \pm 1.7 * 10^4 \mu\text{K}^2 \text{ Mpc}^3$ from $2.4 < z < 3.4$. In 4, I described that SPT-SLIM is specifically targeting CO rotational lines in order to measure the CO power spectrum in a redshift range from $0.5 < z < 2$. models, luminosity function, what would results tell us

5.2 Formalism

Line intensity mapping power spectrums have a clustering and a shot noise component[39] such that

$$P_k(z) = \langle T(z) \rangle^2 b^2(z) P_m(k, z) + P_{shot}(z) \quad (5.1)$$

where $\langle I(z) \rangle$ is the average intensity, $b(z)$ is the redshift-dependent halo bias, $P_m(k, z)$ is the matter power spectrum, and $P_{shot}(z)$ is the shot noise power spectrum. Furthermore, $\langle I(z) \rangle$ and $P_{shot}(z)$ can be further defined as the first and second moments of the line luminosity function $\Phi(L, z) \equiv dn(z)/dL$

$$\langle T(z) \rangle \propto \int_0^\infty L \Phi(L, z) dL \quad (5.2)$$

$$P_{shot}(z) \propto \int_0^\infty L^2 \Phi(L, z) dL \quad (5.3)$$

An example of the CO power spectrum is shown in figure 5.1. From the figure, one can

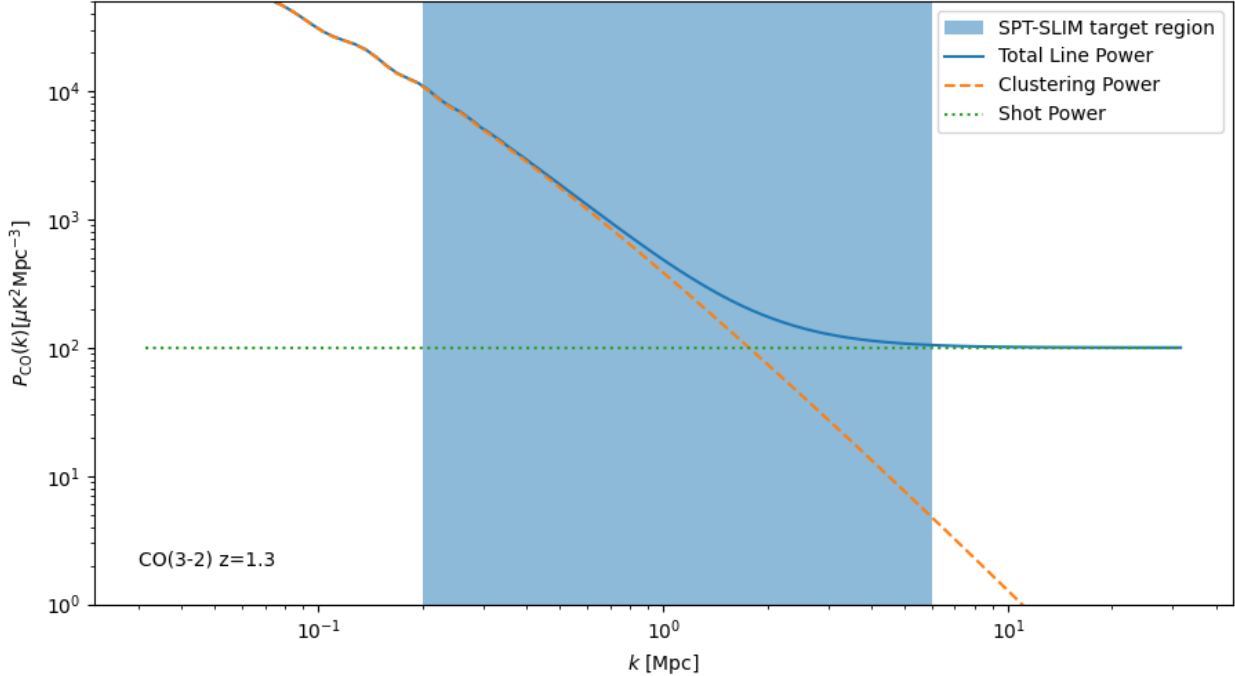


Figure 5.1: An example CO(3-2) power spectrum at a redshift of 1.3. The parameters used to generate the power spectrum are the same as is mentioned in section 5.4. Also shown are the two components of the power spectrum, the clustering and shot power. The blue shaded region are the target wavenumbers that SPT-SLIM will constrain.

deduce that the ability to constrain the clustering and shot components is based on the scale factors, k , that an experiment can measure.

The CO power spectrum can be written in the parameters of the Schechter luminosity function[55] in order to provide more astrophysical constraints. The luminosity function represents the number density of CO luminous galaxies such that

$$\Phi(L)dL = \phi_* \left(\frac{L}{L_*} \right)^\alpha e^{-L/L_*} dL/L_* \quad (5.4)$$

where ϕ_* is a normalization factor, L_* is a high-luminosity cutoff, and α is the low-luminosity power law index.

5.2.1 The Cluster-Power Component

We can, to first order, write the mean brightness temperature of a CO rotation line as

$$\langle T(z) \rangle = \frac{1}{8\pi} \frac{(c/\nu)^3}{2k_B H(z)} \epsilon_{CO} \quad (5.5)$$

where $H(z)$ is the Hubble parameter at a given redshift and ϵ_{CO} is the volume emissivity of the CO line. The Schechter function can then be used to write the volume emmissivity as

$$\epsilon_{CO} = \phi_* L_* \Gamma(\alpha + 2, L_{min}/L_*) \quad (5.6)$$

where L_{min} is a low luminosity cutoff and Γ is the incomplete gamma function. [53] use this same method to cross-correlate CO emission with other LSS tracers in order to measure the emission in terms of redshift and scale.

5.2.2 The Shot-Power Component

Similar to the cluster-power component, the shot power, P_{shot} can be written using 5.3 such that

$$P_{shot}(z) = \left(\frac{c^3(1+z)^2}{8\pi\nu^3 k_B H(z)} \right)^2 \int_0^\infty L^2 \Phi(L, z) dL \quad (5.7)$$

The second moment of the luminosity function is defined to be equal to the volume emissivity variance ϵ^2 which can be written using the Schechter parameters as

$$\epsilon^2 = \phi_* L_*^2 \Gamma(\alpha + 3, L_{min}/L_*) \quad (5.8)$$

5.2.3 Direct Detections

Equations 5.6 and 5.8 both have three parameters while the CO power spectrum has only two components to measure. Thus, we are under constrained and need to add in another component to break the degeneracy. The most straightforward candidate is direct detections of individual galaxies in the survey volume. A relatively small number of very luminous

galaxies that can be seen at high redshift is all that is needed to put a constraint on the upper end of the luminosity function.

5.3 Likelihood Method

We can use the equations described in section 5.2 to begin to predict the constraints that SPT-SLIM will be able to put on the CO power spectrum and the luminosity function. For this analysis, we generate points on the power spectrum using some of the expected Gaussian error components and we assume two approximate data points for direct detections with Poisson error. Using this generated data, we perform a Bayesian likelihood analysis to create likelihood contours for each parameter in the power spectrum and in the luminosity function.

5.3.1 Power Spectrum

For the power spectrum, we group the mean brightness temperature and the halo bias together into one parameter P_{clust} such that equation 5.1 becomes

$$P_k(z) = P_{clust}(z)P_m(k, z) + P_{shot}(z) \quad (5.9)$$

This equation has the same format as a linear regression where the x component is $P_m(k, z)$. The log-likelihood for the power spectrum with Gaussian errors is then

$$\ln(\mathcal{L}_G) = \Sigma \left[(-\ln(2\pi\sigma^2))/2 \right] - \frac{1}{2} \Sigma \left[(P_{obs} - P_{mod})^2 / \sigma^2 \right] \quad (5.10)$$

where P_{obs} are the observed data points, P_{mod} are the predicted power spectrum data points for a given set of P_{clust} and P_{shot} , and σ is the error on the observed data points.

Parameter	Value
H_0	$67.5 \text{ [km/sMpc}^{-1}\text{]}$
$\Omega_b h^2$	0.022
$\Omega_{cdm} h^2$	0.122
n_s	0.965
k_{max}	$30 \text{ [Mpc}^{-1}\text{]}$

Table 5.1: Cosmological parameters used to generate the matter power spectrum.

5.3.2 Luminosity Function

For the luminosity function, we combine all of equations 5.1, 5.4, 5.5, 5.6, 5.7, and 5.8. We also need to provide a prescription for the halo bias in this method. For this analysis, we use a constant value of $b = 2$ from Appendix B of [13] that approximately matches the regime SPT-SLIM will be in.

The log-likelihood for the luminosity function parameters is the summation of the Gaussian log-likelihood of the power spectrum data points and the Poissonian log-likelihood of the direct detection data points. The Poissonian log-likelihood is given by

$$\ln(\mathcal{L}_P) = \sum [y_{obs} \ln(y_{mod}) - y_{mod} - \ln(|\Gamma(y_{obs} + 1)|)] \quad (5.11)$$

where y_{obs} are the number of observed galaxies of a given luminosity and y_{mod} are the model predictions of the number of galaxies of a given luminosity.

5.4 Data Generation

Initially, a cosmology has to be assumed so that we can generate a matter power spectrum. We use the CAMB Python package [40] with the cosmological parameters shown in table 5.4. Furthermore, we make the following assumptions in table 5.4 about the telescope observations and the true values of parameters.

Parameter	Value
ϕ	$0.2 [Mpc^{-3}dex^{-1}]$
L_*	$3.233 * 10^{-13} [10^{10}L_\odot]$
α	-1.3
ν	$345.8 [GHz]$
b	2
$\delta\nu$	2
B (bandwidth)	$60 [GHz]$
Field Length	1°
White Noise Level	$100 [\mu K/\sqrt{s}]$
d (diameter of dish)	$10 [m]$
$\delta\nu$	$0.7538 [GHz]$
$\log(k_{min})$	-1.2 $[\log(Mpc^{-1})]$
$\log(k_{max})$	0.7 $[\log(Mpc^{-1})]$
z	1.3

Table 5.2: Telescope and observational parameters used in data and error generation.

For the initial analysis, however, data and error generation was simplified. For the power spectrum only (no luminosity function parameters), the power spectrum data and errors were taken the 200 hour projections in Figure 4 from the SPT-SLIM overview [36]. The analysis with the power spectrum used the same errors but assumed the true values of the power spectrum parameters in table 5.4. The direct detection points were generated with the same true values as the power spectrum, but the errors are Poissonian based upon the value of the data point. A total of 5 power spectrum data points and 2 direct detection data points are generated, which reflects the approximate data points SPT-SLIM will create. These data points, along with the error and true value lines, can be seen in the upper two images of the right column of figure 5.3.

5.5 Preliminary Results

The power spectrum only analysis is essentially a linear fit using Gaussian errors. Figure 5.2 shows both the χ^2 contours for the clustering and shot power components and the marginalized χ^2 for each parameter. The most likely values and their errors are $\langle T_{CO} \rangle^2 b^2 = 1.26 \pm 0.25 \mu\text{K}^2 \text{Mpc}^{-3}$ and $P_{shot} = 81.16 \pm 0.10 \mu\text{K}^2 \text{Mpc}^{-3}$.

To obtain results for the luminosity parameter analysis, we first begin by calculating the maximum likelihood by finding the minimum of the negative log likelihood. These parameter values are then used to plot the best fit curves in the upper two images of the right column of figure 5.3. Then, to obtain marginalized likelihoods, the likelihood functions are sampled in a grid around the true values. A bilinear interpolation is used to create the color plots in figure 5.3. Those grids are then used to generate the likelihood curves for the individual parameters by performing an integration along one axis using the composite Simpson's rule. In order to avoid numerical errors, the LogSumExp function is used to perform the summation in Simpson's rule.

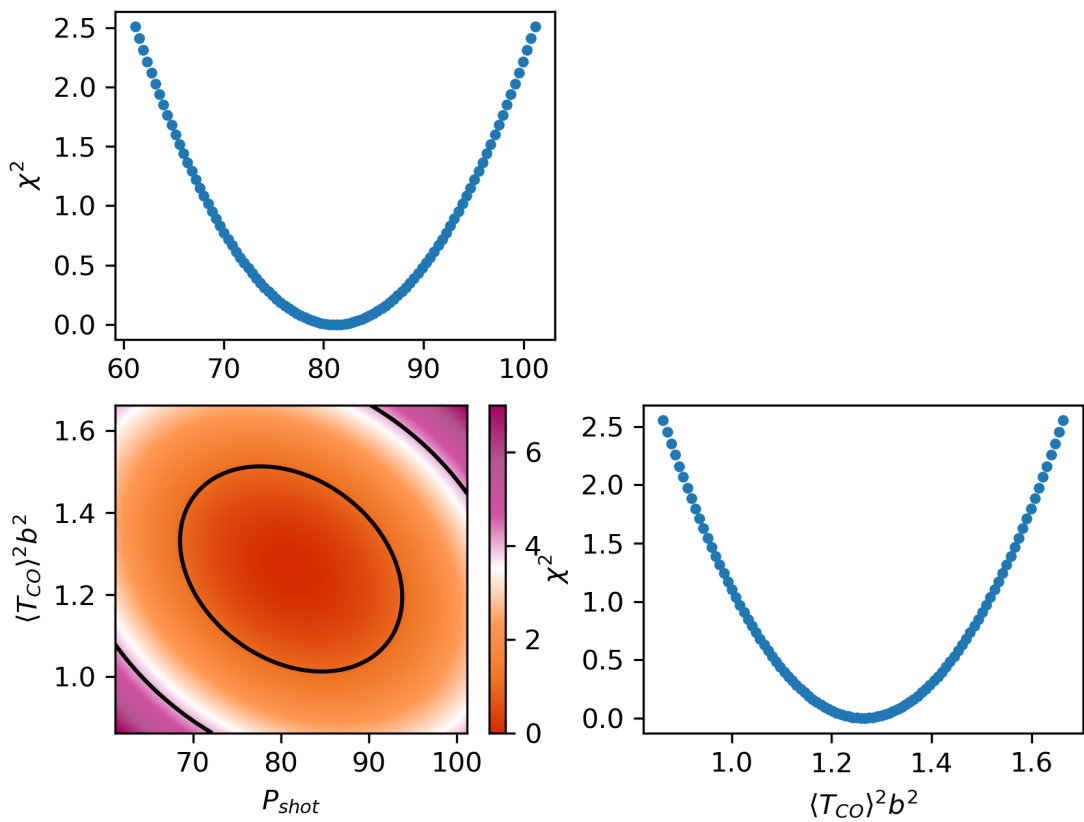


Figure 5.2: The parameter contour and marginalized χ^2 for the power spectrum only analysis. The curves represent Gaussians because the equation is linear with respect to the two parameters. 1 and 4 σ contours are plotted in black on the lower left image.

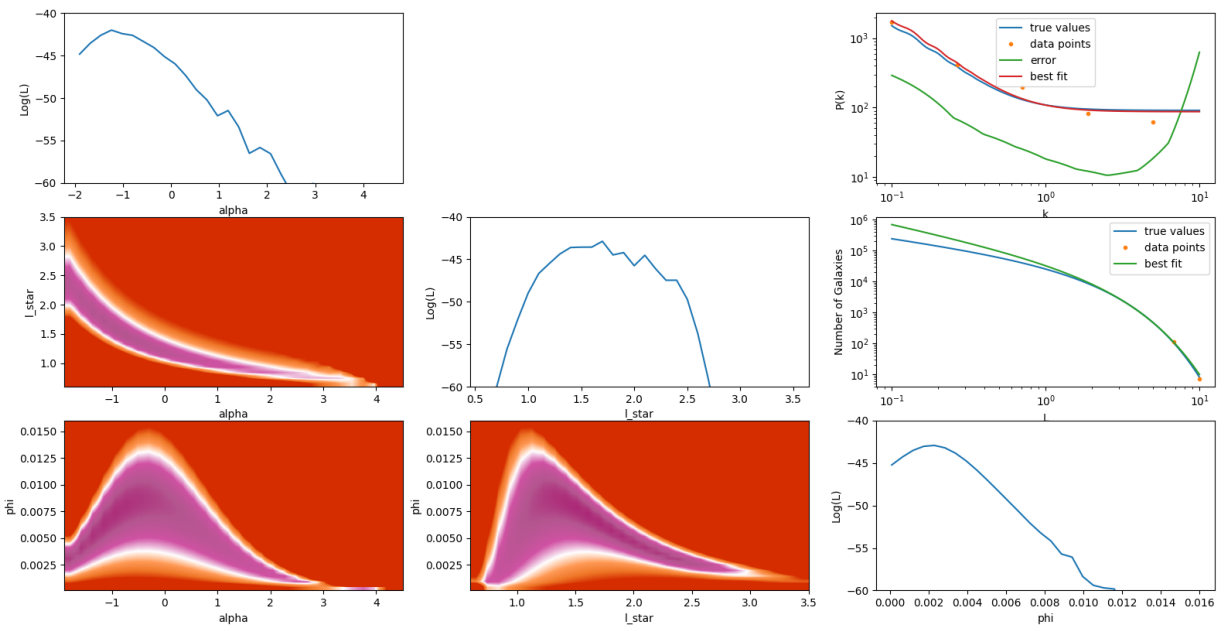


Figure 5.3: Marginalized log likelihoods of the three parameters of the luminosity function. The top two images of the right column show the data points, the true power spectrum and luminosity function curves, and the curves corresponding to the maximal likelihood.

CHAPTER 6

CONCLUSION

MKIDs have been under rapid development since they were conceived in the early 2000s. They are being used for a wide variety of experiments including dark matter detection and other uses outside of astronomy. This thesis expanded upon the development of MKIDs particularly in regards to terahertz spectroscopy with RAxDEx and millimeter wave spectroscopy with SPT-SLIM.

RAxDEx demonstrated the first successful waveguide built into a silicon wafer. This also required investigating and simulating methods to couple light from a waveguide onto a KID. We successfully simulated an inductor design that acts as a terahertz absorber. In simulations, it absorbed at least 60% of the power delivered down the waveguide. Furthermore, we also fabricated and tested aluminum-niobium MKIDs. We then demonstrated that the MKIDs and waveguide could coexist in close proximity on the wafer. Initial tests show good evidence that the KID design is feasible and reasonably matches simulations, but more work is needed to resolve some issues with quality factors. The two main steps that need to be taken are ensuring there is no contamination of the metallic films by preconditioning the sputter chamber further and to look into the simulations to identify the cause of the coupling quality factor dichotomy. Furthermore, future work is needed to design and fabricate a horn to couple light into the waveguide in order to use a Fourier transform spectrometer to measure the spectral response of the detectors to light. The horn would need to attach to the side of the wafer. The difficulties of this lie in ensuring the horn makes good contact with the wafer and aligning the horn to the very small waveguide. Alignment could potentially be done with alignment pins coming out of the side of the box if the tolerances are adequate. We will also investigate the addition of a backshort to the detector by switching to a silicon-on-insulator wafer and etching the Si behind the absorber, using the SiO_2 as an etch stop. Similar structures have been created before. For example, we have made a parallel plate capacitor KID device where the dielectric was a thin crystal silicon membrane. This addition is necessary to prevent the loss of light into the silicon and improve the absorption effectiveness of the inductor.

Line Intensity Mapping promises to produce a new way of measuring large scale cosmological structure at intermediate redshifts. A few preliminary experiments are being conducted and SPT-SLIM is a pathfinder experiment to demonstrate the feasibility of future LIM experiments. SPT-SLIM is pushing the boundaries of mm-wave spectroscopy by using on-chip MKID spectrometers. This design is extremely space efficient and has a simpler read-out scheme than many other detectors. In this thesis, we covered much of the early work in designing, testing, and fabricating MKIDs for SPT-SLIM. The initial KID designs had many issues including the waveguide cutoff being incorrectly positioned which caused the spectral response to be extremely limited. In addition, much development was done creating and tuning fabrication processes. Some examples are transitioning processes to effectively use 6 inch silicon wafer, investigating parallel plate capacitors as an alternative to interdigitated capacitors, and attempting to reduce resonant frequency scatter. Testing of the MKIDs also uncovered a variety of issues that were eventually resolved including a large standing wave on the feedline and time-dependent spikes in the detector read-out. This work enabled the current generation of SPT-SLIM detectors that demonstrate deployable performance as seen in figure 4.20.

Finally, we laid the foundation for using SPT-SLIM's power spectrum data points to place constraints on both the power spectrum parameters and on the CO luminosity function. This analysis relies on Bayesian statistics to combine both Gaussian and Poissonian data to create likelihood contours for each parameter. This analysis will be improved by incorporating more of the telescope and observational parameters outlined in table 5.4. Some work has already been done to this end, but was not completed by the time of this thesis. Furthermore, more analysis could be done for different redshifts and CO rotational lines. These are parameters easily changed in the analysis functions. Finally, this project could be extended by starting with map generation and then creating the data points on the power spectrum from the generated map.

REFERENCES

- [1] K. Bandura, A. N. Bender, J. F. Cliche, T. de Haan, M. A. Dobbs, A. J. Gilbert, S. Griffin, G. Hsyu, D. Ittah, J. Mena Parra, J. Montgomery, T. Pinsonneault-Marotte, S. Siegel, G. Smecher, Q. Y. Tang, K. Vanderlinde, and N. Whitehorn. Ice: A scalable, low-cost fpga-based telescope signal processing and networking system. *Journal of Astronomical Instrumentation*, 05(04):1641005, 2016.
- [2] J. Bardeen, L. N. Cooper, and J. R. Schrieffer. Theory of superconductivity. *Phys. Rev.*, 108:1175–1204, Dec 1957.
- [3] R. Barends. Photon-detecting superconducting resonators. *TUDelft*, Jun 2009.
- [4] P. Barry. On the development of superspec: A fully integrated on-chip spectrometer for far-infrared astronomy. 2014.
- [5] P. S. Barry, A. Anderson, B. Benson, J. E. Carlstrom, T. Cecil, C. Chang, M. Dobbs, M. Hollister, K. S. Karkare, G. K. Keating, D. Marrone, J. McMahon, J. Montgomery, Z. Pan, G. Robson, M. Rouble, E. Shirokoff, and G. Smecher. Design of the spt-slim focal plane: A spectroscopic imaging array for the south pole telescope. *Journal of Low Temperature Physics*, 209(5):879–888, Dec 2022.
- [6] Jochem Baselmans. Kinetic inductance detectors. *Journal of Low Temperature Physics*, 167(3):292–304, May 2012.
- [7] José Luis Bernal and Ely D. Kovetz. Line-intensity mapping: theory review with a focus on star-formation lines. *A&A Rev.*, 30(1):5, December 2022.
- [8] Thomas L. R. Brien, Peter A. R. Ade, Peter S. Barry, Edgar Castillo-Domínguez, Daniel Ferrusca, Thomas Giscard, Victor Gómez, Peter C. Hargrave, Amber L. Hornsby, David Hughes, Enzo Pascale, Josie D. A. Parrianen, Abel Perez, Sam Rowe, Carole Tucker, Salvador Ventura González, and Simon M. Doyle. MUSCAT: the Mexico-UK Sub-Millimetre Camera for AsTronomy. In Jonas Zmuidzinas and Jian-Rong Gao, editors, *Millimeter, Submillimeter, and Far-Infrared Detectors and Instrumentation for Astronomy IX*, volume 10708, page 107080M. International Society for Optics and Photonics, SPIE, 2018.
- [9] Giuseppe Cataldo, Emily M. Barrentine, Berhanu T. Bulcha, Negar Ehsan, Larry A. Hess, Omid Noroozian, Thomas R. Stevenson, Edward J. Wollack, Samuel H. Moseley, and Eric R. Switzer. Second-generation micro-spec: A compact spectrometer for far-infrared and submillimeter space missions. *Acta Astronautica*, 162:155–159, 2019.

- [10] Jhy-Jiun Chang and D. J. Scalapino. Kinetic-equation approach to nonequilibrium superconductivity. *Phys. Rev. B*, 15:2651–2670, Mar 1977.
- [11] George Che, Sean Bryan, Matthew Underhill, Philip Mauskopf, Christopher Groppi, Glenn Jones, Bradley Johnson, Heather McCarrick, Daniel Flanigan, and Peter Day. WSPEC: A Waveguide Filter Bank Spectrometer. *arXiv e-prints*, page arXiv:1503.06528, March 2015.
- [12] Xiaomeng Cheng, Rui Huang, Jimmy Xu, and Xiangdong Xu. Broadband terahertz near-perfect absorbers. *ACS Applied Materials & Interfaces*, 12(29):33352–33360, 2020. PMID: 32526137.
- [13] Dongwoo T. Chung, Patrick C. Breysse, Kieran A. Cleary, Håvard T. Ihle, Hamsa Padmanabhan, Marta B. Silva, J. Richard Bond, Jowita Borowska, Morgan Catha, Sarah E. Church, Delaney A. Dunne, Hans Kristian Eriksen, Marie Kristine Foss, Todd Gaier, Joshua Ott Gundersen, Stuart E. Harper, Andrew I. Harris, Brandon Hensley, Richard Hobbs, Laura C. Keating, Junhan Kim, James W. Lamb, Charles R. Lawrence, Jonas Gahr Sturtzel Lunde, Norman Murray, Timothy J. Pearson, Liju Philip, Maren Rasmussen, Anthony C. S. Readhead, Thomas J. Rennie, Nils-Ole Stutzer, Bade D. Uzgil, Marco P. Viero, Duncan J. Watts, Risa H. Wechsler, Ingunn Kathrine Wehus, David P. Woody, and (COMAP Collaboration). Comap early science. v. constraints and forecasts at $z = 3$. *The Astrophysical Journal*, 933(2):186, jul 2022.
- [14] Kieran A. Cleary, Jowita Borowska, Patrick C. Breysse, Morgan Catha, Dongwoo T. Chung, Sarah E. Church, Clive Dickinson, Hans Kristian Eriksen, Marie Kristine Foss, Joshua Ott Gundersen, Stuart E. Harper, Andrew I. Harris, Richard Hobbs, Håvard T. Ihle, Junhan Kim, Jonathon Kocz, James W. Lamb, Jonas G. S. Lunde, Hamsa Padmanabhan, Timothy J. Pearson, Liju Philip, Travis W. Powell, Maren Rasmussen, Anthony C. S. Readhead, Thomas J. Rennie, Marta B. Silva, Nils-Ole Stutzer, Bade D. Uzgil, Duncan J. Watts, Ingunn Kathrine Wehus, David P. Woody, Lilian Basoalto, J. Richard Bond, Delaney A. Dunne, Todd Gaier, Brandon Hensley, Laura C. Keating, Charles R. Lawrence, Norman Murray, Roberta Paladini, Rodrigo Reeves, Marco P. Viero, and Risa H. Wechsler. Comap early science. i. overview. *The Astrophysical Journal*, 933(2):182, July 2022.
- [15] P. E. Clegg and et al. The ISO Long-Wavelength Spectrometer. *A&A*, 315:L38–L42, November 1996.

- [16] Leon N. Cooper. Bound electron pairs in a degenerate fermi gas. *Phys. Rev.*, 104:1189–1190, Nov 1956.
- [17] Peter K. Day, Henry G. LeDuc, Benjamin A. Mazin, Anastasios Vayonakis, and Jonas Zmuidzinas. A broadband superconducting detector suitable for use in large arrays. *Nature*, 425(6960):817–821, Oct 2003.
- [18] Steven A. H. de Rooij, Jochem J. A. Baselmans, Vignesh Murugesan, David J. Thoen, and Pieter J. de Visser. Strong reduction of quasiparticle fluctuations in a superconductor due to decoupling of the quasiparticle number and lifetime. *Phys. Rev. B*, 104:L180506, Nov 2021.
- [19] P. J. De Visser. Quasiparticle dynamics in aluminum superconducting microwave resonators. *TUDelft*, Mar 2014.
- [20] P. J. de Visser, J. J. A. Baselmans, P. Diener, S. J. C. Yates, A. Endo, and T. M. Klapwijk. Generation-recombination noise: The fundamental sensitivity limit for kinetic inductance detectors. *Journal of Low Temperature Physics*, 167(3):335–340, May 2012.
- [21] S. Doyle. Lumped element kinetic inductance detectors. 2008.
- [22] A. Endo, J. J. A. Baselmans, P. P. van der Werf, B. Knoors, S. M. H. Javadzadeh, S. J. C. Yates, D. J. Thoen, L. Ferrari, A. M. Baryshev, Y. J. Y. Lankwarden, P. J. de Visser, R. M. J. Janssen, and T. M. Klapwijk. Development of DESHIMA: a redshift machine based on a superconducting on-chip filterbank. In Wayne S. Holland, editor, *Millimeter, Submillimeter, and Far-Infrared Detectors and Instrumentation for Astronomy VI*, volume 8452, page 84520X. International Society for Optics and Photonics, SPIE, 2012.
- [23] Akira Endo, Kenichi Karatsu, Alejandro Pascual Laguna, Behnam Mirzaei, Robert Huiting, David Thoen, Vignesh Murugesan, Stephen J. C. Yates, Juan Bueno, Nuri V. Marrewijk, Sjoerd Bosma, Ozan Yurduseven, Nuria Llombart, Junya Suzuki, Masato Naruse, Pieter J. de Visser, Paul P. van der Werf, Teunis M. Klapwijk, and Jochem J. A. Baselmans. Wideband on-chip terahertz spectrometer based on a superconducting filterbank. *Journal of Astronomical Telescopes, Instruments, and Systems*, 5(3):035004, 2019.
- [24] Duncan Farrah, Kimberly Ennico Smith, David Ardila, Charles M. Bradford, Michael J. DiPirro, Carl Ferkinhoff, Jason Glenn, Paul F. Goldsmith, David T. Leisawitz, Thomas

- Nikola, Naseem Rangwala, Stephen A. Rinehart, Johannes G. Staguhn, Michael Zemcov, Jonas Zmuidzinas, James Bartlett, Sean J. Carey, William J. Fischer, Julia R. Kamenetzky, Jeyhan Kartaltepe, Mark D. Lacy, Dariusz C. Lis, Lisa S. Locke, Enrique Lopez-Rodriguez, Meredith MacGregor, Elisabeth Mills, Samuel H. Moseley, Eric J. Murphy, Alan Rhodes, Matthew J. Richter, Dimitra Rigopoulou, David B. Sanders, Ravi Sankrit, Giorgio Savini, John-David Smith, and Sabrina Stierwalt. Review: far-infrared instrumentation and technological development for the next decade. *Journal of Astronomical Telescopes, Instruments, and Systems*, 5(2):020901, 2019.
- [25] Jiansong Gao. The physics of superconducting microwave resonators. *Caltech THESIS*, May 2008.
- [26] K. Geerlings, Z. Leghtas, I. M. Pop, S. Shankar, L. Frunzio, R. J. Schoelkopf, M. Mirrahimi, and M. H. Devoret. Demonstrating a driven reset protocol for a superconducting qubit. *Phys. Rev. Lett.*, 110:120501, Mar 2013.
- [27] Paul A. George, Christina Manolatou, Farhan Rana, Adam L. Bingham, and Daniel R. Grischkowsky. Integrated waveguide-coupled terahertz microcavity resonators. *Applied Physics Letters*, 91(19):191122, 11 2007.
- [28] Sunil R. Golwala, Clint Bockstiegel, Spencer Brugger, Nicole G. Czakon, Peter K. Day, Thomas P. Downes, Ran Duan, Jiansong Gao, Amandeep K. Gill, Jason Glenn, Matthew I. Hollister, Henry G. LeDuc, Philip R. Maloney, Benjamin A. Mazin, Sean G. McHugh, David Miller, Omid Noroozian, Hien T. Nguyen, Jack Sayers, James A. Schlaerth, Seth Siegel, Anastasios K. Vayonakis, Philip R Wilson, and Jonas Zmuidzinas. Status of MUSIC, the Multiwavelength Sub/millimeter Inductance Camera. In Wayne S. Holland, editor, *Millimeter, Submillimeter, and Far-Infrared Detectors and Instrumentation for Astronomy VI*, volume 8452, page 845205. International Society for Optics and Photonics, SPIE, 2012.
- [29] C.J Gorter and H Casimir. On supraconductivity i. *Physica*, 1(1):306–320, 1934.
- [30] Griffin, M. J. and et al. The herschel-spire instrument and its in-flight performance*. *A&A*, 518:L3, 2010.
- [31] S. Hailey-Dunsheath, E. Shirokoff, P. S. Barry, C. M. Bradford, G. Chattopadhyay, P. Day, S. Doyle, M. Hollister, A. Kovacs, H. G. LeDuc, P. Mauskopf, C. M. McKenney, R. Monroe, R. O'Brient, S. Padin, T. Reck, L. Swenson, C. E. Tucker, and J. Zmuidzinas. Status of SuperSpec: a broadband, on-chip millimeter-wave spectrometer. In

Wayne S. Holland and Jonas Zmuidzinas, editors, *Millimeter, Submillimeter, and Far-Infrared Detectors and Instrumentation for Astronomy VII*, volume 9153 of *Society of Photo-Optical Instrumentation Engineers (SPIE) Conference Series*, page 91530M, August 2014.

- [32] Steven Hailey-Dunsheath, Reinier M. J. Janssen, Jason Glenn, Charles M. Bradford, Joanna Perido, Joseph Redford, and Jonas Zmuidzinas. Kinetic inductance detectors for the Origins Space Telescope. *Journal of Astronomical Telescopes, Instruments, and Systems*, 7(1):011015, 2021.
- [33] R. M. J. Janssen, J. J. A. Baselmans, A. Endo, L. Ferrari, S. J. C. Yates, A. M. Baryshev, and T. M. Klapwijk. High optical efficiency and photon noise limited sensitivity of microwave kinetic inductance detectors using phase readout. *Applied Physics Letters*, 103(20):203503, 11 2013.
- [34] Cecile Jung-Kubiak, Theodore J. Reck, Jose V. Siles, Robert Lin, Choonsup Lee, John Gill, Ken Cooper, Imran Mehdi, and Goutam Chattopadhyay. A multistep drie process for complex terahertz waveguide components. *IEEE Transactions on Terahertz Science and Technology*, 6(5):690–695, 2016.
- [35] S. B. Kaplan, C. C. Chi, D. N. Langenberg, J. J. Chang, S. Jafarey, and D. J. Scalapino. Quasiparticle and phonon lifetimes in superconductors. *Phys. Rev. B*, 14:4854–4873, Dec 1976.
- [36] K. S. Karkare, A. J. Anderson, P. S. Barry, B. A. Benson, J. E. Carlstrom, T. Cecil, C. L. Chang, M. A. Dobbs, M. Hollister, G. K. Keating, D. P. Marrone, J. McMahon, J. Montgomery, Z. Pan, G. Robson, M. Rouble, E. Shirokoff, and G. Smecher. Spt-slim: A line intensity mapping pathfinder for the south pole telescope. *Journal of Low Temperature Physics*, 209(5):758–765, Dec 2022.
- [37] K. S. Karkare, P. S. Barry, C. M. Bradford, S. Chapman, S. Doyle, J. Glenn, S. Gordon, S. Hailey-Dunsheath, R. M. J. Janssen, A. Kovács, H. G. LeDuc, P. Mauskopf, R. McGeehan, J. Redford, E. Shirokoff, C. Tucker, J. Wheeler, and J. Zmuidzinas. Full-Array Noise Performance of Deployment-Grade SuperSpec mm-Wave On-Chip Spectrometers. *Journal of Low Temperature Physics*, 199(3-4):849–857, February 2020.
- [38] Garrett K. Keating, Geoffrey C. Bower, Daniel P. Marrone, David R. DeBoer, Carl Heiles, Tzu-Ching Chang, John E. Carlstrom, Christopher H. Greer, David Hawkins, James W. Lamb, Erik Leitch, Amber D. Miller, Stephen Mchovaj, and David P. Woody.

- First results from copss: The co power spectrum survey. *The Astrophysical Journal*, 814(2):140, November 2015.
- [39] Ely D. Kovetz, Marco P. Viero, Adam Lidz, Laura Newburgh, Mubdi Rahman, Eric Switzer, Marc Kamionkowski, James Aguirre, Marcelo Alvarez, James Bock, J. Richard Bond, Goeffry Bower, C. Matt Bradford, Patrick C. Breysse, Philip Bull, Tzu-Ching Chang, Yun-Ting Cheng, Dongwoo Chung, Kieran Cleary, Asantha Corray, Abigail Crites, Rupert Croft, Olivier Doré, Michael Eastwood, Andrea Ferrara, José Fonseca, Daniel Jacobs, Garrett K. Keating, Guilaine Lagache, Gunjan Lakhani, Adrian Liu, Kavilan Moodley, Norm Murray, Aurélie Pénin, Gergö Popping, Anthony Pullen, Dominik Reichers, Shun Saito, Ben Saliwanchik, Mario Santos, Rachel Somerville, Gordon Stacey, George Stein, Francesco Villaescusa-Navarro, Eli Visbal, Amanda Weltman, Laura Wolz, and Micheal Zemcov. Line-intensity mapping: 2017 status report. 2017.
- [40] Antony Lewis and Sarah Bridle. Cosmological parameters from CMB and other data: A Monte Carlo approach. *Phys. Rev. D*, 66:103511, 2002.
- [41] H. F. Liu, X. X. Song, Q. Wang, W. J. Wu, J. Fan, J. Q. Liu, and L. C. Tu. Healing pinhole shorts for applications using intermetal dielectric films. In *2017 IEEE 12th Nanotechnology Materials and Devices Conference (NMDC)*, pages 68–69, 2017.
- [42] D. C. Mattis and J. Bardeen. Theory of the anomalous skin effect in normal and superconducting metals. *Phys. Rev.*, 111:412–417, Jul 1958.
- [43] P. D. Mauskopf, S. Doyle, P. Barry, S. Rowe, A. Bidead, P. A. R. Ade, C. Tucker, E. Castillo, A. Monfardini, J. Goupy, and M. Calvo. Photon-noise limited performance in aluminum lekids. *Journal of Low Temperature Physics*, 176(3):545–552, Aug 2014.
- [44] Benjamin A. Mazin. Microwave kinetic inductance detectors. *CaltechTHESIS*, Aug 2004.
- [45] Benjamin A. Mazin, Peter K. Day, Henry G. LeDuc, Anastasios Vayonakis, and Jonas Zmuidzinas. Superconducting kinetic inductance photon detectors. In Howard A. MacEwen, editor, *Highly Innovative Space Telescope Concepts*, volume 4849, pages 283 – 293. International Society for Optics and Photonics, SPIE, 2002.
- [46] Ryan A. McGeehan. Superspec: Development and characterization of kinetic inductance detector-based on-chip spectrometer for millimeter and sub-millimeter observations. *ProQuest Dissertations and Theses*, page 122, 2023 2023. Copyright - Database

copyright ProQuest LLC; ProQuest does not claim copyright in the individual underlying works; Last updated - 2024-02-23.

- [47] J. McMahon, J. W. Appel, J. E. Austermann, J. A. Beall, D. Becker, B. A. Benson, L. E. Bleem, J. Britton, C. L. Chang, J. E. Carlstrom, H. M. Cho, A. T. Crites, T. Essinger-Hileman, W. Everett, N. W. Halverson, J. W. Henning, G. C. Hilton, K. D. Irwin, J. Mehl, S. S. Meyer, S. Mossley, M. D. Niemack, L. P. Parker, S. M. Simon, S. T. Staggs, C. Visnjic, E. Wollack, K. U.-Yen, K. W. Yoon, and Y. Zhao. Planar Orthomode Transducers for Feedhorn-coupled TES Polarimeters. *AIP Conference Proceedings*, 1185(1):490–493, 12 2009.
- [48] A. Monfardini, A. Benoit, A. Bideaud, L. Swenson, A. Cruciani, P. Camus, C. Hoffmann, F. X. Désert, S. Doyle, P. Ade, P. Mauskopf, C. Tucker, M. Roesch, S. Leclercq, K. F. Schuster, A. Endo, A. Baryshev, J. J. A. Baselmans, L. Ferrari, S. J. C Yates, O. Bourrion, J. Macias-Perez, C. Vescovi, M. Calvo, and C. Giordano. A dual-band millimeter-wave kinetic inductance camera for the iram 30 m telescope. *The Astrophysical Journal Supplement Series*, 194(2):24, may 2011.
- [49] R. Nie, J. P. Filippini, E. Brooks, P. Barry, J. Connors, C. Fazar, M. Gradziel, D. Mercado, D. Patru, E. Shirokoff, L. Spencer, S. Tramm, N. Trappe, and Zemcov M. A vacuum waveguide filter bank spectrometer for far-infrared spectroscopy. *J. Low Temp. Phys.*, This Special Issue, 2023.
- [50] Rong Nie, Jeffrey Filippini, Elyssa Brooks, Peter Barry, Jake Connors, Marcin Gradziel, Dale Mercado, Vesal Razavimaleki, Erik Shirokoff, Locke Spencer, Serena Tramm, Neil Trappe, and Michael Zemcov. A vacuum waveguide filter bank spectrometer for far-infrared astrophysics. *Journal of Low Temperature Physics*, Jun 2024.
- [51] Poglitsch, A. and et al. The photodetector array camera and spectrometer (pacs) on the herschel space observatory*. *A&A*, 518:L2, 2010.
- [52] D. Pozar. *Microwave Engineering*. Wiley, 2011.
- [53] Anthony R. Pullen, Tzu-Ching Chang, Olivier Doré, and Adam Lidz. Cross-correlations as a cosmological carbon monoxide detector. *The Astrophysical Journal*, 768(1):15, April 2013.
- [54] G. Robson, A. J. Anderson, P. S. Barry, S. Doyle, and K. S. Karkare. The simulation and design of an on-chip superconducting millimetre filter-bank spectrometer. *Journal of Low Temperature Physics*, 209(3):493–501, Nov 2022.

- [55] P. Schechter. An analytic expression for the luminosity function for galaxies. *ApJ*, 203:297–306, January 1976.
- [56] A. V. SERGEEV and M. YU. REIZER. Photoresponse mechanisms of thin superconducting films and superconducting detectors. *International Journal of Modern Physics B*, 10(06):635–667, 1996.
- [57] E. Shirokoff, P. S. Barry, C. M. Bradford, G. Chattopadhyay, P. Day, S. Doyle, S. Hailey-Dunsheath, M. I. Hollister, A. Kovács, H. G. Leduc, C. M. McKenney, P. Mauskopf, H. T. Nguyen, R. O'Brient, S. Padin, T. J. Reck, L. J. Swenson, C. E. Tucker, and J. Zmuidzinas. Design and performance of superspec: An on-chip, kid-based, mm-wavelength spectrometer. *Journal of Low Temperature Physics*, 176(5):657–662, Sep 2014.
- [58] L. J. Swenson, P. K. Day, B. H. Eom, H. G. Leduc, N. Llombart, C. M. McKenney, O. Noroozian, and J. Zmuidzinas. Operation of a titanium nitride superconducting microresonator detector in the nonlinear regime. *Journal of Applied Physics*, 113(10):104501, 03 2013.
- [59] Q. Y. Tang, P. S. Barry, R. Basu Thakur, A. Kofman, A. Nadolski, J. Vieira, and E. Shirokoff. Fabrication of antenna-coupled kid array for cosmic microwave background detection. *Journal of Low Temperature Physics*, 193(3):149–156, Nov 2018.
- [60] Qing Y. Tang. Development of kinetic inductance detectors for mm and sub-mm observations. *ProQuest Dissertations and Theses*, page 113, 2021 2021.
- [61] Akio Taniguchi, Tom J. L. C. Bakx, Jochem J. A. Baselmans, Robert Huiting, Kenichi Karatsu, Nuria Llombart, Matus Rybak, Tatsuya Takekoshi, Yoichi Tamura, Hiroki Akamatsu, Stefanie Brackenhoff, Juan Bueno, Bruno T. Buitendorp, Shahab O. Dabironezare, Anne-Kee Doing, Yasunori Fujii, Kazuyuki Fujita, Matthijs Gouwerok, Sebastian Hähnle, Tsuyoshi Ishida, Shun Ishii, Ryohei Kawabe, Tetsu Kitayama, Kotaro Kohno, Akira Kouchi, Jun Maekawa, Keiichi Matsuda, Vignesh Murugesan, Shunichi Nakatsubo, Tai Oshima, Alejandro Pascual Laguna, David J. Thoen, Paul P. van der Werf, Stephen J. C. Yates, and Akira Endo. Deshima 2.0: Development of an integrated superconducting spectrometer for science-grade astronomical observations. *Journal of Low Temperature Physics*, 209(3):278–286, Nov 2022.
- [62] M. Tapia, P. A. R. Ade, E. Aguilar Pérez, P. S. Barry, T. L. R. Brien, E. Castillo-Domínguez, C. Dodd, C. Dunscombe, S. Eales, D. Ferrusca Sr., V. Gómez-Rivera,

- P. Hargrave, J. L. Hernández-Rebollar, A. Hornsby, J. House, D. Hughes, J. M. Jáuregui García, P. Mauskopf, D. Murias, A. Papageorgiou, E. Pascale, N. Peretto, A. Pérez, S. Rowe, D. Sánchez-Argüelles, M. W. L. Smith, K. Souccar, R. Sudiwala, A. Torres Campos, C. Tucker, M. Velázquez, S. Ventura-González, I. Walker, and S. Doyle. The Mexico UK Sub-mm Camera for Astronomy (MUSCAT) on-sky commissioning: focal plane performance. In Jonas Zmuidzinas and Jian-Rong Gao, editors, *Millimeter, Sub-millimeter, and Far-Infrared Detectors and Instrumentation for Astronomy XI*, volume 12190, page 1219017. International Society for Optics and Photonics, SPIE, 2022.
- [63] Jason Tumlinson, Molly S. Peeples, and Jessica K. Werk. The Circumgalactic Medium. *ARA&A*, 55(1):389–432, August 2017.
- [64] C. M. Wilson and D. E. Prober. Quasiparticle number fluctuations in superconductors. *Phys. Rev. B*, 69:094524, Mar 2004.
- [65] Yuxuan Yuan, Mark R. Krumholz, and Crystal L. Martin. The observable properties of cool winds from galaxies, AGN, and star clusters - II. 3D models for the multiphase wind of M82. *MNRAS*, 518(3):4084–4105, January 2023.
- [66] Jonas Zmuidzinas. Superconducting microresonators: Physics and applications. *Annual Review of Condensed Matter Physics*, 3(1):169–214, 2012.